Nanotribology and Nanomechanics of Ultra Thin Films for Hard Disk Drives

By

Yu Lo

B. S. (National Taiwan University) 1993

M. S. (University of California, Berkeley) 1997

A dissertation submitted in partial satisfaction of the

Requirements for the degree of

Doctor of Philosophy

In

Engineering-Mechanical Engineering

In the

GRADUATE DIVISION

Of the

UNIVERSITY of CALIFORNIA, BERKELEY

Committee in charge:

Professor David B. Bogy, Chair
Professor Panayiotis Papadopoulos
Professor Robert O. Ritchie

Fall 1999

UMI Number: 9966459

UMI®

UMI Microform 9966459

Bell & Howell Information and Learning Company
300 North Zeeb Road
P.O. Box 1346
Ann Arbor, MI 48106-1346

Nanotribology and Nanomechanics of Ultra Thin Solid Films for Hard Disk Drives

by

Yu Lo

To My Late Father, My Mother, and My Wife, Yining

TABLE OF CONTENTS

LIST OF FIGURES

Chapter 2

Chapter 3

Chapter 4

Chapter 5

Chapter 6

Chapter 7

LIST OF TABLES

Chapter 6

Chapter 7

ACKNOWLEGMENTS

First and foremost, I would like to express my sincere gratitude to my advisor, Professor David B. Bogy, for his continuous guidance and support throughout my Ph.D. research. I consider this experience honorable and invaluable, one that not only escalated my professional skills, but also assimilated me into the American culture. I would also like to thank Professors Panayiotis Papadopoulos and Robert O. Ritchie for reviewing this manuscript.

I am grateful to Mr. Tomas Wyrobek, Mr. Lance Khun, Dr. Douglas A. Crowson, Dr. Antanas Daugela, and everybody else from Hysitron Incorporated for generously providing one of their very first transducers to the Computer Mechanics Laboratory and their continuous hardware and software supports. It has proved that the collaboration between Hysitron and CML is constructive and mutual-beneficial. Thanks also go to Dr. Othon R. Monteiro of the Lawrence Berkeley National Laboratory for his helpful suggestions and advice. In addition, the Cathodic-arc amorphous carbon films were fabricated in the chamber at LBNL with his permission and help.

I would also like to thank my colleagues in CML for their friendship and support. In particular, I am thankful to Walton Fong for his help in fabricating the CAC films and useful discussions. I also appreciate the valuable discussions with Dr. Weidong Huang. Thanks also go to Ryan Grisso for his friendship and his help in the computer systems. I had a very good time in CML.

Any acknowledgments would not be complete without mentioning my family. My late father completely devoted himself to the family. It was his hope to see his children well

educated. I regret that I was not able to present this achievement to him soon enough. My mother is a high school mathematics teacher who gave me my first instruction in math. My deepest appreciation belongs to my wife, Yining, for her love, patience, and comfort.

Chapter 1

GENERAL INTRODUCTION

1.1 THIN FILM OVERCOATS IN MAGNETIC HARD DISK DRIVES

Since first being introduced to the public in the 1959, innovations and breakthroughs resulting from transistor-based computers have continuously and rapidly changed our world. With the rapid recent rise of the Internet, the needs for more and faster computers have pushed the computer industry toward even faster growth. Soon, one will be able to store every single piece of information (including text, audio, and video), digitally in personal computers. To achieve this ultimate goal, a large, fast, low-cost, and easily available data storage system is needed. IBM foresaw this strong demand and introduced the first commercial hard disk drive, the IBM 305, or RAMAC, in 1956. It had fifty 24-in.-diameter disks with an areal density of about 0.3 Kb/in^2. The total storage capacity of the 305 RAMAC was 5 Mbytes - not even enough to hold this dissertation on one single drive. Improvements made in the past 40 years have increased the areal density to 10 Gb/in^2 commercially, and as much as 37 Gb/in^2 in the laboratory. One of the many reasons for the incredible jump is the dramatic reduction of magnetic spacing in the modem drives. The magnetic spacing is the actual distance between the read-write head and the magnetic layer on the disk, and consists of two physical components: the air bearing flying height and the overcoat thicknesses. The flying height used in the commercial hard disk drives today is about 15-25 nm. Researchers are experimenting with slider designs towards pseudo contact to minimize the flying height and thus to further increase the areal density.

Protective thin film overcoats have been applied on the sliders and disks to improve their tribological performance and to prevent data loss. Since the addition of these films increases the magnetic spacing by the thickness of the films, the films are required to be very thin, yet robust against corrosion and physical contact with the sliders. In today's disk drives, the films are usually made of sputtered hydrogenated carbon (CH_x) or nitrogenated carbon (CN_x) with thcknesses of 7 to 10 nm. To achieve the future areal density goals, the film thickness has to drop to 2 nm. But questions arise as to how to characterize the properties of these ultra thin films. The major properties of interest are: atomic and chemical structures; the electrical properties; film thickness and surface topography; and mechanical properties, such as the elastic modulus, yielding strength, internal stresses, and the interaction with the substrates. For atomic and chemical structure characterizations, equipment such as the Scanning Electron Microscopy (SEM), the Transmission Electron Microscopy (TEM), the Auger Electron Spectroscopy (AES), the X-Ray Photoelectron Spectroscopy (XPS), and the Rutherford Backscattering (RBS), have been developed. The Scanning Tunneling Microscopy (STM) and the Atomic Force Microscope (AFM) are able to obtain the film surface topography at atomic resolution. However, the mechanical properties of the thin films could not be conveniently measured until the emergence of the Point Contact Microscope (1992) and the commercially available Hysitron Picoindenter (1996), using the technique of nanoindentation.

The PCM and the Hysitron Picoindenter are capable of obtaining the mechanical hardness (and with the Hysitron, elastic modulus) of ultra thin films. Although macroindentation tests have been used to measure material hardness for about a hundred years, nanoindentation tests on ultra thin films have remained a challenge for researchers due to the extremely high system sensitivity, stability, and resolution requirements. Difficulties arise due to the need for such tiny indentations. For example, the residual indentation areas cannot be seen by the naked eye, and their boundaries are influenced by the surface roughness due to comparable indentation sizes. Additionally, the indenter tip must be sharp enough to generate stresses that are considerably higher than the material yield strengths. Although commercial products have recently become available, understanding of nanoindentation techniques is still in the stage of exploration and development. Therefore, this dissertation mostly focuses on further developments in nanoindentation techniques, and on studies of phenomena generated by nanoindentations.

1.2 OVERVIEW

The dissertation is divided into eight chapters. Chapter 1-7 present the analysis of the load-unload versus displacement curves obtained experimently. Chapter 8 presents the study of the newly developed cathodic-arc amorphous carbon films.

After this introductory chapter, the experimental apparatus is reviewed and discussed in Chapter 2. Two pieces of equipment were used to study the ultra thin film overcoats in this dissertation: the Point Contact Microscope (PCM) and the Hysitron Picoindenter. Both machines are able to measure the hardness of thin films. Due to their different characteristics, the definitions of hardnesses obtained using the PCM and the Hysitron Picoindenter are different. The PCM measures the residual indentation areas with post-indentation scans and obtains the hardnesses defined as the maximum loads divided by the residual indentation areas. The Hysitron Picoindenter, however, measures the hardnesses defined as the maximum loads divided by the maximum contact areas with the proper application of elastic theories. The advantages and disadvantages of both systems are discussed. It is concluded that the Hysitron Picoindenter surpasses the PCM, and therefore it was chosen to conduct most of the experiments.

Elastic theories are introduced and discussed in Chapter 3 in order to analyze the load-unload/displacement curves obtained with the Hysitron Picoindenter. Sneddon's solution for the elastic stress field of a half space indented by a flat, cylindrical, and rigid punch is the backbone of the theories. Since the geometry of the indentation tests is different from that of Sneddon's problem, boundary conditions of both geometries are closely examined. It is then concluded that Sneddon's solution is valid for the indentation experiments. An indenter calibration procedure is provided to close the indeterminate system of equations obtained from Sneddon's solution. Because we are interested in thin films that are deposited on substrates, the substrate effects for the indentation measurements are also discussed. A rule of thumb is proposed based on the percentage of the film thickness for the substrate effects of elastic modulus measurements.

The techniques discussed in Chapter 3 implicitly assume rigid indenters. The assumption is valid for most materials if the indenter is made from diamond, which has a hardness of about 100 GPa. However, the recently developed cathodic-arc amorphous carbon films can be as hard as 70 GPa. Even diamond indenters will deform while indenting these films. In this case, Sneddon's solution will overestimate the hardness and elastic modulus of the specimen. In Chapter 4, a compensation procedure is proposed for elastic indenter deformation while indenting very hard materials. Sneddon's load/displacement relation is re-derived using the Hertz contact theory. Another equation is also obtained and the system of equations is automatically determinate; no tip shape function is needed. The tip radius of the indenter can also be calculated from the procedure without complicated and costly process. The limitations of using this procedure are also discussed, and it is shown that they can be avoided. Finally, the calculated hardness and elastic modulus values are compared with the finite element simulation results by Follstaedt et al. (1997).

As discussed in Chapter 3, only the initial portion of the unloading process of an indentation is purely elastic. Yielding in tension usually occurs right before the load is completely removed. Chapter 5 discusses the phenomenon of indentation hysteresis and presents studies of the substrate effects of hardness measurements using different types of hysteresis mechanisms. One type of indentation hysteresis can be generated with repeated indentations at the same location on the material surface due to the non-elastic unloading process. This type of hysteresis is usually seen on metals and is subject to shakedown after a few cycles of repeated loadings. The second type of indentation hysteresis is found on silicon (or germanium) due to a reversible pressure-induced phase transformation. This type of hysteresis is not subject to shakedown and is always present as an energy consumption mechanism. Substrate effects are then studied on the specimen with film hysteresis that is subject to shakedown and another substrate hysteresis that is not subject to shakedown.

The theoretical developments presented in both Chapter 3 and Chapter 4 consider the specimen surface as mathematically flat. However, real surfaces always have roughness and waviness. Moreover, in some cases, our interest is on the asperities, such as laser bumps on the specimen surfaces. The local curvature at the contact points plays an important role in the estimation of the mechanical properties. Chapter 6 studies the geometry effect and proposes a correction method for non-flat indentations based on the Hertz contact theory. This correction method is compared with that proposed by Bobji et al. (1996)

Anders et al. (1994) adopted cathodic-arc deposition techniques for the disk drive applications. At a deposition substrate bias of −100 V, the cathodic-arc amorphous carbon (CAC) films have an sp^3 content of 85%, and hardness of 60 GPa, elastic modulus of 400 GPa, and a density of 3 g/cm^3 (Anders et al. 1994 and Veerasamy et al. 1993). With such superior characteristics, the CAC films may be the solution enabling the 2 nm protective films to reach the future areal density goal of 100 Gb/in^2. In Chapter 7 we adopt all of these techniques (as well as correction methods mentioned in the previous chapters) and we present practical studies of the mechanical properties of CAC films of different thicknesses. Films deposited on silicon wafers and on Permalloy sublayers are tested. The indentation results show that the hardnesses and elastic modulii of the CAC films are dependent on the film thickness. An explanation based on the sp^3 concentration is provided.

Chapter 2

EXPERIMENTAL SETUP

2.1 INTRODUCTION

The primary challenge in determining the mechanical properties of thin films 5-20 nm thick is to modify the material surfaces with sufficiently small but nontrivial indentations or scratches. In some cases, it is also necessary to obtain post-indentation images of cavities made by indentations. The Atomic Force Microscope is able to scan sample surfaces with forces in the pico-Newton range and to obtain images with atomic resolution. However, the traditional AFM's suspension and tip are not strong enough to modify most solid sample surfaces. Some modification or an alternative is needed to achieve this goal.

The Point Contact Microscope (PCM), which was originally developed by Kaneko and his coworkers (1988) and further modified by Lu et al. (1994), was the first one we employed to study thin film hardness. The PCM is able to indent and scratch the sample surfaces with normal forces in the micro-Newton range. The residual areas are obtained with post-indentation scans. The surface hardnesses of the samples are then calculated as the maximum loads divided by the residual areas. However, the PCM is not able to record the load/displacement curve during an indentation. Material responses during the indentation process cannot be obtained.

Therefore, the Hysitron system, which provides real-time load/displacement curves, was adopted to improve the experiments and to acquire more useful information. This chapter briefly describes the PCM and the Hysitron systems. The advantages and disadvantages of both systems are also discussed.

2.2 POINT CONTACT MICROSCOPE

2.2.1 Equipment setup

The Atomic Force Microscope (AFM), which was developed initially by Binnig, Quate, and Gerber (Binnig et al., 1986), is a scanning probe device that is able to scan various sharp probes over sample surfaces and obtain the topography of the surfaces. The probes, or tips, are usually made from silicon nitride with tip radii of about 4 nm for the latest systems. The topography is obtained from the necessary height change of the sample holder to keep the deflection of the cantilever, and hence the contact force, constant. As suggested by its name, the AFM is able to obtain images of surfaces at atomic resolutions with these sharp tips. However, since the tip materials are not very hard and the tip radii are very small, the AFM is not able to modify most sample surfaces, nor therefore, to measure the mechanical properties of the surfaces.

To overcome this problem and to expand the ability of the AFM, Kaneko and his colleagues (Kaneko et al., 1988) developed the Point Contact Microscope (PCM). Figure 2.1 shows a schematic diagram of the PCM. The PCM is connected through an interface circuit to a Digital Instruments (DI) Nanoscope II SPM controller with the DI software. The scanning probe, or the tip, is made of diamond and is mounted on a stainless steel cantilever assembly. The diamond tips used by the PCM are three-sided pyramids with tip radii of about 100 nm to 200 nm and apex angles of 60° or 80°. The deflection of the cantilever is measured by a focusing-error-detection optical head, whose resolution is better than 1 nm. The laminated PZT actuator is controlled by one dc power supply with a range of 0-100 volts. It has a sensitivity of about 0.15 μm/V, giving a total z-range of 15 μm. By decreasing the voltage in the laminated PZT, hence pulling the PZT end of the cantilever, a force can be exerted against the sample surface by the diamond indenter. The area in the vicinity of the indentation is scanned with a small force (1 μN) immediately after the indentation process. The size of the indentation area is then assessed from the scanned image. The hardness of the material surface is calculated by dividing the maximum indentation load by the residual indentation area.

Therefore, the PCM is able to measure the surface hardness of materials with post-indentation scans. However, the PCM is not able to record the material responses during the indentation processes. Additional material properties, such as the elastic modulus, could not be obtained by PCM measurements. Moreover, assessment of the residual areas with post-indentation scans generates measurement errors that are inherent in the PCM, especially for small indentations. This problem is discussed in the next section.

2.2.2 Measurement errors inherent in the PCM

Lu et al. (1994) reported increasing hardness values for polycarbonate and gold with decreasing indentation force and depth. Figure 2.2 shows the geometry of a diamond tip used in their indentation hardness measurements by the SPM, where r is the smallest radius of the tip and $2t$ is the lateral dimension of its rounded point. Figure 2.3 shows a scan of an indentation made by such a tip on a typical surface. Dimensions a and b are the lateral dimensions of the indentation and of the scanned indentation, respectively. The tip does not follow the surface exactly because of the rounded point. If the cavity is much larger than the indenter lateral dimension, i.e. $a >> t$, the scanned indentation area, b^2 is approximately equal to the true indentation area a^2. That means the error introduced by the tip itself is negligible. However, if the cavity size is comparable to the indenter lateral dimension, i.e. $a \sim t$, the scanned diameter b is much smaller than the true diameter a. The error in the area values introduced by scanning with such a tip is plotted as a function of a in Figure 2.4, where the indentation mark is assumed to be circular. Note that the errors introduced in the indentation areas are also the ones affecting the measured hardness values. As t/a approaches 1/2, the error goes to infinity because b^2 approaches zero, and therefore the obtained hardness values tend to infinity. When a is larger than about $10t$, that is $t/a < 0.1$, the error is almost negligible. This phenomenon accounts for the increased hardness measurements at small indentation depths as observed by Lu et al. (1994).

Since it is very hard to obtain the true indentation areas for tiny indentations by using the PCM, methods to obtain the relative hardness values by comparing the residual indentation depths or their reciprocals have been proposed (Yun, X. et al. 1996, and Hsiao, R. and Bogy, D. B. 1996). Since the residual depths are also obtained with post-indentation scans, there are difficulties associated with these methods too. One of the errors can be identified as resulting from the scan speeds used to acquire the post-indentation images. Figure 2.5 shows the measured depths of an indentation cavity with various post-indentation scan speeds together with the depth obtained with the Hysitron Picoindenter, whose working mechanism will be discussed in the ext section. For scans with larger speeds, the depths obtained are smaller for the same cavity. For scans at sufficiently low speed, the reported depth approaches the Hysitron measurement. Specifically, it takes about 1.5 minutes to complete a 1 μm by 1 μm area with the speed of 2 μm/s. However, it takes about 1 hour to obtain the image for the same area with the speed of 0.1 μm/s. The error in measuring the depth is as high as 60% and is attributed to the tip's inability to reach the deepest part of an indentation cavity while moving at high speeds across it. The lower the speed, the more completely the tip sinks into the cavity. Therefore, obtaining the relative hardness in this way may not be reliable or practical, since the true depths are not measured at reasonable scan speeds and may never be obtained by the scanning techniques. Since the thin film overcoats currently used in the industry are approximately 10 nm or thinner, an alternative technique should be adopted to characterize their mechanical properties.

2.3 HYSITRON TESTER

In order to avoid the difficulties encountered by the PCM, the Hysitron systems were employed for most of the work in this dissertation. There are two types of Hysitron systems. One is the single-axis tester, the Picoindenter; the other one is the two-axis tester, the Triboscope. Their working mechanisms are described in this section.

Figure 2.6 shows a schematic diagram of the Hysitron Picoindenter. The system is a portable add-on to commercially available AFM's. We use it with a Digital Instruments Nanoscope III. It essentially substitutes for the AFM scan head. Like its counterpart, the Hysitron Picindenter is able to scan sample surfaces with very low forces. However, unlike its counterpart, the Hysitron Picoindenter is also able to indent the sample surfaces. A detailed schematic diagram of its working mechanism is shown in Figure 2.7. The heart of the testing instrument is a three-plate capacitative force/displacement transducer, as illustrated also in Figure 2.8. It provides high sensitivity, large dynamic range, and a linear force or displacement output signal. It generates downward forces by changing the capacitance between the plates. The low sprung mass (200 mg) of the transducer's center plate minimizes the instrument's sensitivity to external vibrations, and allows very low force indentations to be made. The maximum and minimum loads that can be applied are 10 mN and 1μN, respectively, with a force sensitivity of 100 nN. The maximum displacement of the central plate is 5μm with a displacement sensitivity of 0.2 nm. The drift rate of the transducer after warm-up is 20 nN/min and 0.2 nm/min. All the tests were done after the transducer was warmed up.

The sensor consists of two fixed outer electrodes (drive plates), which are driven by AC signals out of phase with each other. The electric field potential between the plates can be considered to vary linearly, since the drive plates are parallel to each other and closely spaced. Since the signals applied to the drive plates are equal in magnitude but opposite in polarity at any instant, the electric field potential is maximized at the drive plates and minimized at the center plate. Terminals CHA HV IN and CHB HV IN in Figure 2.9 are used to provide the electrostatic force generated by the transducer. This allows for simultaneous determination of displacement and load during indentation tests. Therefore, a load/displacement curve, as shown in Figure 2.10, can be generated simultaneously for each indentation test. Using this result, the information for the material's deformation response to the indentation can be analyzed with the method mentioned in Chapter 3 or Chapter 4. Material properties such as hardness and elastic modulus can then be determined. Figure 2.11 depicts the block diagram for the Hysitron system in use with a scanning probe microscope, such as an AFM. The three blocks on the left side of the diagram (SPM controller, SPM computer and monitor) and the 3-D piezo-actuator are part of the microscope system. The transducer, the transducer controller, the transducer computer and monitor as well as the signal adapter comprise the Hysitron add-on system.

The Triboscope software versions 3 through 3.5 were used in the measurements reported in this dissertation. Various loading functions can be generated through the Triboscope software. Figure 2.12(a) and (b) show a triangular loading function and a trapezoidal loading function, respectively. The additional horizontal section between the load and unload curves for the trapezoidal function is usually used for materials that creep significantly. Cube corner diamond tips with nominal radii of 50 nm to 200 nm were most commonly used to make indentations. Figures 2.13 (a) and (b) show the geometry of a typical Hysitron indenter and a detailed view of a cube corner diamond tip, respectively. Since the tip radii are generally much larger than those of AFM tips (usually about a few nanometers), the system cannot provide imaging resolutions as high as regular AFMs. The transducers can provide a force output as low as 1 μN. Scanning with such a small force, we can easily obtain images without deforming the sample surfaces.

2.4 SUMMARY AND CONCLUSION

The working mechanisms of the PCM and the Hysitron Picoindenter are described and discussed. The hardness obtained with the PCM is defined as the maximum load divided by the residual indentation area. The PCM obtains the residual areas with post-indentation scans in the neighborhood of the indentation marks. However, inherent errors are associated with the PCM measurements and are closely examined. The Hysitron Picoindenter records the load-unload/displacement curves during the indentation processes. By analyzing the load/unload curves, hardness and reduced elastic modulus of the specimen can be obtained. Therefore, the Hysitron system is chosen as the instrument to perform all the measurements in this dissertation.

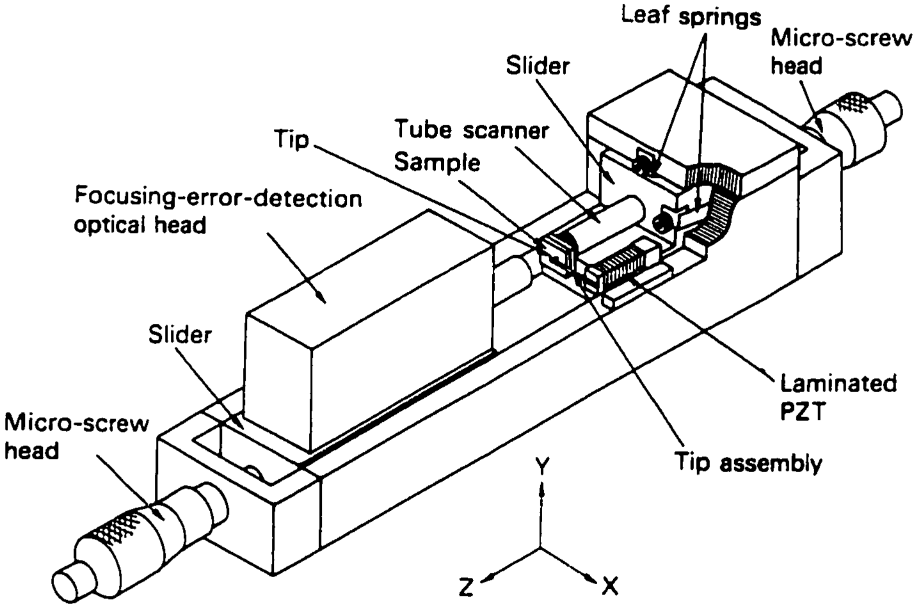

Fig. 2.1: A schematic diagram of the Point Contact Microscope (Kaneko et. al, 1998)

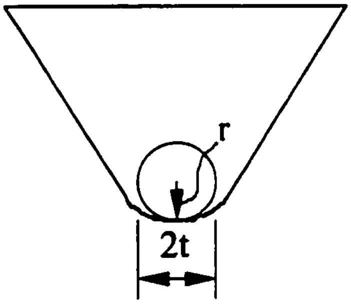

Fig. 2.2: The geometry of a diamond indenter used in the PCM. *r* is the tip radius and *t* is the tip lateral dimension.

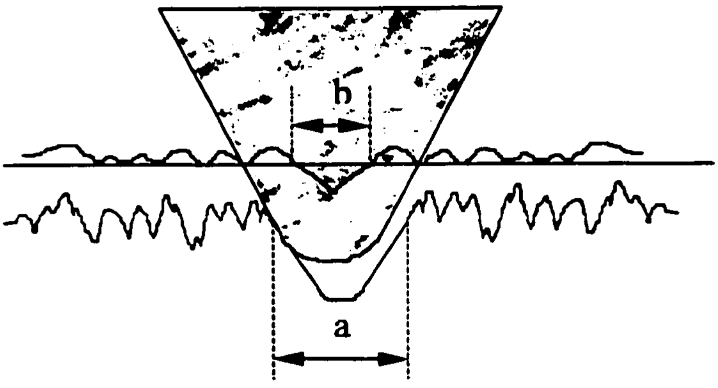

Fig. 2.3: The schematic trajectory of a indenter scanning on a rough surface. *a* is the actual diameter of the cavity and *b* is the scanned diameter of the cavity.

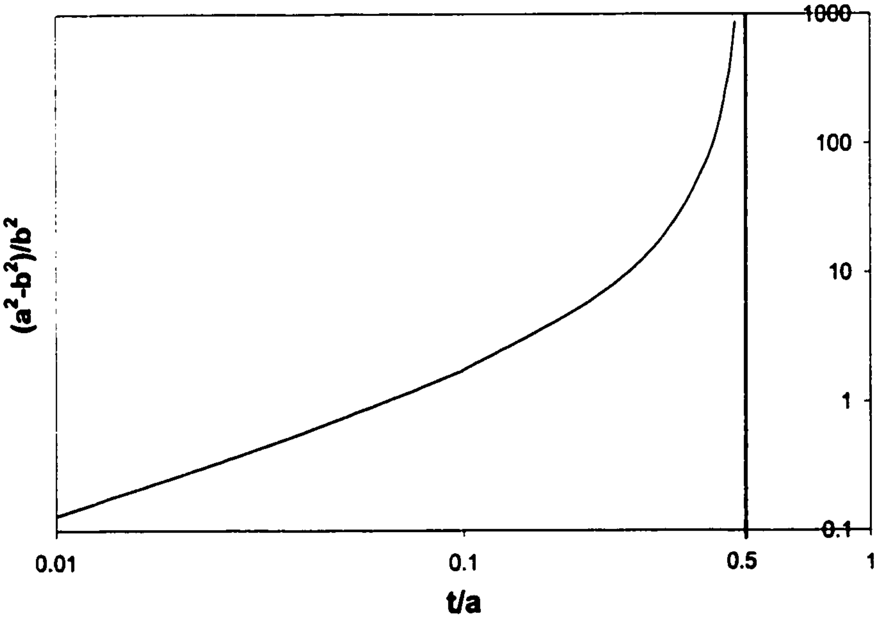

Fig. 2.4: Relative errors in the scanned areas as a function of the ratio of the indenter lateral dimension over the cavity diameter. When the ratio is small, the error is negligible. However, when t/a = 0.5, the error approaches to infinity.

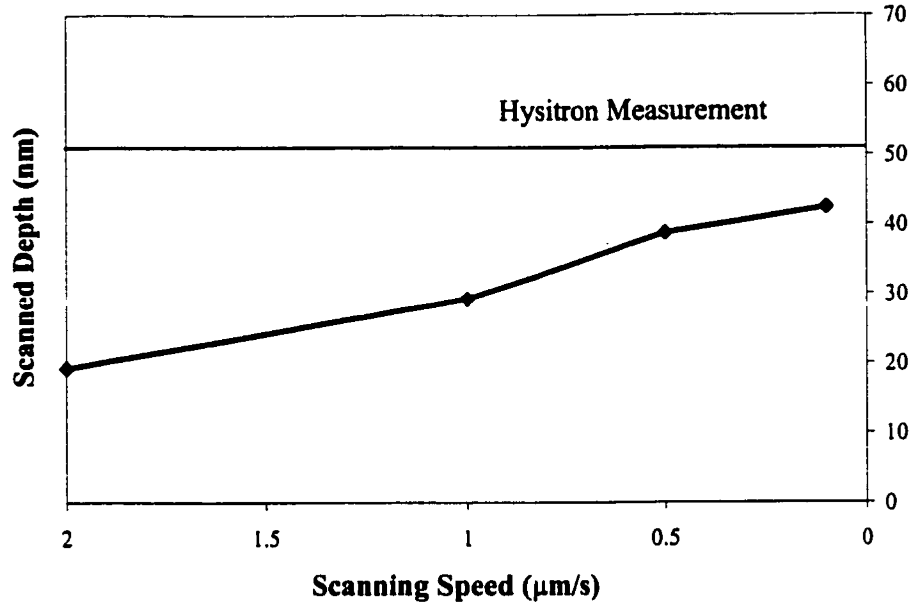

Fig. 2.5: Scanned depths of the same indentation cavity with various scan speeds. The Hysitron measurement is also shown.

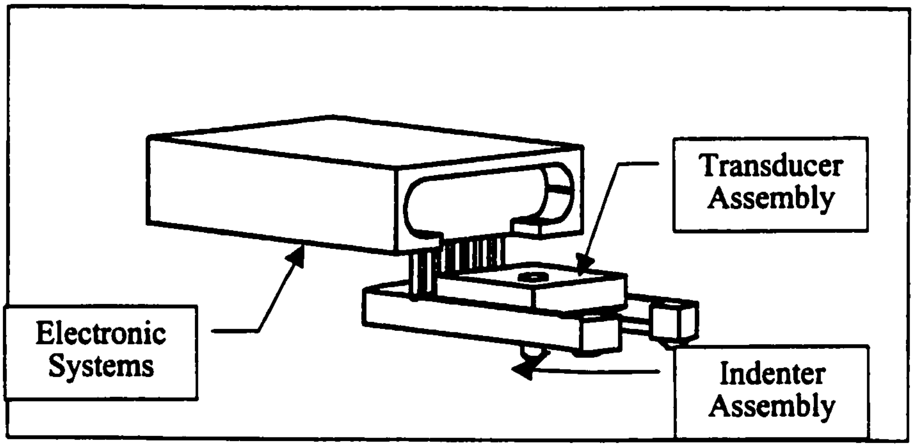

Fig. 2.6: A schematic diagram of a Hysitron Picoindenter. The transducer assembly is a three-capacitance design. The indenter assembly consists of a tip holder and a diamond tip at the very end.

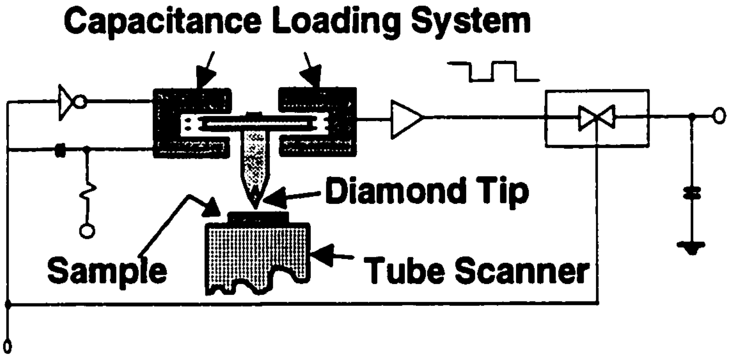

Fig. 2.7: Detailed view of the components of the Hysitron Picoindenter.

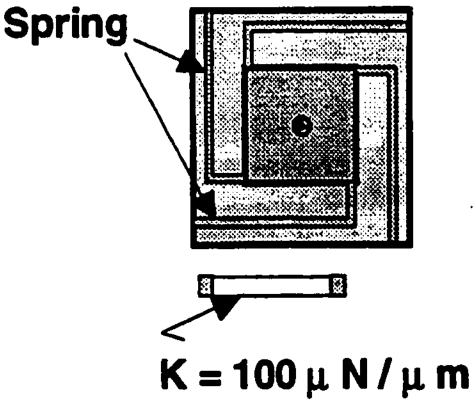

Fig. 2.8: A top view of the suspension system of the Hysitron transducer.

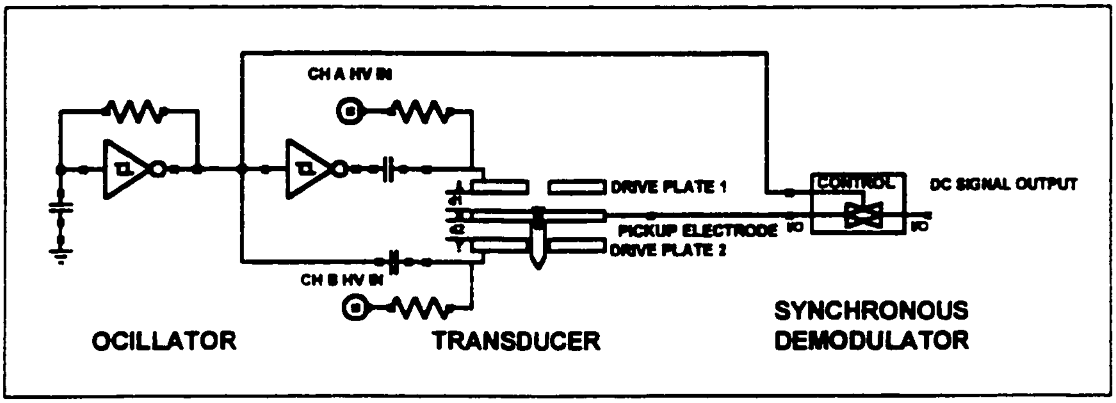

Fig. 2.9: A schematic diagram of the Hysitron transducer system

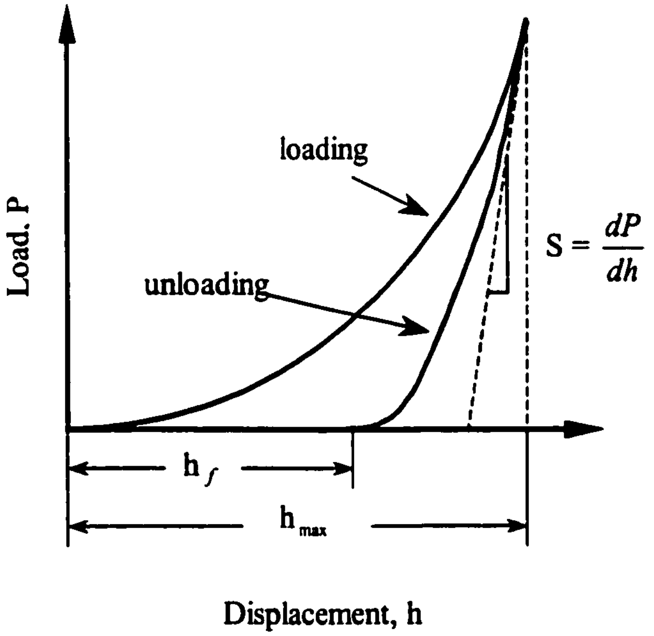

Fig. 2.10: A typical load/unload curve generated by the Hysitron Picoindenter.

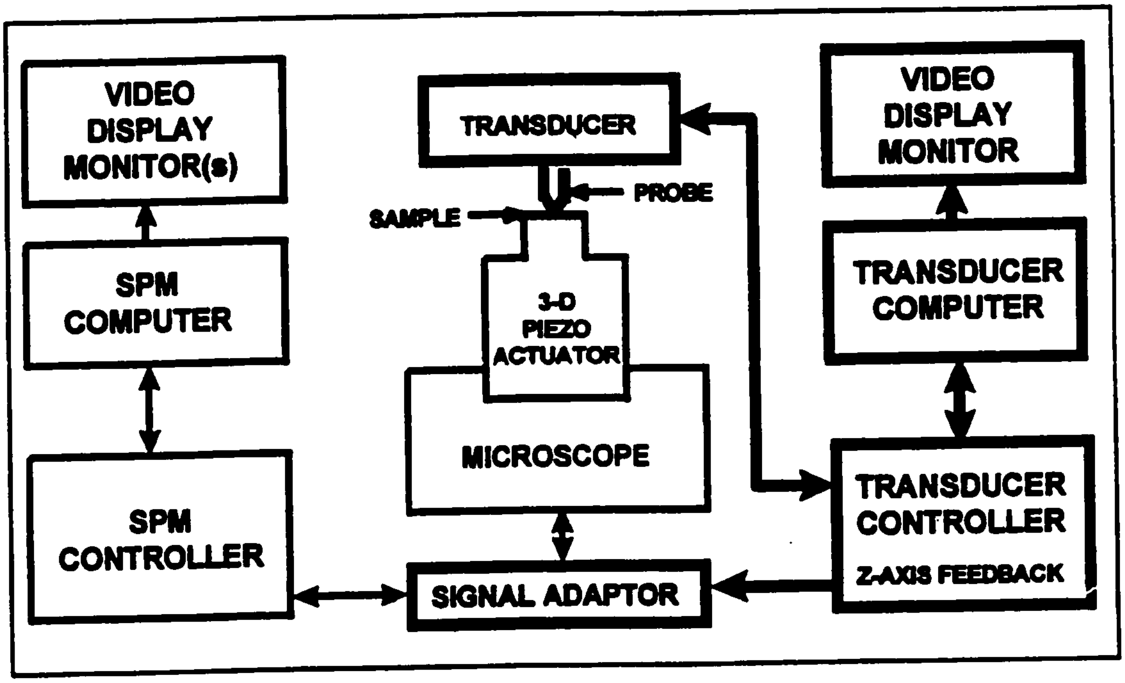

Fig. 2.11: Block diagrams for the Hysitron system used with SPM.

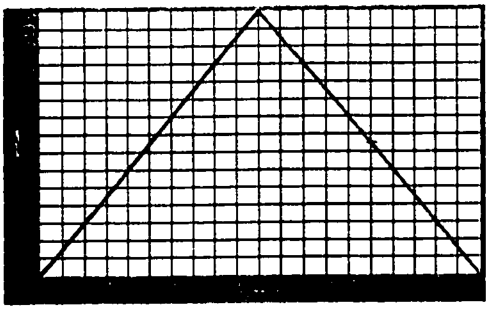

Fig. 2.12(a): a triangular loading function

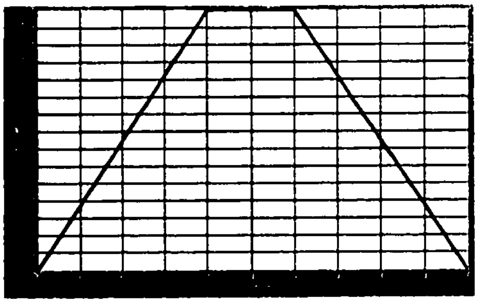

Fig. 2.12(b): a trapezoidal loading function

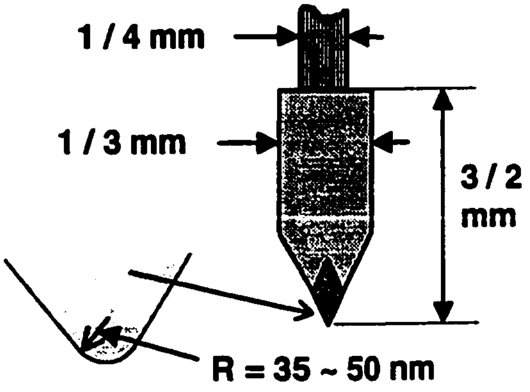

Fig. 2.13 (a): Description of a cube corner diamond indenter used in the experiments. The filled portion is the diamond tip. This is a three-sided pyramid with an apex angel of 90°.

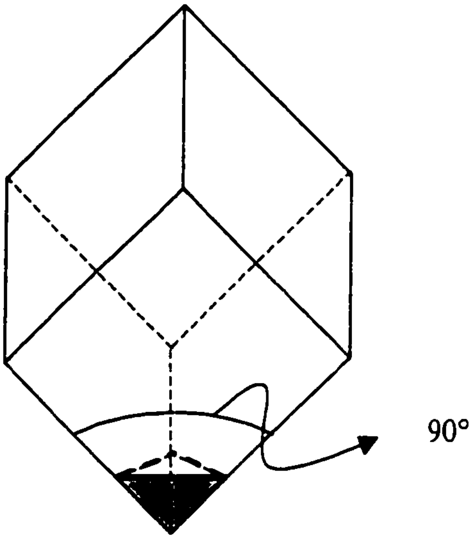

Fig. 2.13 (b): A deatailed view of the indenter assembly. A diamond tip is installed at the very end of the assembly.

Chapter 3

THEORETICAL ANALYSIS OF LOAD/UNLOAD CURVES

3.1 INTRODUCTION

This chapter focuses on the theoretical background of the analyses of load-unload/displacement curves obtained with the Hysitron Picoindenter. Since the initial stage of the unloading process is purely elastic, modified elastic theories are applied to the unloading curves. Two important mechanical properties of the specimen, hardness and reduced elastic modulus, can be obtained. However, before any theories are discussed, the definitions of hardness should be closely examined.

Hardness is often defined as the maximum load divided by the residual indentation area. Hardness itself is not a fundamental property of material, but rather a complex combination of properties such as elastic modulus, yield strength, ductility, work hardening, etc. Hardness is also understood as the resistance to plastic deformation. This resistance involves both elastic and plastic parameters. In most measurements, the residual areas are obtained with post-indentation scans by the SPMs, such as the PCM or the Hysitron Picoindenter. With the Hysitron Picoindenter we are able to calculate the contact areas at maximum loads. The maximum contact area is defined as the projected area on the specimen that makes contact with the indenter at maximum load. Thus, the contact area supports all the pressure exerted by the indenter in the form of normal stresses. Regions outside the contact area do not experience any normal stress in the direction parallel to the indenter motion. Figure 3.1 illustrates this concept schematically with an indenter with shape of a solid of revolution. Therefore, hardness is also defined as the maximum load divided by the maximum contact area. With this definition, hardness can be understood as the average normal stress supported under the indenter at the maximum load. As reported by Stilwell and Tabor (1961), the maximum contact area and the residual area are practically the same. Therefore, the two definitions should give similar hardness values.

Since the unloading curve is a measure of the material's elastic response while the load is withdrawing, the reduced elastic modulus - which will be defined in the next section - of the material can be estimated by assuming Poisson's ratio. Unlike hardness, the elastic modulus is well defined and is a fundamental material property. It provides more insight into the material. For a film/substrate system with similar film and substrate modulii, the film modulus can be extracted from the composite modulus by using Gao's (1992) method.

3.2 THEORETICAL ANALYSIS

3.2.1 Applicability of Sneddon's solutions to nanoindentation tests

Sneddon (1965) analytically solved for the elastic stress field within a homogeneous half space when it is indented by a flat, cylindrical, and rigid punch. Figure 3.2 illustrates Sneddon's problem. The boundary conditions in his problem are

$$u_3 = h, \text{ for } r = \sqrt{\left(x_1^2 + x_2^2\right)} \le a = \sqrt{\frac{A}{\pi}}, \tag{3.1a}$$

$$\sigma_{33} = 0, \text{ for } r > a, \tag{3.1b}$$

$$\sigma_{31} = \sigma_{32} = 0, \text{ for all } r \ge 0, \tag{3.1c}$$

where u_3 is the displacement component in the z direction; h is the vertical movement of the flat punch; σ_{ij} are the stress components; and a is the radius of the contact area, which is always a constant for the flat punch. Boundary condition (3.1a) simply states a geometrical constraint. Eq. (3.1b) requires the normal stress σ_{33} to vanish outside the contact area, and Eq. (3.1c) assumes a frictionless contact. In addition, the stress approaches zero when $r \to \infty$. He showed that the relationship between the load P and the penetration depth h is

$$P = \frac{4aGh}{1-\nu} \tag{3.2}$$

where G and ν are the shear modulus and Poisson's ratio of the half space, respectively. By differentiating P with respect to h, a simple relationship between the contact stiffness $S = \frac{dP}{dh}$, the contact area A, and the elastic modulus E is obtained as follows,

$$\frac{dP}{dh} = S = 2\sqrt{\frac{A}{\pi}}(\frac{E}{1-\nu^2}) \tag{3.3}$$

The relations, $G = \frac{E}{2(1+\nu)}$ and $A = \pi a^2$, have been invoked to obtain Eq. (3.3). The term $\frac{E}{1-\nu^2}$ is called the reduced modulus of the specimen, E_r. For a non-rigid indenter the reduced modulus can be generalized to

$$\frac{1}{E_r} = \frac{1-\nu^2}{E} + \frac{1-\nu_i^2}{E_i} \tag{3.4}$$

E_i *and* ν_i are the elastic modulus and Poisson's ratio of the indenter, respectively. For clarity Eq. (3.3) is restated below for elastically deformable indenters,

$$\frac{dP}{dh} = S = 2\sqrt{\frac{A}{\pi}}E_r \tag{3.5}$$

King (1987) studied the validity of Eq. (3.5) for triangular and square based pyramidal shape indenters by finite element analysis and concluded that Eq. (3.5) should be modified to

$$S = \frac{dP}{dh} = 2\sqrt{\frac{A}{\pi}}\beta E_r \tag{3.6}$$

where $\beta = 1.034$ for a triangular based pyramid and $\beta = 1.012$ for a square based pyramid. In addition, Oliver and Pharr (1992) theoretically extended the validity of Eq. (3.5) to the deformation behavior of an elastic half space with a flat surface indented by any punch that can be described as being in the shape of a solid of revolution from a smooth function. In other words, Eq. (3.5) can be used even when the contact area between the indenter and the specimen changes continuously as the indenter moves against the specimen. They also concluded that this method could be used at the atomic scale. Comparing Eq. (3.6) and Eq.

(3.5), we see that, $\beta = 1$ for circular cross section indenters. It is apparent that the deviation for the triangular and square geometries from the circular one is only 3.4% and 1.2%, respectively. Therefore, Eq. (3.5) can be used for elastic indentations by indenters that are triangular- and square-based pyramids without significant errors.

Indentations conducted in most experiments involve plastic deformation. Figure 3.3 shows a typical load/unload curve obtained with an indentation test. The deviation of the unloading curve from the loading curve represents a permanent indentation cavity. The depth of the cavity is called the residual depth and can be obtained from the intersection of the unloading curves and the abscissa. The existence of the residual cavity implies that the loading curve is plastic. In fact, as reported by Kral et al. (1993), yielding in tension occurs when the load is almost completely withdrawn. In other words, only the upper portion of the unloading curve is purely elastic in the entire indentation process. The limits of the upper portion of the unloading curves vary from material to material. Therefore, the only possibly legitimate point on the load/unload curve for Eq. (3.5) is the maximum load (or depth) point on the unloading curve. This fits the need to find the maximum contact areas, since hardness is defined as the maximum load divided by the maximum contact area. However, the geometry used to obtain Eq. (3.5) is still different from that used in most indentation tests.

In deriving Eq. (3.5), the specimen is modeled as a half space with a flat surface. However, the surface has already been indented plastically by the loading process. It is not a flat surface when the unloading process starts. In fact, the unloading process occurs in the indented cavity. The boundary conditions are different than those stated in Eqs. (3.1). Tabor

(1948) found experimentally that for a spherical indenter, the elastic load/displacement relation remains the same in a spherical indentation as for the half-space. A subsequent study by Stilwell and Tabor (1961) showed that the same relation holds for a conical indenter on a flat surface and in a conical cavity. Although they have verified two extreme cases, i.e. a very blunt one (spherical) and a very sharp one (conical), it requires more insight into the boundary conditions to generalize their findings to all indenters in the shape of solids of revolution.

Consider the schematic diagram depicted in Figure 3.4. The indenter is described as being in the shape of a solid of revolution of a smooth function $f(r)$. When the indenter is at its maximum penetration depth, h_m, the radius of maximum contact area is a_m. The stress field in the specimen is denoted as σ_{ij}, which includes any possible plastic and elastic components. The displacement fields are u_i, which also includes any possible plastic and elastic terms. The boundary conditions are as follows,

$$u_3 = h_m - f(r), \text{ for } r = \sqrt{\left(x_1^2 + x_2^2\right)} \le a_m = \sqrt{\frac{A_m}{\pi}}, \tag{3.7a}$$

$$\sigma_{33} = 0, \text{ for } r > a_m, \tag{3.7b}$$

$$\sigma_{31} = \sigma_{32} = 0, \text{ for all } r > 0, \tag{3.7c}$$

Eq. (3.7a) simply states the geometrical constraint that requires the surface of the specimen within the maximum contact area to be always in contact with the indenter. When the indenter is withdrawn infinitesimally from the maximum penetration, the penetration depth decreases from h_m to h. The change in the stress field and displacement field are denoted by

σ'_{ij} and u'_i, respectively. Both σ'_{ij} and u'_i contain only elastic components, since the unloading process is elastic in the early stages. The total stress and displacement fields are $\sigma_{ij} + \sigma'_{ij}$ and $u_i + u'_i$, respectively. The radius of the contact area is denoted by a. The following boundary conditions for the infinitesimal unloading must be satisfied:

$$u'_3 = h - f(r) - (h_m - f(r)) = h - h_m, \text{ for } r \le a_m, \tag{3.8a}$$

$$\sigma_{33} + \sigma'_{33} = 0, \text{ for } a < r \le a_m, \tag{3.8b}$$

$$\sigma_{33} + \sigma'_{33} = 0, \text{ thus } \sigma'_{33} = 0, \text{ for } r > a_m \tag{3.8c}$$

$$\sigma'_{31} = \sigma'_{32} = 0, \text{ for all } r > 0, \tag{3.8d}$$

Note that $u'_3 = h - h_m \to dh$. In addition, Stilwell and Tabor (1961) studied the change of contact area experimentally and concluded that there is an appreciable recovery in depth but there is practically no change in the diameter of the indentation after the load is withdrawn. Thus, the difference between a and a_m should be smaller than dh by orders of magnitude. Since, $\sigma_{33} = 0$ just outside the maximum contact area (Eq. (3.7b)), it is essentially zero in the area of $a < r \le a_m$ due to continuity of the stress fields. Thus, σ'_{33} vanishes for $a < r \le a_m$ according to Eq. (3.8b). Combining Eq. (3.8b) and Eq. (3.8c), Eqs. (3.8) are restated below:

$$u'_3 = h - h_m, \text{ for } r \le a, \tag{3.9a}$$

$$\sigma'_{33} = 0, \text{ for } r > a, \tag{3.9b}$$

$$\sigma'_{31} = \sigma'_{32} = 0, \text{ for all } r > 0, \tag{3.9c}$$

Therefore, Eqs. (3.9) each have the same form as Eqs. (3.1), which are the boundary conditions in Sneddon's solution. Since plastic deformation does not change the elastic properties of materials or the constitutive laws, solutions obtained with the boundary conditions in Eqs. (3.9) are the same as those with Eqs. (3.1). Therefore, Sneddon's solution is still valid for indentations in the indentation cavities, provided that the changes in contact area due to indenter withdrawals are negligible (at least at the early stage of withdrawal).

3.2.2 The contact area and the tip shape function

Next, we need to know that how much the indenter contacts the specimen at the maximum penetration, i.e. the maximum contact depth, as well as the exact indenter geometry. This allows us to determine the contact area and thus, the hardness and elastic modulus of the specimen. Figure 3.5 shows the geometry of an indentation cross-section and parameters for an elastic-plastic indentation. At any stage during the indentation, the total displacement h can be written as $h = h_s + h_c$ where h_s is the elastic displacement of the surface at the perimeter of the contact area and h_c is the contact depth. While the indenter is at its maximum penetration, the maximum depth, the surface displacement at the perimeter of the contact area, and the contact depth are h_m, h_{sm}, and h_{cm}, respectively. Again, the relation, $h_m = h_{sm} + h_{cm}$ still holds. The radius of the contact area is a_m at maximum load. After the load is fully withdrawn, the residual depth at the center of the indentation cavity is h_f. For a conical indenter, the relation between h_{sm}, h_m, and h_f can be determined by following Sneddon's solution,

$$h_{sm} = \frac{\pi - 2}{\pi}\left(h_m - h_f\right). \tag{3.10}$$

Also, $\left(h_m - h_f\right)$ is equal to $2P_m/S_m$ from Sneddon's load/displacement relation for conical indenters. Thus, we have the following relation,

$$h_{sm} = \frac{2}{\pi}(\pi - 2)\frac{P_m}{S_m} = \varepsilon\frac{P_m}{S_m} \tag{3.11}$$

In this case, $\varepsilon \approx 0.726$. Doing a similar calculation using Sneddon's solution, the values of ε are obtained for various indenter geometries. For example, $\varepsilon = 1.0$ for a flat, cylindrical punch and 0.75 for a paraboloid. The value of ε will be taken as 0.75 for our 90° cube-corner diamond indenters, since the paraboloid is the closest geometry to the triangular-based pyramid. As mentioned previously, an error of about 3% is expected with this assumption. Since h_m can be experimentally measured, the maximum contact depth, h_{cm}, is then calculated by subtracting h_{sm} obtained in Eq. (3.11) from h_m.

Since we assumed earlier that the surface of the specimen within the contact area is always in contact with the indenter, the contact area A can be related to the contact depth, h_c, if the indenter geometry is known. Thus, the contact area can be expressed as a function of h_c, i.e.,

$$A = A(h_c) \tag{3.12}$$

Note that the subscript m for h_c has been dropped for simplicity. Eq. (3.12) is called the area function or the tip shape function for an indenter. For a perfectly sharp cube-corner indenter, i.e. with a tip radius of 0, its tip shape function can be calculated as,

$$A(h_c) = 2.598h_c^2 \tag{3.13}$$

However, a practical indenter has a finite tip radius and its area function deviates from Eq. (3.13). The amount of deviation is obviously related to the tip radius. Correction terms are added to Eq. (3.13) to compensate for the deviation. The tip shape function for practical indenters becomes,

$$A(h_c) = 2.598h_c^2 + c_1 h_c + c_2\sqrt{h_c} + c_3\sqrt[4]{h_c} + c_4\sqrt[8]{h_c} + c_5\sqrt[16]{h_c} \tag{3.14}$$

Eq. (3.14) states a tip shape function for general indenters. Not all of the additional coefficients, $c_1 \ldots c_5$, are always needed. For very sharp cube-corner indenters, i.e. with tip radii smaller than 50 nm, only c_1 and c_2 are necessary. Since Eq. (3.14) is only an approximation to the real shape of the indenter, we suggest having at least two tip shape functions for one indenter, i.e. one for very shallow indentations and one for large indentations. Thus, the approximations can be more accurate for both shallow and deep applications. To find the coefficients of the correction terms, a series of indentations with various loads are done on standard samples such as fused quartz, whose elastic modulus and Poisson's ratio are 70 GPa and 0.3, respectively. Fused quartz is chosen as the standard sample because of its homogeneity and isotropy. For each indentation, the contact area is calculated from Eq. (3.5) with the obtained S at the maximum contact area and the known E_r. The contact depths are also calculated by using Eq. (3.11). Then, a curve of the contact area as a function of the contact depths is plotted. Coefficients c_1 through c_5 are determined by fitting Eq. (3.14) to the curve. This procedure is called tip shape calibration, and it must be done before any meaningful measurement can be made. Usually, 60 indentations are done for each calibration. Fig. 3.6 shows the tip shape function of tip 21 and the data obtained from calibration. Tip 21 is a cube-corner diamond tip with a radius of 62 nm. The technique for finding the tip radius will be discussed in Chapter 4. Since the tip shape function is obtained by fitting the calibration data in a certain range of contact depths (3 nm to 87 nm for the case of tip 21), it is only valid in that range. After obtaining the tip shape function for one particular tip, we can use it to find the contact areas for specimens and find their hardnesses and elastic modulii from Eq. (3.5).

It is worth noting that the usage of a tip shape function on all materials implicitly assumes a constant tip shape, i.e. a rigid indenter, although Eq. (3.5) is valid for non-rigid indenters. In most cases, the tip shape function remains the same while indenting on specimens. However, if the specimen is as hard as diamond, elastic or even plastic deformation of the diamond tip may occur. In this case, the tip shape function is no longer valid, since the shape of the tip has been changed. Unreasonably high hardness or elastic modulus (sometimes higher than those of diamond) may be obtained if the same tip shape function is used. Chapter 4 will discuss the method to compensate for the indenter elastic deformation while indenting on very hard materials. However, if the indenter is plastically deformed during an indentation test, its original shape is never recoverable. The indenter might still be usable with a new tip shape calibration. For some cases, the indenter cannot be calibrated anymore, since it is deformed so much that it cannot be approximated by a solid of revolution.

3.2.3 Determination of the initial unloading stiffness

In order to calculate E_r in Eq. (3.5), the stiffness at the maximum penetration of the unloading curve needs to be determined first. By definition, the stiffness is the slope of the unloading curve at maximum depth. However, the data obtained from experiments are discrete. A stiffness or a slope cannot be determined for discrete data. A function that fits the data is necessary so that the slope of the fitting function at the maximum penetration can be used as the stiffness. Although it is conceptually easy, significant errors may be generated if the unloading curve is not fitted correctly. Two fitting schemes are proposed here. In both methods, a curve is fitted to the upper portion (usually 40% to 100% of the maximum load) of the unloading curve.

Linear fit:

A linear function, of the form $P = c_1h+c_2$ is fitted to the chosen upper portion of the unloading curve by the least square method. The slope of this linear function is then the maximum stiffness. It turns out that the fitted line found in this way is not generally very close to the slope at the maximum load. This fitting line can only approximate the slope at maximum depth if a small upper portion on the unloading curve is chosen as the fitting range. Thus, the linear fit scheme is a first order approximation of the slope at the maximum depth. However, it is also the fastest and easiest way to roughly estimate the stiffness. For this reason, the linear fit scheme is adopted when a first order estimate of the stiffness is needed.

Power fit:

A power function of the form $P = c(h - h_f)^m$ is used to fit the upper portion of the unloading curve. The stiffness at maximum depth can be calculated by differentiating the function with respect to h. Since the power fit is more insensitive to the fitting range of the unloading curve and thus more accurate, it is adopted to calculate the stiffness in the measurements reported in the entire dissertation.

3.3 CORRECTION FOR THIN FILM INDENTATIONS

The Sneddon's problem considers the specimen as a homogeneous half space, i.e. a bulk. However, if indentation is performed on multi-layered or film/substrate systems, only the composite material properties are determined. Eq. (3.5) is restated below with the composite quantities.

$$\left.\frac{dP}{dh}\right|_{eff} = S_{eff} = 2\sqrt{\frac{A_{eff}}{\pi}}\left.E_r\right|_{eff} \tag{3.15}$$

Sneddon's solution is not able to separate the film properties (both hardness and elastic modulus) from the composite ones. To partially solve this problem, Doerner and Nix (1986) introduced an effective contact modulus, $[(1-\nu)/G]_{\text{eff}}$, expressed as some linear combination of the modulus of the film and the substrate. King (1987) adopted an integral equation analysis and modified Doerner and Nix's equation to fit his experimental results. Ramsey (1991) modeled the film/substrate system as a plate on an elastic foundation subjected to a point force. He discussed the cases for both small deflection and large deflection. Parallel to the above studies, finite element methods have also been used to simulate indentation tests (Bhattacharya and Nix (1988), Laursen and Simo (1992)). Lu and Bogy (1995) studied the effect of tip radius on hardness values of soft/hard (Al/Si) and hard/soft (Si/Al) thin film systems. Gao et al. (1992), applied a first order modulii-perturbation method to the multi-layer material problem. It is adopted to calculate the film elastic modulus when the modulii of the film and the substrate are similar. They assumed the film/substrate medium could be viewed as a homogeneous body originally made entirely of the substrate material subjected to a phase transformation in the film region. During the transformation the applied force P is kept constant, but the vertical displacement h and strain energy are allowed to change.

Energy conservation requires that the extra work done by the force *P* be equal to the energy change in the whole body. They then obtained the following effective shear modulus and Poisson's ratio,

$$G_{eff} = G_s + (G_f - G_s)I_0(\xi) \tag{3.16}$$

$$\nu_{eff} = \nu_s + (\nu_f - \nu_s)I_1(\xi) \tag{3.17}$$

where $\xi = t/a$, *t* is the film thickness and *a* is the radius of the contact area. The quantities with subscripts *s* belong to the substrate and the quantities with subscripts *f* belong to the film. The two interpolation functions I_0 and I_1 are given by

$$I_0(\xi) = \frac{2}{\pi}\tan^{-1}\xi + \frac{1}{2\pi(1-\nu)}\left[(1-2\nu)\xi\ln\left(\frac{1+\xi^2}{\xi^2}\right) - \frac{\xi}{1+\xi^2}\right] \tag{3.18}$$

$$I_1(\xi) = \frac{2}{\pi}\tan^{-1}\xi + \frac{\xi}{\pi}\ln\left(\frac{1+\xi^2}{\xi^2}\right) \tag{3.19}$$

Combining Eq. (3.16) and Eq. (3.17), the effective elastic modulus can be determined if we assume that the Poisson's ratios of the film and the substrate are similar. Eq. (3.20) briefly shows the derivation.

$$\begin{aligned} E_{eff} &= 2\left[\frac{E_f}{2(1+\nu_f)}I_0 + \frac{E_s}{2(1+\nu_s)}(1-I_0)\right]\cdot\left[1+\nu_f I_1 + \nu_s(1-I_1)\right] \\ &= E_s + (E_f - E_s)I_0 \end{aligned} \tag{3.20}$$

Thus, if the elastic modulus of the substrate is known, the elastic modulus of the film can be calculated with Eq. (3.20). Figure 3.7 shows a plot of the two interpolation functions, I_0 and

I_l. Since I_0 is a function of both ζ and ν, two I_0s with different values of ν were plotted. Note that both I_0 and I_l approach zero as ξ approaches 0 and one as ξ is about 100. I_0 reaches a value of 0.98 as ζ is about 10. This means that when the thickness of the film is ten times larger than the contact radius, the composite elastic properties obtained with Sneddon's solution can be viewed as the film elastic properties, i.e $t \geq 10a$. For a perfect cube-corner tip, i.e. its tip radius is 0, the contact radius can be related to the contact depth as,

$$a = \sqrt{\frac{2.598 h_c^{\ 2}}{\pi}} = \eta h_c^{\ 2}. \tag{3.21}$$

where η is 0.909. Substituting Eq. (3.21) into the inequality, we have the following,

$$h_c \leq \frac{t}{9.09} \Rightarrow \frac{h_c}{t} \leq 11.1\% \tag{3.22}$$

Eq. (3.22) provides a rule of thumb for the substrate effect of elastic modulus measurements by the nanoindentation techniques. In other words, nanoindentation measurements of elastic modulus of the film and substrate systems do not experience the influence from the substrates if the contact depths are kept below 11% of the film thickness. Note that the estimation in Eq. (3.19) is based on a perfect tip. For a practically used tip, i.e. its tip radius is finite, its η is larger than 9.09. Hence, the contact depths have to be kept below 11% of the film thickness to avoid the substrate effects on the elastic modulus measurements. Since the contact depth is always larger than the residual depth for an indentation, the residual depth has to be kept to an even smaller percentage of the film thickness to avoid the substrate effects. It is worth noting that this rule does not apply to the substrate effects on the hardness measurements by using the nanoindentation techniques, since it is not sufficient to determine the form of A_{eff} with Eq. (3.15) and Eq. (3.2). The substrate effect of hardness measurements is expected to be different, since hardness involves not only the elastic properties, but also the plastic properties such as yield strength, ductility, work hardening, etc. It will be studied in Chapter 5 with the indentation hysteresis technique.

3.4. SUMMARY AND CONCLUSIONS

Sneddon's solution for the elastic field in a homogeneous half space indented by a flat punch is examined and discussed. It is then extended to nanoindentation tests with indenters of solids of revolution or triangle- and square-based pyramidal indenters by manipulating the boundary conditions. Since Sneddon's solution provides an equation with two unknowns (A and E_r in Eq. (3.5)), it is not a determinate system of equations. A tip calibration procedure on fused quartz is needed to establish an additional equation for the contact area A and thus, to close the system of equations. Hence, the hardness and elastic modulus of the specimen can be obtained by applying Sneddon's solution at the maximum penetration point on the unloading curve. By doing the tip shape calibration, the shape of the tip is implicitly assumed unchanged from specimen to specimen. Therefore, this procedure is only useful when the tip geometry does not change during indentations. If the tip shape changes plastically, a new tip calibration has to be done before any meaningful measurement is made. If the tip only deforms elastically, a compensation procedure is developed in Chapter 4. No additional tip calibration procedure is needed.

The substrate effect is a major concern in the nanoindentation measurements, especially for films of 20 nm or less. Insights into the substrate effects for the elastic modulus measurements are discussed by using Gao's solution for elastic fields of the film and substrate systems. For a perfect cube-corner tip, the contact depth should be kept below 11% of the film thickness to avoid any influence from substrates. This percentage is even smaller for a tip with a finite radius. The substrate effect for hardness measurements is not retrievable, and it will be discussed with the indentation hysteresis techniques in Chapter 5.

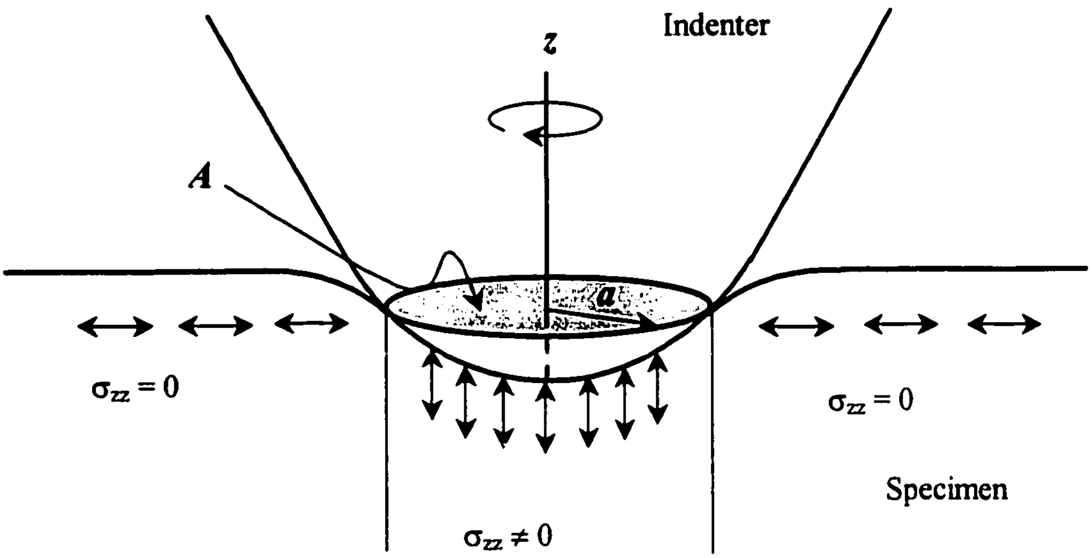

Fig. 3.1: A schematic diagram of an indentation by an indenter of solid of revolution on a flat surface. *A* is the maximum contact area and *a* is the maximum contact radius. The region under the contact area is loaded with σ_{zz} and the regions out the contact area are not.

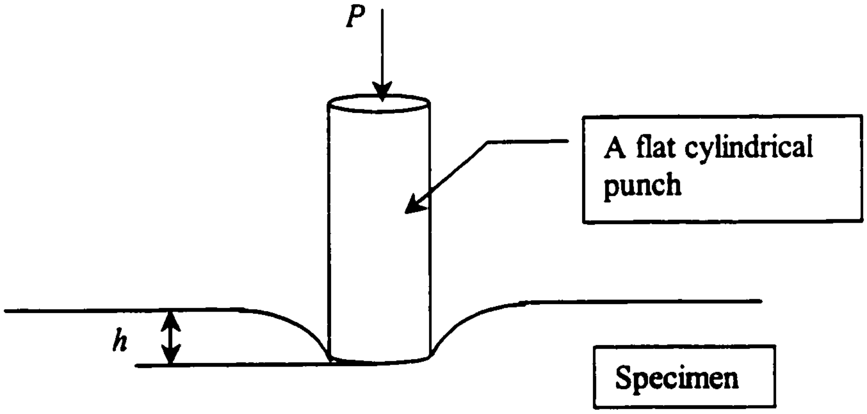

Fig. 3.2: An illustration of the Sneddon's problem. The indenter is modeled as a flat cylindrical punch and the specimen is homogeneous and isotropic. Note that the contact area is always a constant and equals to the area of the end of the cylinder.

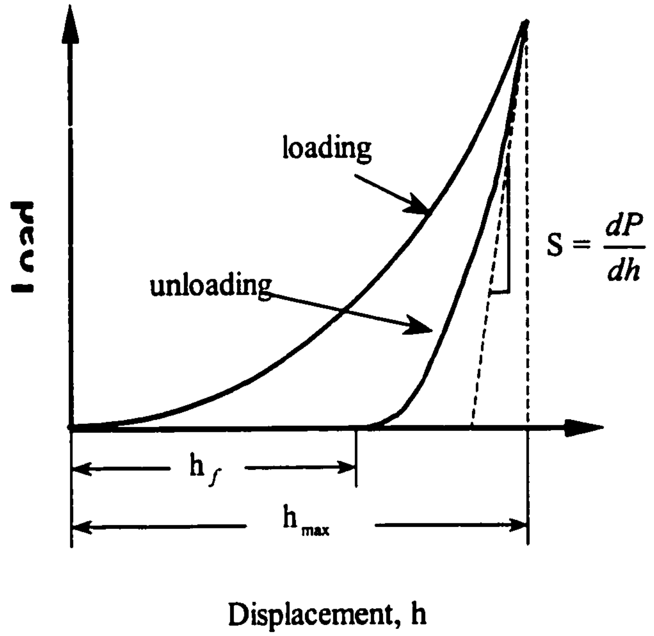

Fig. 3.3: A schematic diagram of a typical load/displacement curve for an indentation.

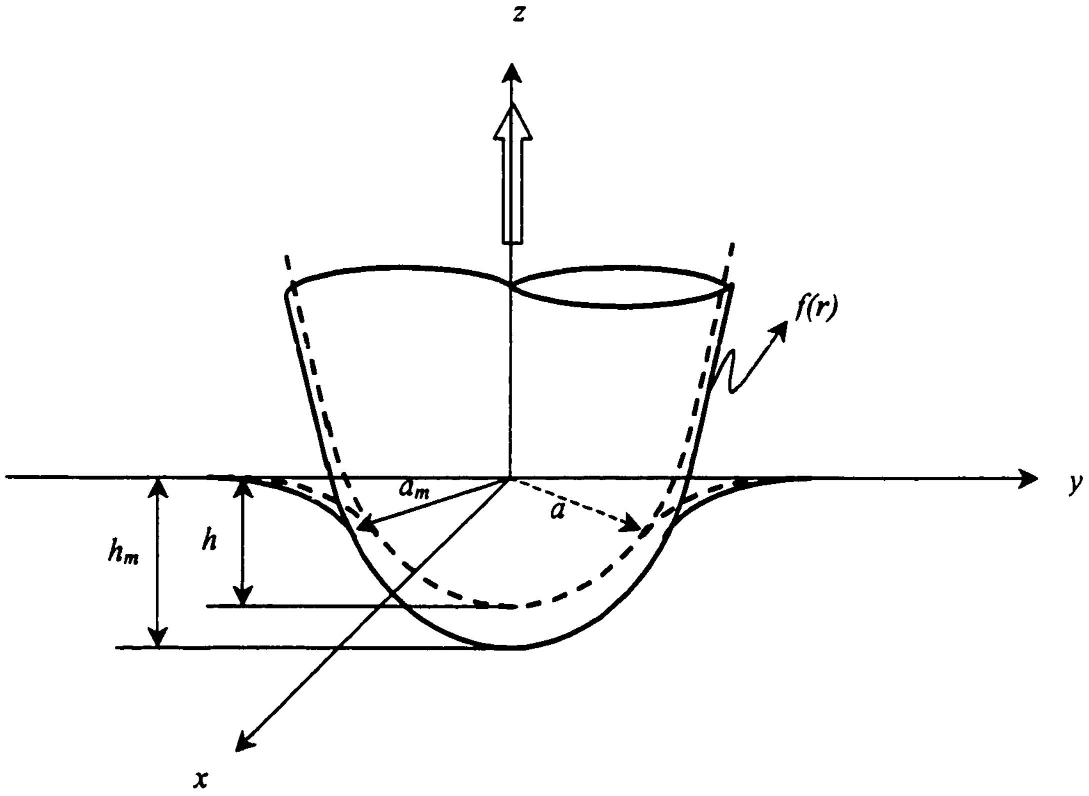

Fig. 3.4: An infinitesimal withdrawal of the indenter. The penetration depth changes from h_m to h, while the radius of the contact area changes from a_m to a.

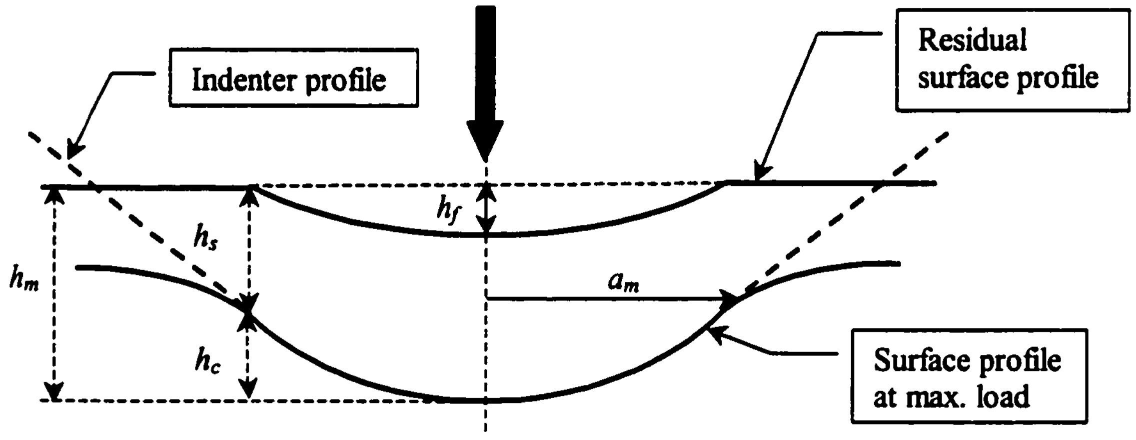

Fig. 3.5: The geometry of an indentation cross-section and parameters of an elastic-plastic indentation.

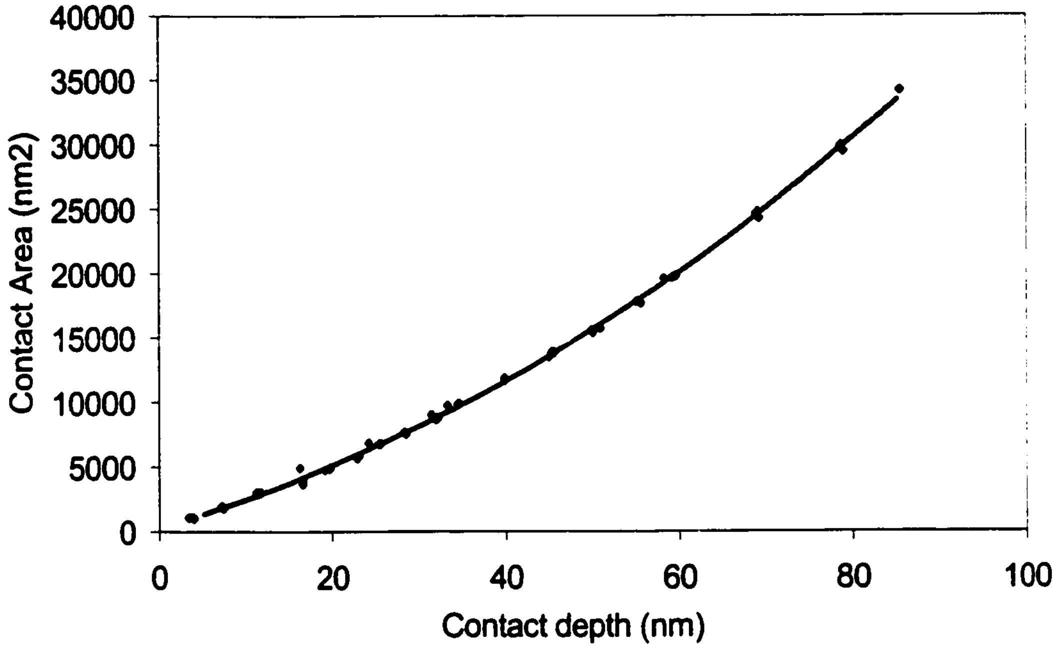

Fig. 3.6: the tip shape function for tip 21.

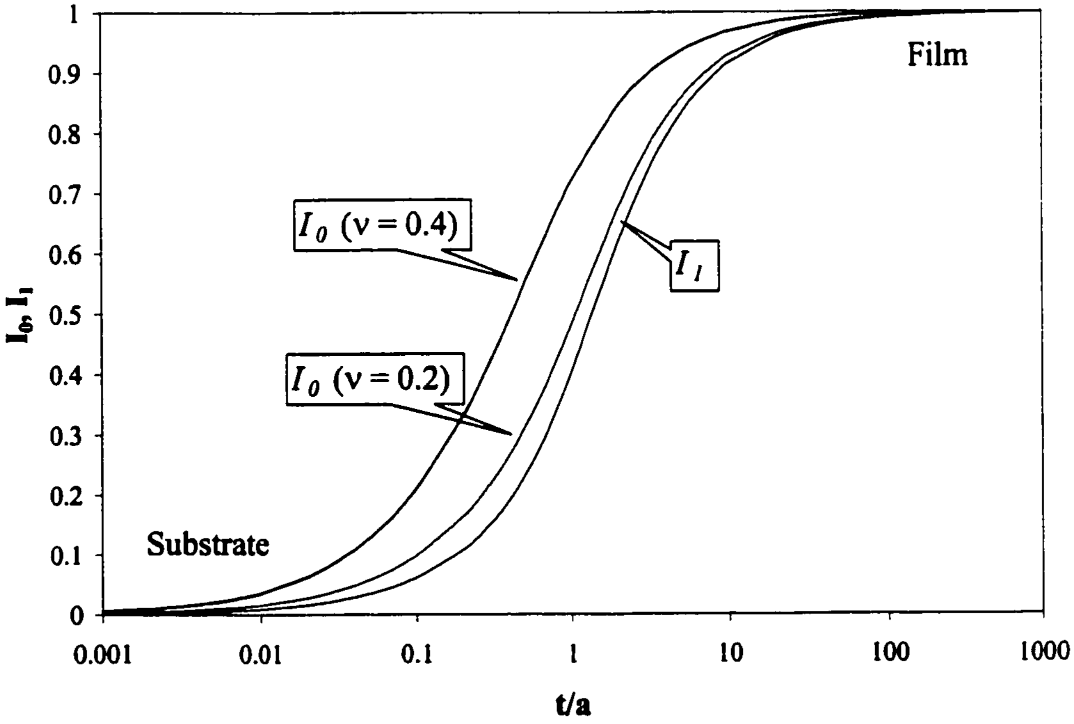

Fig. 3.7: I_0 and I_1 function

Chapter 4

COMPENSATING FOR INDENTER DEFORMATION WHILE INDENTING ON HARD MATERIALS

4.1 INTRODUCTION

The demand for higher areal storage density for disk drives has driven the development of thinner and harder protective films for disks and sliders. Nanoindentation tests have been widely adopted to study the mechanical properties, such as hardness and modulus of these films. The modified Sneddon's solution for an elastic field within a homogeneous half space indented by a solid of revolution is usually used to analyze the load/displacement curves obtained from experiments. Indenters are implicitly treated as rigid bodies by using a fixed tip shape function. (This point will be explained in detail later in this chapter.) When indenting on materials with hardnesses of 50GPa or lower a diamond indenter can be treated as a rigid body and no appreciable errors will be introduced. However, if indentations are made on much harder materials such as, for example, the recently developed cathodic-arc amorphous carbon films, the diamond indenter deforms during the indentation processes. As the demand for higher performance protective films for disk drives continues, even harder materials will be developed. The current method of analysis will then fail to predict the right hardness and modulus values. A new technique is needed to compensate for the diamond indenter deformation during indentation.

The new method proposed here is based on the Hertz contact theory for elastic solids. The hardness values for the cathodic-arc amorphous carbon films calculated by this method are compared with the values predicted by Sneddon's solution and those from the finite-element simulation obtained by Follstaedt et al. (1997). Together with the Sneddon method, the new method is able to estimate the indenter tip radius by a series of indentations on fused Quartz.

Indentation tests in this chapter were made by the Hysitron single-axis tester, which is a commercially available nanomechanical test instrument described in Chapter 2. The software version 3.0 was used to record and to analyze the data according to Sneddon's solution. A triangle-based pyramid-shaped (Cube corner) diamond indenter with a tip radius of about 160nm was used. Cathodic-arc amorphous carbon films were used for obtaining samples with hardness near that of diamond.

4.1.1 Review of the current method

The current method of analyzing the load/displacement curve is based on Sneddon's (1965) solution for an elastic stress field within a homogeneous half space when it is indented by a rigid flat punch. It is discussed in detail in Chapter 3. He derived a simple relationship between the contact stiffness S, the projected area of indentation (or, the contact area) A, and the elastic modulus E of the indented material, i.e.

$$\frac{dP}{dh} = S = 2\sqrt{\frac{A}{\pi}}\left(\frac{E}{1-\nu^2}\right), \qquad (4.1)$$

where P and h are the load and displacement of the indenter, while ν is the Poisson's ratio of the indented material. For elastically deformable indenters, the term in the parenthesis can be generalized to the reduced modulus E_r, which is defined as

$$\frac{1}{E_r} = \frac{1-\nu^2}{E} + \frac{1-\nu_i^2}{E_i}. \tag{4.2}$$

Thus, Eq. (4.1) can be re-written as

$$S = 2\sqrt{\frac{A}{\pi}}E_r. \tag{4.3}$$

Pharr et al. (1992) extended this expression to the deformation behavior of an elastic half space indented by any punch that can be described as a solid of revolution of a smooth function. Therefore, Eq.(4.3) can be used to analyze the load-unload/displacement curves obtained from indentation experiments with non-flat indenters. A detailed discussion of the validity of Sneddon's solution is provided in Chapter 3. Fig. 3.3 shows a typical load/unload curve for a non-flat indenter with definitions of load (P), indentation depth (h), maximum depth (h_{max}), residual depth (h_{res}), and stiffness (S).

The contact stiffness S in Eq.(4.3) can be calculated from the unloading curve for each indentation. Therefore, we have two unknowns involved in Eq. (4.3), the contact area A and the reduced modulus E_r. So it is an indeterminate system. The system becomes determinate if we introduce a tip shape function, which is the relation between the contact depth and contact area, $A = A(h_c)$, i.e., the shape of the assumed rigid tip. The tip shape function can be found by a series of indentations on materials with homogeneous and isotropic mechanical properties, for example, fused Quartz. Since the reduced modulus of diamond and fused Quartz is known, the contact area of each indentation can be calculated from Eq. (4.3). According to Sneddon's solution the contact depth can also be calculated for the same indentation. The tip shape function can thereby be established. Equation (4.3) together with the tip shape function constitute a closed system.

4.1.2. Problem associated with the current method

Finding the tip shape function on fused Quartz implicitly assumes that the tip shape is a fixed geometry. This is true if the tip is made of diamond and indentations are on relatively soft materials. For most materials used in disk drive applications, for example, silicon, silicon carbide, silicon nitride, hydrogenated carbon, nitrogenated carbon, etc., the method predicts hardness and modulus values quite well. However, if indentations are made on the recently developed cathodic-arc amorphous carbon films whose hardnesses are close to that of diamond, this method fails to predict the right hardness and modulus values. In fact, since the tip deforms to increase the contact area between itself and the indented material, this method underestimates the contact area and thus, overestimates the hardness and modulus, according to the definition of hardness and Eq.(4.3). A new method that accounts for indenter deformation during indentation is needed to solve the problem.

4.2 COMPENSATING FOR ELASTIC INDENTER DEFORMATION

4.2.1 Theoretical background (Johnson 1985)

When two solids are brought into contact they initially touch at a single point or along a line. As the contact force increases they deform near their points of first contact. Figure 4.1 shows a schematic diagram of this concept. The solids are shown as convex for convenience. They could be of any shape as long as they are topographically smooth. The point of first contact is taken as the origin of a rectangular coordinate system. The common tangent plane at the origin is taken as the *x-y* plane. The z-axis is chosen to coincide with the common normal to the surfaces at the origin. The sense of the z-axis is chosen to point to Body One. Before any interaction of these two solids occurs, the profile of each surface near the origin can be expressed approximately in the form,

$$z = Ax^2 + By^2 + Cxy + \dots, \tag{4.4}$$

where higher order terms are neglected. The separation between the two surfaces is given by

$$s = z_1 - z_2 = A_1x^2 + B_1y^2 + C_1xy - \left(A_2x^2 + B_2y^2 + C_2xy\right) = A'x^2 + B'y^2 + C'xy\,. \tag{4.5}$$

where $A' = A_1 - A_2$, etc. By properly choosing the x, y axes, we can make $C' = C_1 - C_2$ zero, and hence

$$s = A'x^2 + B'y^2 = \frac{x^2}{2R'} + \frac{y^2}{2R''}, \tag{4.6}$$

where A' and B' are positive constants and R' and R'' are defined as the principal relative radii of curvature. A' and B' can be written in terms of R' and R'' by,

$$A' + B' = \frac{1}{2}\left(\frac{1}{R'} + \frac{1}{R''}\right) = \frac{1}{2}\left(\frac{1}{R_1'} + \frac{1}{R_1''} + \frac{1}{R_2'} + \frac{1}{R_2''}\right), \tag{4.7}$$

and

$$B' - A' = \frac{1}{2}\left\{\left(\frac{1}{R'_1} - \frac{1}{R_1''}\right)^2 + \left(\frac{1}{R'_2} - \frac{1}{R_2''}\right)^2 + 2\left(\frac{1}{R'_1} - \frac{1}{R_1''}\right)\left(\frac{1}{R'_2} - \frac{1}{R_2''}\right)\cos 2\alpha\right\}^{1/2} \tag{4.8}$$

where R_1' and R_1'' are the principal radii of curvature of the first surface at the origin and R_2' and R_2'' are the principal radii of curvature of the second surface at the origin while α is the angle between the axes of principal curvature of each surface. If the bodies can be described as solids of revolution with respect to the origin, then $R_1' = R_1'' = R_1$ and $R_2' = R_2'' = R_2$, and therefore, $A' = B' = ½(1/R_1+1/R_2)=1/2R$. It follows that the separation between the two surfaces can be simplified as

$$s = \frac{1}{2R}\left(x^2 + y^2\right) = \frac{r^2}{2R}. \tag{4.9}$$

where $r = \left(x^2 + y^2\right)^{1/2}$. Figure 4.2 shows the geometry of two solids of revolution in contact under the application of a normal load P. u_{z1} and u_{z2} are the displacements of points S_1 on surface 1 and S_2 on surface 2 due to the contact pressure. h_1 and h_2 are the displacements of distant points in the two bodies T_1 and T_2. a is the radius of the contact circle. After deformation, if the points S_1 and S_2 coincide with each other within the contact surface, then

$$u_{z1} + u_{z2} + s = h_1 + h_2 = h, \tag{4.10}$$

where h is the relative displacement of two distant points T_1 and T_2. Equation (10) has to be satisfied for all points within the contact circle, i.e. for $0 \le r \le a$, where a is the contact radius, i.e. the radius of the contact circle (see Fig. 4.2).

Next we consider the contact of two bodies of special shapes: one is a solid of revolution (the indenter) and the other is a homogenous half space with a flat surface (the specimen). Thus, R_1 is the tip radius at the origin and $R_2 \to \infty$. From Eq.(4.9), the separation of S_1 and S_2 before deformation is

$$s = \frac{r^2}{2R_1}. \tag{4.11}$$

Therefore, Eq. (4.10) becomes

$$u_{z1} + u_{z2} = h - \frac{r^2}{2R_1}. \tag{4.12}$$

The pressure distribution obtained by Hertz, which results in displacements satisfying Eq. (4.12), is given by

$$p = p_0\left[1-\left(\frac{r}{a}\right)^2\right]^{1/2}, \; r \le a, \tag{4.13}$$

where p_0 is the maximum pressure. Hertz also showed that the normal displacement induced by this pressure distribution is

$$u_z = \frac{1-\nu^2}{E}\frac{\pi p_0}{4a}\left(2a^2 - r^2\right), \; r \le a. \tag{4.14}$$

Equation (4.14) is valid for both bodies. Subscripts have been dropped for convenience. Therefore, Eq. (4.12) can be written as,

$$u_{z1} + u_{z2} = \left(\frac{1-\nu_1^2}{E_1} + \frac{1-\nu_2^2}{E_2}\right)\frac{\pi p_0}{4a}\left(2a^2 - r^2\right) = \frac{\pi p_0}{4aE_r}\left(2a^2 - r^2\right) = h - \frac{r^2}{2R_1}, \tag{4.15}$$

where E_r is the reduced modulus as defined in Eq.(4.2). Again, Eq. (4.15) is valid for all r smaller than a. Re-arranging Eq. (4.15), we have

$$h = \frac{\pi p_0}{4aE_r}\left(2a^2 - r^2\right) + \frac{r^2}{2R_1}, \tag{4.16}$$

where *h* and *a* are variables independent of *r*. Since the left hand side of Eq. (4.16) is not a function of *r*, the right hand side also cannot be a function of *r*. Therefore, the coefficient of r^2 must vanish, and we have

$$\frac{\pi p_o}{4aE_r} = \frac{1}{2R_1}, \tag{4.17}$$

or,

$$a = \frac{\pi p_0 R}{2E_r}. \tag{4.18}$$

Note that the subscript 1 of *R* has been dropped for simplicity. Substituting Eq. (4.18) back to Eq. (4.16), we obtain

$$h = \frac{\pi a p_0}{2E_r} = \frac{a^2}{R}. \tag{4.19}$$

The total load can also be calculated by integrating the pressure over the contact area, i.e.,

$$P = \int p(r) 2\pi r dr = \frac{2}{3} p_0 \pi a^2. \tag{4.20}$$

Substituting for p_0 by $\frac{3}{2}\frac{P}{\pi a^2}$ into Eq.(4.18) and Eq. (4.19), we have

$$a = \left(\frac{3PR}{4E_r}\right)^{1/3}, \tag{4.21}$$

$$h = \frac{a^2}{R} = \left(\frac{9P^2}{16RE_r^2}\right)^{1/3}. \tag{4.22}$$

The second equality in Eq. (4.22) can be re-written as,

$$P = \frac{4}{3} E_r \sqrt{Rh^3}. \tag{4.23}$$

Taking the first derivative of P with respect to h, we obtain

$$\frac{dP}{dh}=2E_r\sqrt{Rh}=2aE_r=2\sqrt{\frac{A}{\pi}}E_r, \tag{4.24}$$

in which the first equality of Eq. (4.22) and $A = \pi a^2$ have been invoked. Equation (4.24) is the same as Eq. (4.3), which is derived from Sneddon's solution. Thus, Eq. (4.3) can be derived from Hertz contact theory for the elastic stress field within a homogenous half space indented by any punch that can be described as a solid of revolution of a smooth function.

The restrictions of this derivation are that the contact radius has to be much smaller than the tip radius as well as the lateral and axial dimensions of the two bodies. That is to say $a \ll R$, and $a \ll l$, where l represents the lateral and axial dimensions of the bodies. These restrictions are easily satisfied in the specimen side. However, if indentations are made on the nanometer scale, care is needed in applying these equations, since the restrictions may not be satisfied. A detailed discussion will be provided in the next subsection.

4.2.2 Accounting for elastic deformation of the indenter

Equation (4.22) and Eq. (4.24), which are re-written below, constitute a determinate system for E_r and a (or A), unlike the results from Sneddon's solution, from which only Eq. (4.3) can be obtained.

$$h=\frac{a^2}{R}=\frac{A}{\pi R} \tag{4.22}$$

$$\frac{dP}{dh}=S=2\sqrt{\frac{A}{\pi}}E_r \tag{4.24}$$

Equation (4.22) states a linear relation between the contact area A and the indenter displacement h, which can be measured experimentally, as long as R is a constant. Since the tip radius R is defined at the origin a constant R indicates that the deformation is localized in the vicinity of the origin. Besides, there are only geometric parameters, instead of material properties, involved in Eq. (4.22). This means that Eq. (4.22) is valid for all materials with the same geometry parameters. That is to say, Eq. (4.22) is only tip dependent. If we can obtain the relation between the indenter displacement and the contact area on one material for a particular tip this relation holds for all materials provided that indentations are done within the restrictions.

There are two approaches for obtaining the relation between indentation depth and the contact area for a particular tip. The first one is based on a known tip radius. By substituting the tip radius into Eq. (4.22) we can construct the relation between the indentation depth and the contact area. The tip radius is usually estimated from SEM pictures of the region near the origin (Lu and Bogy 1994). However, this is often a lengthy and expensive process. The accuracy of this method is also a concern. The second approach for getting the indentation depth and contact area relation is to indent on any homogeneous and isotropic material, for example fused Quartz, for a range of indentation depths. Contact areas can be calculated by the method mentioned in Chapter 3, since no appreciable deformation is expected if a diamond tip is used. Indentation depths can be easily read out from the load-unload/displacement curve obtained from each indentation test. Figure 4.3 shows the contact area vs. the indentation depth for a typical indenter, tip 47. The curve is not linear over the entire range (0 – 250 nm). This means that the tip radius R is not a constant within the range shown, and thus the Hertz solution is not applicable. However, if we consider only the lower part of the curve, for example, for indentation depths less than 85nm, the curve can be fitted by a linear function in that range without experiencing large errors, as shown in Fig. 4.4. Thus, the technique based on the Hertz contact theory is valid in this range of indentation depths. This range is called the working range. After obtaining the fitted linear function for the area vs. depth curve we can calculate the tip radius by dividing the slope of the function by π. In the case of tip 47, its tip radius with respect to the origin is 160 nm. Determining tip radii by this approach involves only a simple calculation.

After Eq. (4.22) has been used for a particular tip indentation tests can then be conducted for materials as hard as the diamond indenter. For each indentation the maximum depth can be read out from the load-unload/displacement curve (see Fig. 3.3). Substituting the maximum depth into Eq. (4.22) we can calculate the maximum contact area. Thus, the hardness, which is defined as the maximum indentation force divided by the maximum contact area, can be calculated. Besides, the slope S_{max} (Stiffness of the unloading curve at maximum indentation force) for the unloading curve at the maximum depth can be calculated by approaches discussed in Chapter 3. Substituting S_{max} and the maximum contact area into Eq. (4.24) we can calculate the reduced modulus at the maximum depth.

Next, we need to determine if it is sufficient to consider only the elastic deformation of the indenter. Figure 4.5 shows the hardness measurement of fused Quartz using tip 47 before and after indenting on a cathodic-arc amorphous carbon film (cathodic-arc DLC film) whose hardness is close to that of diamond. The hardness values were calculated by the method mentioned in Sec. 1 with the tip shape function obtained before the test, since no significant deformation of the diamond indenter is expected while indenting on fused Quartz. The same tip shape function was used in the calculation before and after indenting. If the indenter had experienced plastic deformation or other damage during indenting on the cathodic-arc DLC film the tip shape would have changed permanently, and so the tip shape function would have changed. However, according to the data shown there is no significant difference in the measured hardness before and after indenting on the cathodic-arc DLC film. This indicates that the tip shape did not change permanently. Therefore, it is sufficient to consider only the elastic deformation of the diamond indenter.

4.3 EXPERIMENTS

Figure 4.6 shows the hardness values for a cathodic-arc amorphous carbon film with a thickness of 500nm, which was deposited under –100V substrate bias. Note that the abscissa is the residual depth, instead of the indentation depth. The empty triangles represent the hardness data calculated by the method based on Sneddon's solution. The solid triangles show the hardness data calculated by the new technique based on the Hertz contact theory. The data plotted are within the working range of the theory, i.e. the maximum indentation depths are smaller than 85nm. The values represented by the empty triangles are significantly higher than the ones represented by the solid triangles. The relatively low hardness at the film surface is due to predominant sp^2 bonding near the surface (Monteiro et al. 1997). A similar phenomenon has been reported by Pharr et al. (1996).

Follstaedt et al. (1997) employed a finite element technique to calculate the hardness and the modulus of thin film. They matched the finite-element-simulated load-unload/displacement curve with the experimentally observed load-unload/displacement curve by varying the film elastic modulus and yield strength. They obtained a hardness of 68.4 ± 2.5 GPa at a residual depth of around 30nm. This result appears to agree with the data shown in Fig. 4.6. Figure 4.7 shows the reduced modulus values for the same film. The empty symbols show higher values than the solid symbols. Note that the difference in the reduced modulus between these two methods is not as much as that in hardness. This is because the reduced modulus depends only on the square root of the contact area in Eq. (4.24), while the hardness depends on the contact area itself. Note that the values shown on Fig. 4.7 are the reduced modulus of the film/indenter system. Substituting the elastic parameters for diamond (E = 1140GPa and $\nu = 0.07$) into Eq. (4.2), we find that $\frac{E}{1-\nu^2}$ for the film itself is about 500GPa. Assuming that the Poisson's ratio equals 0.25, we can roughly estimate the elastic modulus of the film to be 470GPa. However, the simulated result reported by Follstaedt *et al* is 848 ± 10 GPa at a residual depth of 30nm. No explanation is available at this point for the inconsistency. Figures 4.8 and 4.9 show the hardness and modulus values of a different cathodic-arc amorphous carbon film, which was deposited under –2000V substrate bias. In this case the values represented by the empty symbols are not significantly different from those shown by the solid symbols. This indicates that if there is no deformation of the indenter the technique based on the Hertz contact theory predicts the same hardness and modulus values as the methods mentioned in Chapter 3. The relatively low hardness values at the film surface are explained by the same argument as provided for the other film. According to the data shown in Fig. 4.8 this film exhibits a hardness of 25GPa at a residual depth of 40nm, which agrees well with the value (27.5 ± 0.7 GPa) reported by Follstaedt *et al.* The elastic modulus at 40nm residual depth can be roughly estimated to be 300GPa by the same approach as mentioned above. This number is not far from the modulus (360GPa ± 10GPa) reported by Follstaedt *et al*, unlike the modulus for the film deposited under –100V substrate bias. Knapp et al. (1998) have a detailed discussion of their simulation techniques.

4.4 SUMMARY AND CONCLUSIONS

Sneddon's solution can be derived from the Hertz contact theory (Eq. (4.24)). The relation between the contact area, indentation depth, and tip radius can be obtained (Eq. (4.22)). The system of equations derived from the Hertz contact theory is determinate. No extra assumption is necessary, for example, such as a constant tip shape, to close the system. Thus, the method proposed here is able to account for the indenter elastic deformation if indentations are made on materials as hard as the indenter. If a diamond indenter is used it is sufficient to consider only the elastic deformation according to experimental experiences. Besides, the tip radius at the origin can also be calculated if the contact areas are known. No special equipment and time-consuming processes are needed.

The method proposed here yields lower hardness and modulus values for very hard materials than those calculated by the method based on Sneddon's solution. This is due to underestimation of the contact area in the latter case and thus overestimation of hardness and modulus. The method proposed here shows almost the same hardness and modulus values when indenting on soft materials as the method based on Sneddon's solution. This is because indenter deformation is negligible while indenting on soft materials. The hardness and modulus values calculated by this method agree with the finite-element-simulated results by Follstaedt *et al*, except for the modulus of the film deposited at −100V substrate bias. No explanation can be found for the one inconsistency.

Finally, it is also possible to integrate this technique into commercial software for analyzing load-unload/displacement curves. The corrected hardness and reduced modulus values can be calculated in seconds, rather than hours or days if done by the finite-element simulation.

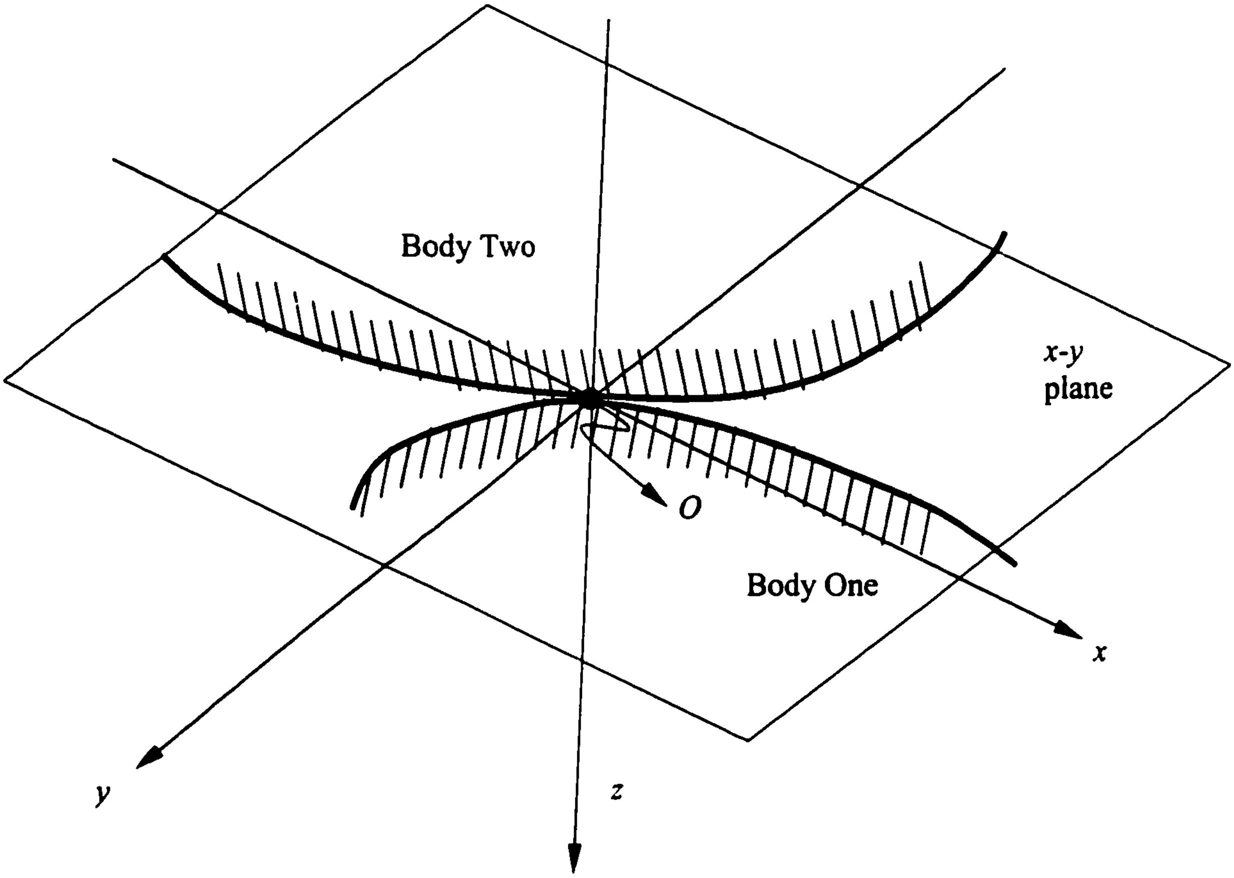

Fig. 4.1: A schematic diagram for two bodies at first contact

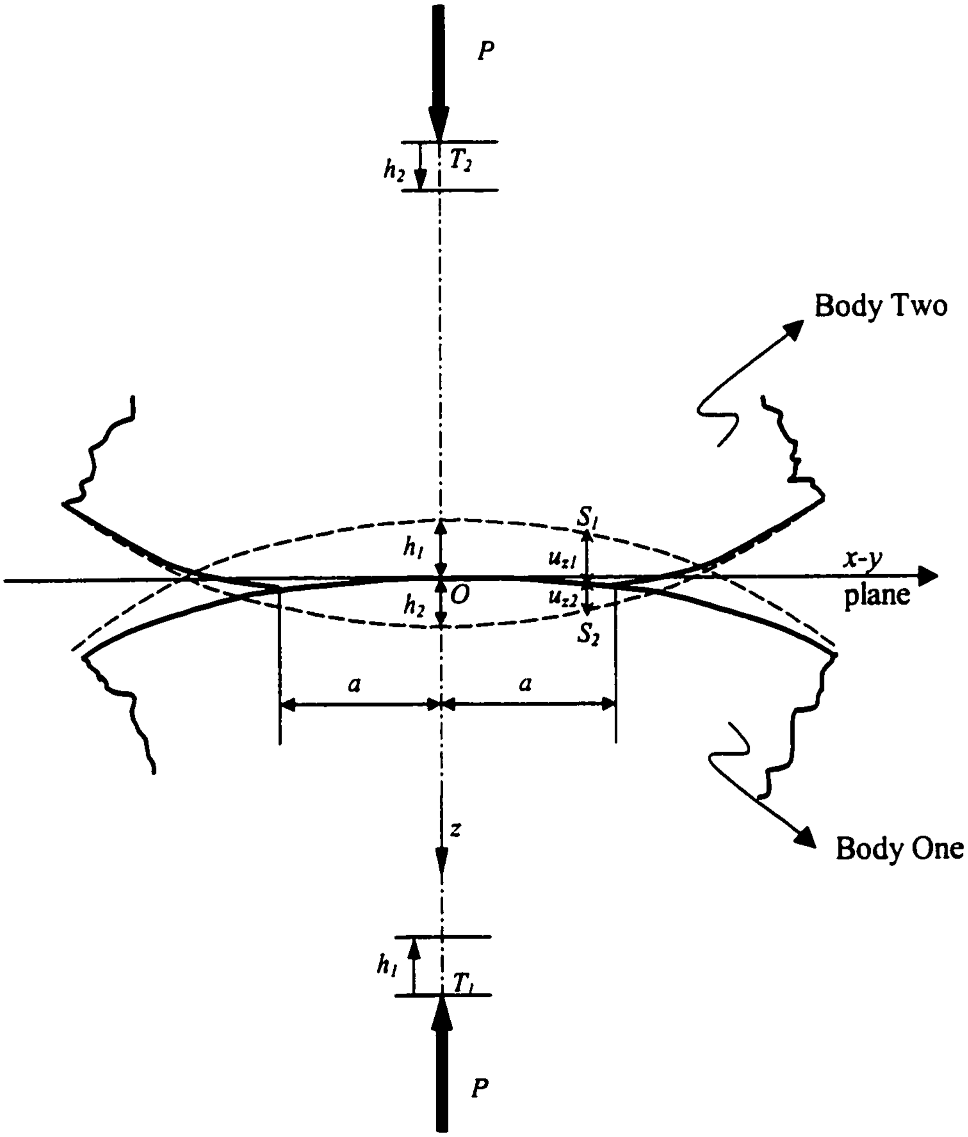

Fig. 4.2: A schematic diagram and the geometry parameters for two solids in contact under a normal load P

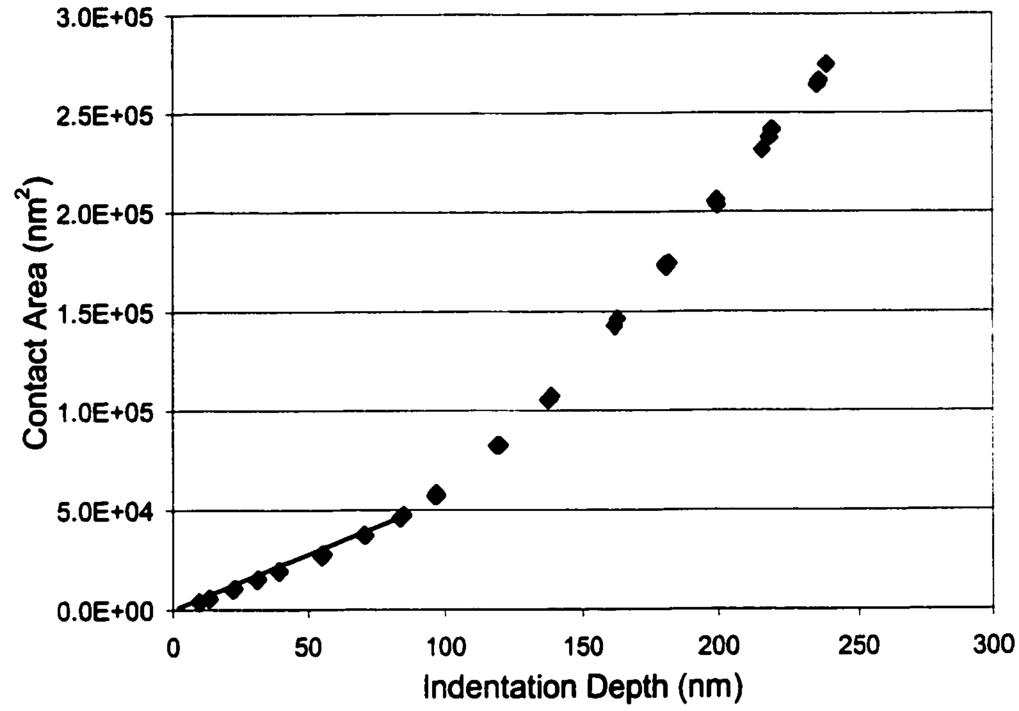

Fig. 4.3: Contact area vs. indentation depth for tip 47 (long range)

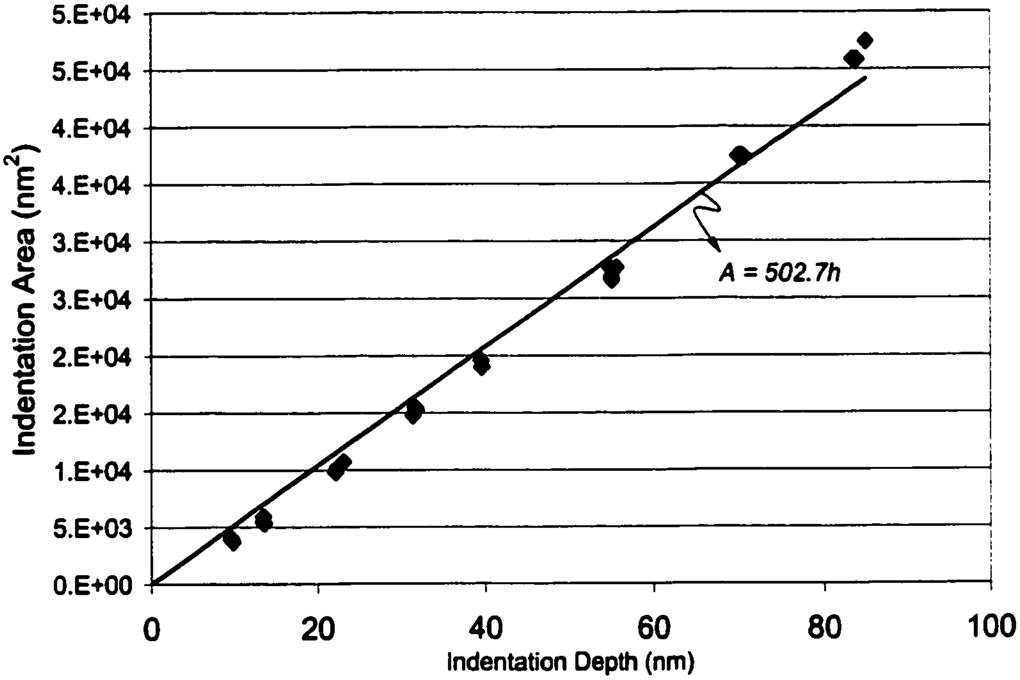

Fig. 4.4: Contact area vs. indentation depth for tip 47 (short range)

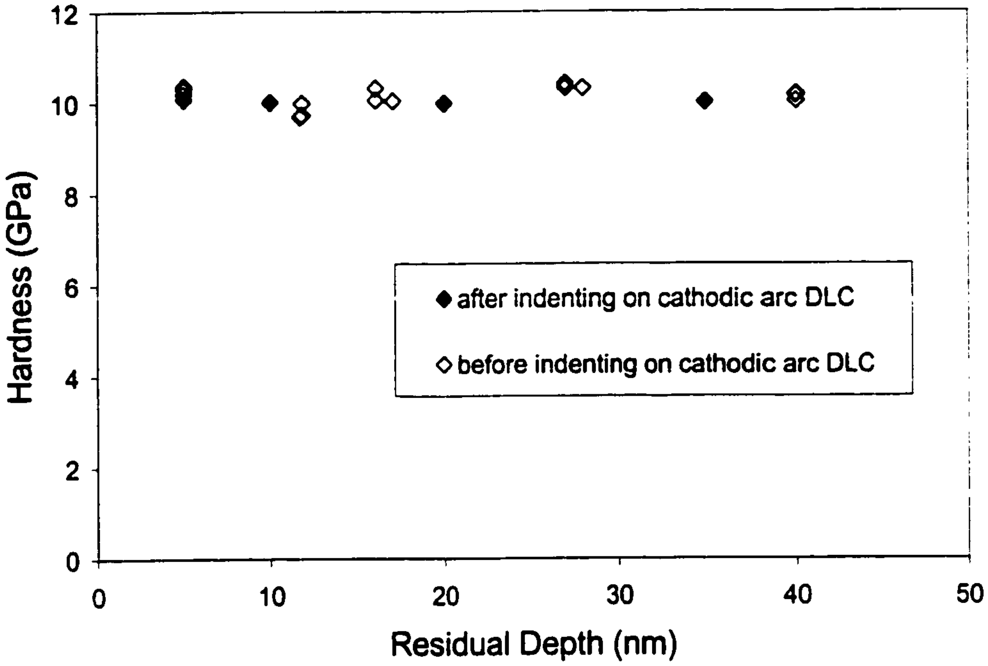

Fig. 4.5: Hardness values calculated by the same tip shape function for tip 47 before and after indenting on a cathodic arc DLC film

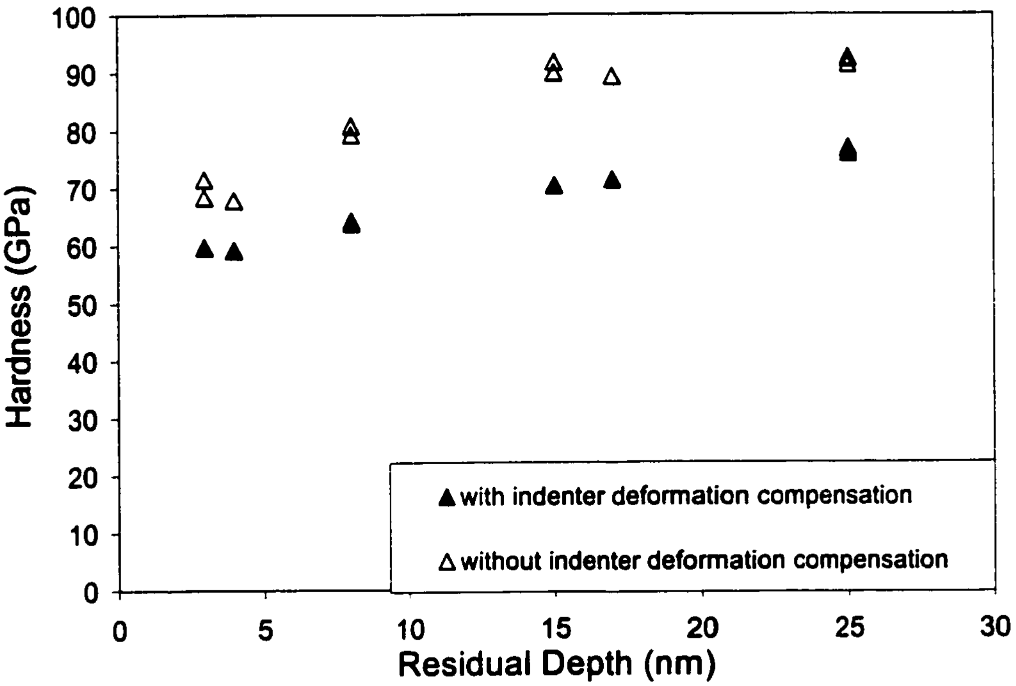

Fig. 4.6: Hardness of the cathodic arc DLC film deposited under –100V substrate bias

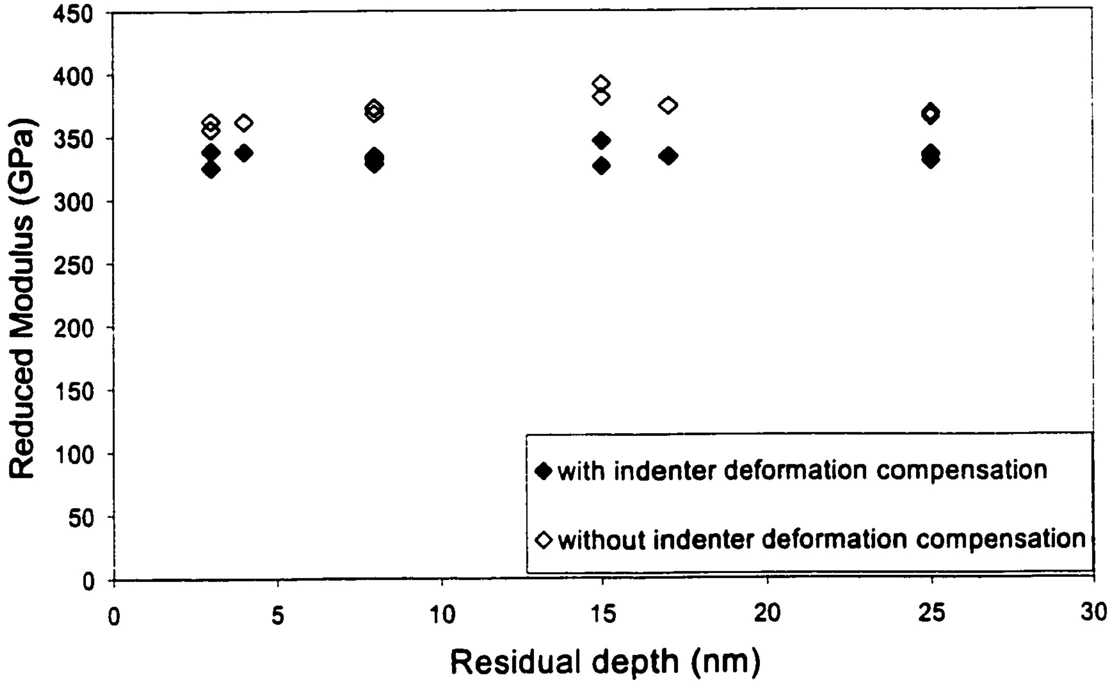

Fig. 4.7: Reduced modulus of the cathodic arc DLC film deposited under –100V substrate bias

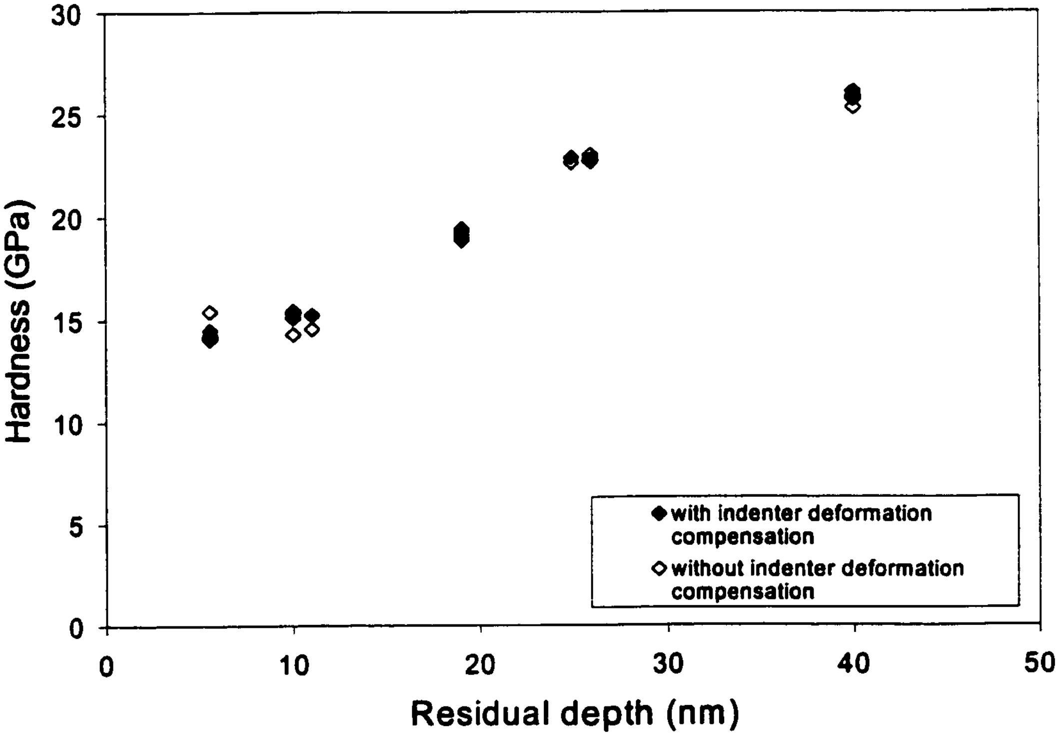

Fig. 4.8: Hardness of the cathodic arc DLC film deposited under –2000V substrate bias

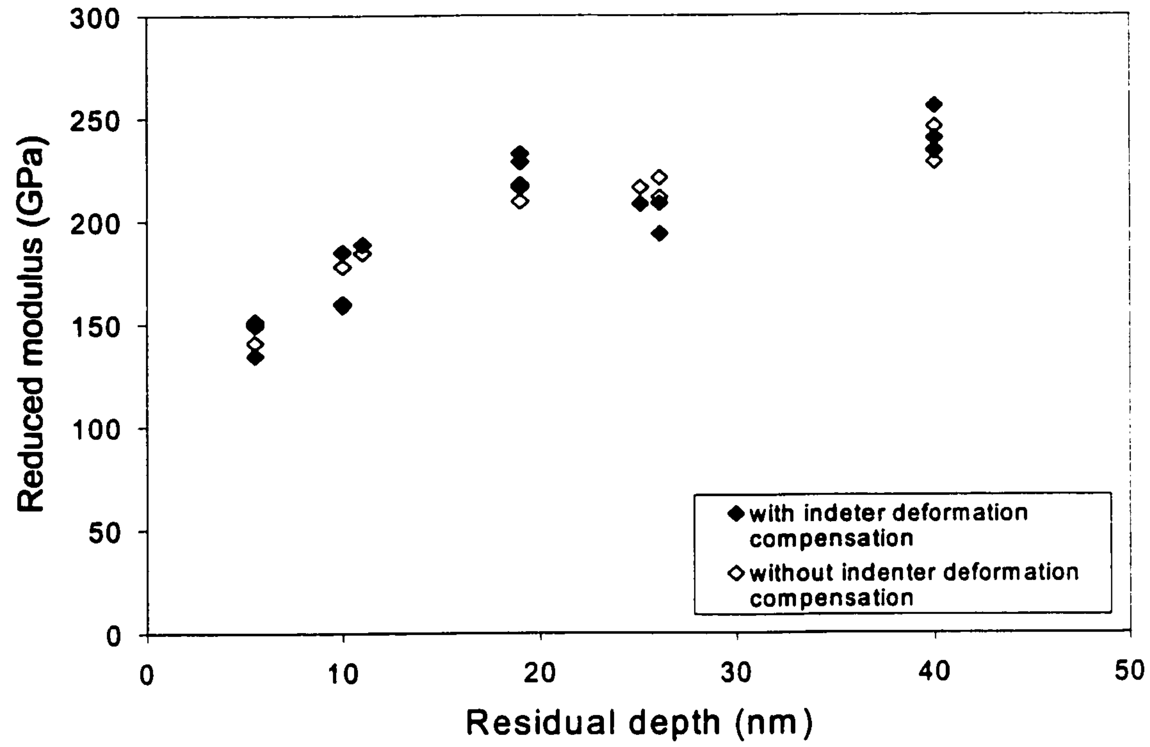

Fig. 4.9: Reduced modulus of the cathodic arc DLC film deposited under –2000V substrate bias

Chapter 5

INDENTATION HYSTERESES AND SUBSTRATE EFFECTS

5.1 INTRODUCTION

Nanoindentation tests have been widely adopted to study the mechanical properties, such as hardness and elastic modulus, of thin film materials. The unloading process of an indentation test is usually assumed to be elastic, and therefore it can be analyzed by the Hertz elastic contact theory (Chapter 4) or by Sneddon's (1965) solution for the elastic field within a homogenous half space indented by a solid of revolution (Chapter 3). However, the purely elastic unloading process can only be observed for a few materials such as fused quartz. The unloading process for most materials usually involves a yielding in tension due to the residual stresses generated in the loading process. If the material is loaded again at the same location with the same maximum force, the second loading process usually contains re-yielding at forces close to the maximum. Again, the second unloading process shows yielding in tension. Therefore, hysteresis loops are generated by the second and subsequent loading cycles. The residual stress generated in each loading process suppresses additional plastic deformation. The hysteresis can be completely suppressed (subjected to shakedown) after a few loading cycles. After shakedown, both the loading and unloading processes are purely elastic.

Indentation hysteresis can also be generated in semiconductor materials such as silicon and germanium. Unlike the hysteresis mentioned above, hysteresis in these materials does not have obvious signs of re-yielding in the reloading process, and thus their deformation mechanisms are different from the one mentioned previously. Silicon experiences phase transformations from the semiconductor state to the denser metal state under load. This transformation is reversible and not suppressible (or subject to shakedown). This means that hysteresis still exists after many cycles of repeated indentation. Using these two types of indentation hysteresis, we can study the substrate effects on the nanoindentation techniques of film/substrate systems. We are particularly interested in the films a few nanometers thick used in the magnetic recording slider-disk interface.

5.2 HYSTERESIS GENERATED BY INDENTATION CYCLES OF LOADING AND UNLOADING

Analyses based on Sneddon's solution (see Chapter 3) or Hertz contact theory (see Chapter 4) are usually applied to the unloading part of the cycle, since the unloading process is assumed to be purely elastic. This means that if a second loading cycle were generated at the same location immediately after the first cycle, the second loading process would follow the first unloading curve, and so would the second unloading curve. This is true for materials such as fused quartz. Figure 5.1 shows the load/displacement curve for fused quartz under double-cycle loading of 100 μN. It is obvious that the first unloading curve, the second loading curve, and the second unloading curve overlap one another. Note that the unloading curves are straight lines with a slightly curved portion for loads lower than 20 μN.

However, the purely elastic unloading assumption is not true for most materials. Repeated indentation at the same location usually generates hysteresis loops. Figures 5.2(a), 5.2(b), 5.2(c), and 5.2(d) show a doubled-cycled loading function and the load/displacement curves of double-cycled loading for steel, nickel phosphorus (NiP) and silicon <100>, respectively. For all of the cases shown, it is clear that the second loading curves do not coincide with the first unloading curves. The second cycles form closed loops. However, the graph shapes of the hysteresis of steel and NiP are very different from that of silicon. The silicon hysteresis graph is formed by two relatively smooth curves, while the curves of steel and NiP have kinks. This suggests that the deformation mechanism of silicon under repeated indentation is different from that of steel or NiP. Both deformation mechanisms are discussed in detail in the next subsections.

5.2.1 Hysteresis formed by elastic-plastic deformation

Consider the graphs for steel and NiP in Figs 5.2(b) and 5.2(c). There are kinks on the first unloading, the second loading, and the second unloading curves. The kinks on the unloading curves appear at very low loads while the kinks of the second loading curve are close to the maximum load (displacement). The kinks represent a sudden softening mechanism in the materials. Therefore, the kinks are signs of a transition from elastic processes to plastic processes, i.e. the onset of plastic deformation. Moreover, the kinks on the unloading curves represent a yielding in tension while the kink on the reloading curve indicates a yielding in compression. These observations agree with the prediction by Johnson (1985) and the finite element simulation of repeated indentation of a half-space by a rigid sphere reported by Kral et al. (1993). In their analysis, Kral *et al* mentioned that yielding during unloading is caused by a continuous increase in both the tensile hoop and the compressive radial stresses upon the removal of the approximately uniform contact pressure. Thus, the kinks on the unloading curves occur when the loads are vanishing, since larger differences between the tensile hoop stresses and the compressive radial stresses are created. They also indicated that yielding during unloading occurs on the material surface just outside the maximum contact area and is less likely to be observed on materials with larger elastic modulii and smaller strain hardening exponents. This also agrees with the experimental findings here, since the modulus of NiP is about 150 GPa and is larger than the fused quartz modulus of 70 GPa. We do not see any kinks from the unloading curves of fused quartz. Kral *et al* also reported that re-yielding in tension occurs during the second loading process. However, they did not mention the timing of this re-yielding.

Figure 5.3 shows the load/displacement curve for five load-unload cycles of NiP at the same location. The curves are marked according to the order in which they are generated. Again, the second loading cycle generates a hysteresis loop, in which neither the loading nor the unloading curve coincides with those of the first loading cycle. However, the third through fifth loading cycles do not form hysteresis loops. In fact, the loading and unloading curves of the third through fifth cycles essentially overlap the second unloading curve. There are kinks in the loading and unloading curves at relatively low loads. The kinks appearing at high load in the second loading curve do not occur in the third through fifth loading curves. This result implies that the plastic deformation due to compression is suppressed or subjected to shakedown. Johnson indicates that residual stresses introduced in the early loading cycles are "protective in the sense that they make yielding less likely" on the later loading cycles. Thus, after a few cycles of loading, the hysteresis, which is due to re-yielding, should vanish.

Figure 5.4 shows the load/displacement curve for steel undergoing five cycles of indentation at the same location. These curves are slightly different from those for NiP, because the hysteresis of steel is not subjected to shakedown within the first three cycles; it takes an additional loading cycle. Based on the finite element analysis by Kral et al., the difference in behavior between steel and NiP may be attributed to the larger elastic modulus or the smaller strain hardening exponent of steel.

The observation of plastic deformation contradicts the assumption of the purely elastic unloading processes when applying elastic theories to hardness measurements. However, since the elastic theories are applied at the maximum load point on the first unloading curve and the onset of plastic deformation appears later at a very low load, the elastic theories can still be applied.

5.2.2 Hysteresis formed by phase transformations

As seen in Fig. 5.2, the shape of the hysteresis loop for silicon is very different from those for steel and NiP. There is no kink on the second loading curve, and the second unloading curve almost overlaps the first unloading curve. To further confirm the shape of the hysteresis we used different loads to generate indentation hystereses. Figures 5.5(a) and 5.5(b) show the load/displacement curve for silicon for two cycles of indentations at 500 μN and 250 μN, respectively. Figure 5.5(c) shows the normalized plot for both indentations. The hysteresis loops are self-similar according to the normalized plot. There is no observable onset of plastic deformation on the loading curves. Furthermore, there is no sign of yielding in tension while withdrawing the indenter. Therefore, the special shapes of the hysteresis loops for silicon are not due to special loads or stresses. Figure 5.6 shows the load/displacement curve for silicon under ten cycles of repeated indentations at the same location. Surprisingly, the hysteresis loop generated in each cycle overlaps the others, and the process shows no sign of shakedown. This means that the shape and size of the hysteresis after ten cycles of repeated indentations remains the same as that of the first cycle. This phenomenon suggests that the deformation mechanism of silicon under repeated indentations is different from that of steel and NiP, which involves elastic-plastic deformation as mentioned in the previous subsection.

To further compare the deformation mechanism behind the indentation hysteresis loops of silicon and NiP we performed two-stage loadings on them. Figure 5.7 shows a two-stage loading function versus time. This function loads the specimens with a smaller load (100 μN in this case) for five cycles and then with a larger load (400 μN in this case) for another five cycles at the same location. In the study, the second-stage load is held fixed while the first-stage load varies. The purpose is to investigate the difference in the second-stage hysteresis due to different first-stage loads. Figure 5.8 shows the responses of NiP due to two two-stage loading functions. In this experiment the first-stage loads are 100 μN and 200 μN, whereas the second-stage loads are fixed at 400 μN. It is clear that hysteresis loops were generated in the first and second-stages for both loading functions. However, the sizes of the second stage hystereses are significantly different for the different first-stage loads. The second hysteresis associated with the larger first-stage load is smaller than that of the smaller first-stage load. A reasonable explanation of this phenomenon is that more material was deformed and shaken down in the first load stage for larger first-stage loads. Since plastic deformation is not a reversible process, the material left for plastic deformation for the second-stage load is less for larger first-stage loads. Therefore, the second-stage hysteresis loops are smaller for larger first loads. Note that both of the hystereses exhibited shakedown after ten cycles of repeated indentations. Figure 5.9 shows the responses of silicon due to three two-stage loading functions with first-stage loads of 100 μN, 200 μN, and 300 μN, and with second-stage loads fixed at 400 μN. Hystereses are generated in all of the cases in the first and second loading stages. However, unlike the situation for NiP, the sizes and shapes of the second-stage hystereses were not affected by the magnitudes of the first-stage loads. This interesting phenomenon again confirms the view that the deformation mechanism of silicon is reversible and is very different from that of NiP.

Gerk and Tabor (1978) reported that silicon and germanium undergo pressure-induced phase transitions from their semiconductor structures to metals. They reported that the transition hydrostatic pressures of silicon and germanium are 19 GPa and 12 GPa, respectively, which are about 50% greater than the reported hardnesses (12 GPa for Si and 8 GPa for Ga). Clarke et al. (1988) studied the transition of silicon and germanium by measuring their electrical conductivity changes under Vickers and Knoop indentations. They found that the materials become electrically conducting instantaneously as the load is applied. They also reported that "the process is reversible on subsequent unloading and reloading". Hu et al. (1986) reported that the volume change associated with the transformation process is 21%. Pharr et al. (1989) studied repeated indentations on fused quartz and silicon. They made four cycles of indentations with loads between 0.5 mN and 120 mN in each test. They reported a purely elastic unloading process for fused quartz, but concluded incorrectly that "it is typical of most metals, ceramics, and glasses", which is contrary to our findings. Hysteresis generated on silicon was reported and attributed to "one intriguing mechanism ...which is a sluggish, but reversible, pressure-induced phase transformation beneath the indenter". From their cross-section study of silicon <100> under indentation, Wu et al. (1999) also observed the amorphous phase beneath the indenter. Figure

5.10 shows the phase diagram for silicon (1991). According to the diagram, the pressure required for silicon to transform from a face-centered cubic structure to a centered tetragonal structure is 12 GPa at room temperature (300 K). The stresses generated under the indenter can be roughly estimated as the load divided by the square of the tip radii. For the case of tip 18, which has a tip radius of 50 nm, 25 μN generates 100 GPa. This stress is more than sufficient to induce phase transformation.

Repeated indentation tests were performed on amorphous silicon (a-Si) to further verify the above observations. Figure 5.11 shows the load/displacement curve for a-Si under five cycles of repeated indentation. It is obvious that the amount of hysteresis of a-Si is significantly smaller than that of crystalline silicon. Like those of NiP and steel, the hysteresis exhibits shakedown after five loading cycles, although the kink of re-yielding on the second loading curve is not easily observable. This test suggests that amorphous silicon undergoes elastic-plastic deformation, rather than phase transformation, under the application of repeated indentations. Since application of pressure generates a phase transformation from less dense states to denser states, and amorphous silicon is the densest state of silicon, it is understandable that hysteresis due to phase transformation cannot be observed for amorphous silicon.

Since the hysteresis found in silicon and germanium is due to the pressure-induced phase transformation, it is not possible to either subject the hysteresis to shakedown or to find an unloading process that is elastic or whose top portion is elastic. The true hardnesses and modulii of these materials cannot be assessed by the elastic theories. However, the approximate values can still be estimated with the available elastic theories.

5.3 SUBSTRATE EFFECTS IN THIN FILM MATERIALS

Substrate effects in characterizing the mechanical properties of thin films have been investigated for many years. As the demand for thinner protective films increases in order to decrease the gaps between the sliders and disks in hard disk drives, characterizing the true mechanical properties of the films becomes an even more difficult challenge. It is unlikely that we can avoid the influence of substrates in attempts to obtain the film properties by means of indentation tests for films with thicknesses of 2 to 5 nm. It is widely believed that as the indention depth decreases the substrate effects will become smaller. However, a limit of this concept certainly exists as the film thickness approaches zero. The rule of thumb is that if the residual depths of indentations do not exceed 20% of the film thickness, then the measured properties are expected to be free of substrate effects. Some rules state that the maximum indentation depth should not exceed 20% of the film thickness to avoid substrate effects. There is essentially no rule that is universally agreed upon. However, all of these rules depend only on the percentage of film thickness that the indenter penetrates and thus, are material-independent.

Since there are two types of indentation hysteresis, i.e. shakedownable and non-shakedownable, the substrate effects of thin-film materials can be studied if the film hysteresis is shakedownable and the substrate hysteresis is not (or vice versa). Tests can be conducted with various loading forces for five to ten cycles of repeated indentations to shakedown the hysteresis of the film. The remaining hysteresis is due only to the substrate. The substrate effects can be quantified by the hysteresis energy (The area enclosed by the loading and unloading curve) remaining after the loading cycles. A remaining hysteresis energy of zero means there was no influence by the substrate on the indentation processes. Therefore, true film properties can be obtained for an indentation exhibiting zero remaining hysteresis energy.

In our study a 100 nm permalloy (NiFe) film deposited on a silicon wafer (si <100>) was investigated. The permalloy layer consisted of 80% nickel (Ni) and 20% iron (Fe). Three cube-corner tips (90° apex angle), tip18, tip47, and tip20 with radii of 50, 160, and 334 nm, respectively, were used to generate indentation hysteresis curves. The tip radii were calculated by the method presented in Chapter 4. Indentation forces were adjusted to keep the maximum depths between 3 and 120 nm to obtain a complete understanding across the entire film thickness. Since the tip radii are different for the different tips, the indentation forces needed to generate the same depths are expected to be different.

Figure 5.12 shows a typical load/unload curve and the final hysteresis loop of the permalloy/silicon system after five loading cycles with tip 18 (50 nm radius). The maximum depth and residual depths are 54 and 45 nm, respectively. It is obvious that the size of the hysteresis loop decreases with an increase in the number of loading cycles, and becomes saturated in the third cycle. The remaining hysteresis is contributed by the silicon substrate. Figure 5.13 shows the hysteresis energy versus maximum indentation forces for all three tips. The hysteresis energies were calculated by integrating the final hysteresis loops over the enclosed areas. As expected, the maximum force required to generate the same amount of hysteresis energy is smaller for a sharper tip. Moreover, the critical forces, i.e. the largest forces allowed to generate zero hysteresis energy, for tip18, tip47, and tip20 are 40 μN, 150 μN, and 400 μN, respectively. Figure 5.14 shows the hysteresis energy verse maximum indentation depth for the three tips. The critical maximum depths (i.e. the largest maximum depths with zero hysteresis energy) for the three tips are 25 nm, 27 nm, and 33 nm, in order of tip radius. This indicates that the indenters did not experience the substrate effects if the maximum depths were lower than 25 nm, and 27 nm or 33 nm, depending on the tip radius. Figure 5.15 shows the hysteresis energies versus the residual depths for all three tips. In contrast to the indentation forces and maximum depths, the critical residual depths—which are the largest residual depths with zero hysteresis energies—for all of the tips are 19 nm, which is 19% of the film thickness. This indicates that if the residual depths are smaller than 20% of the film thickness, measurements using the nanoindentation techniques will exhibit no substrate effects.

5.4 SUMMARY AND CONCLUSIONS

Hystereses were generated by repeated indentations at the same location on the surfaces of several materials. Yielding in tension and re-yielding were observed in metals such as NiP and steel. This type of hysteresis exhibits shakedown after a few cycles of repeated loading and unloading. The loading processes after shakedown are purely elastic. Phase transformation occurred with repeated indentations on semiconductors such as silicon. Silicon transforms from its semiconductor state to a denser metal state. The transformation was reversed when the load was withdrawn. Therefore, the transformation is reversible and is not suppressed (or does not exhibit shakedown) after multiple loading cycles.

Substrate effects were studied on a 100 nm permalloy film on a silicon substrate. Three indenters with different radii were used to study the influence of tip radius on substrate effects. The study shows that, for the indentation residual depths smaller than 20% of the film thickness, substrate effects can be ignored. This statement is true for all the tips tested regardless of tip radii.

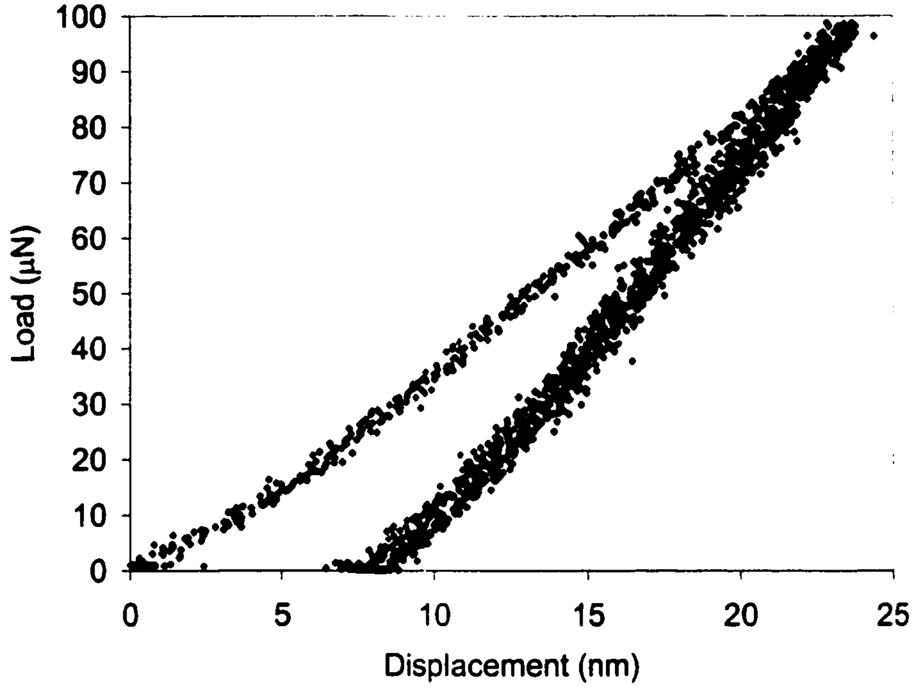

Fig. 5.1: Two cycles of repeated indentations on fused quartz. The loading and unloading curves of the second loading cycle overlap the first unloading curve.

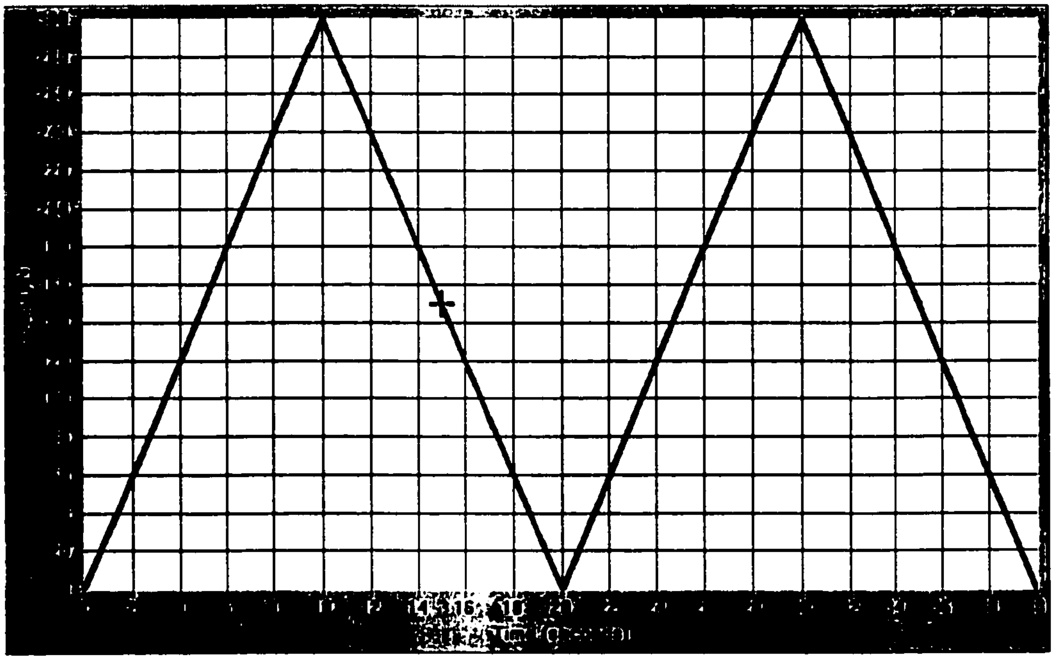

Fig. 5.2(a): A double-cycle loading function with maximum force of 300 μN

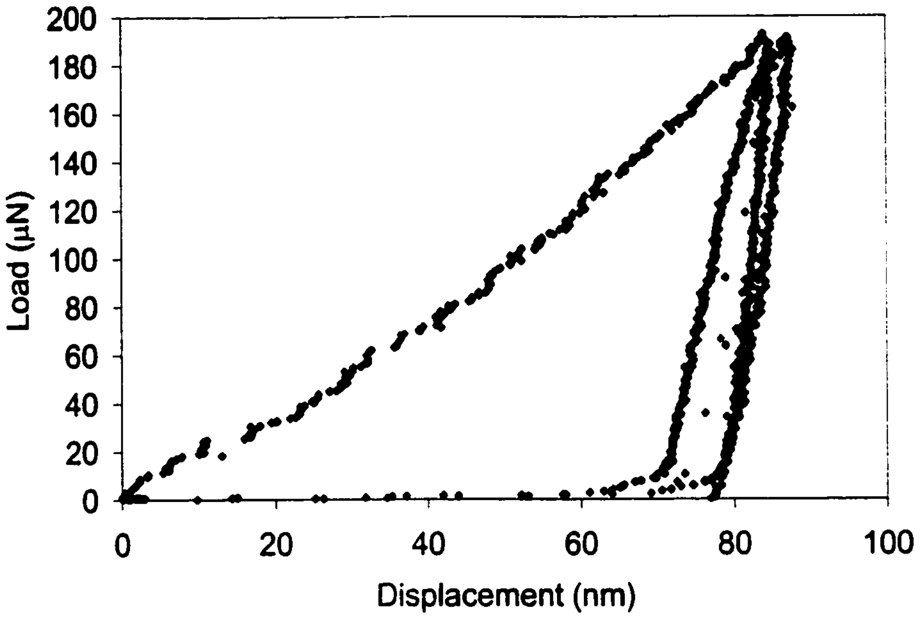

Fig. 5.2(b): The load/displacement curve of steel under a repeated loading for two cycles. Hysteresis is generated by the second cycle.

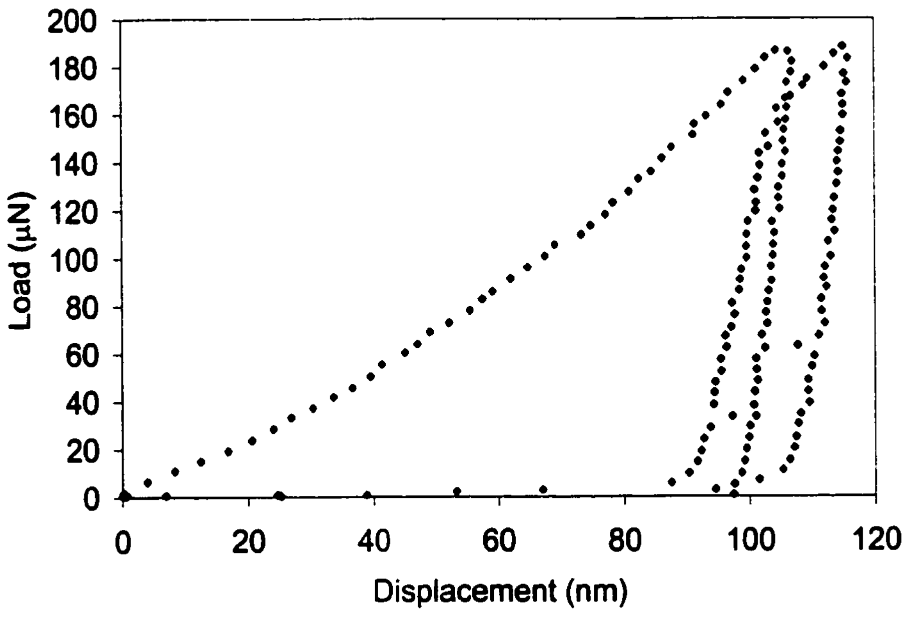

Fig. 5.2(c): The load/displacement curve of Nickle Phosphorus (NiP) under repeated indentations for two cycles. Clear signs of yielding while withdrawing and re-yielding at second loading.

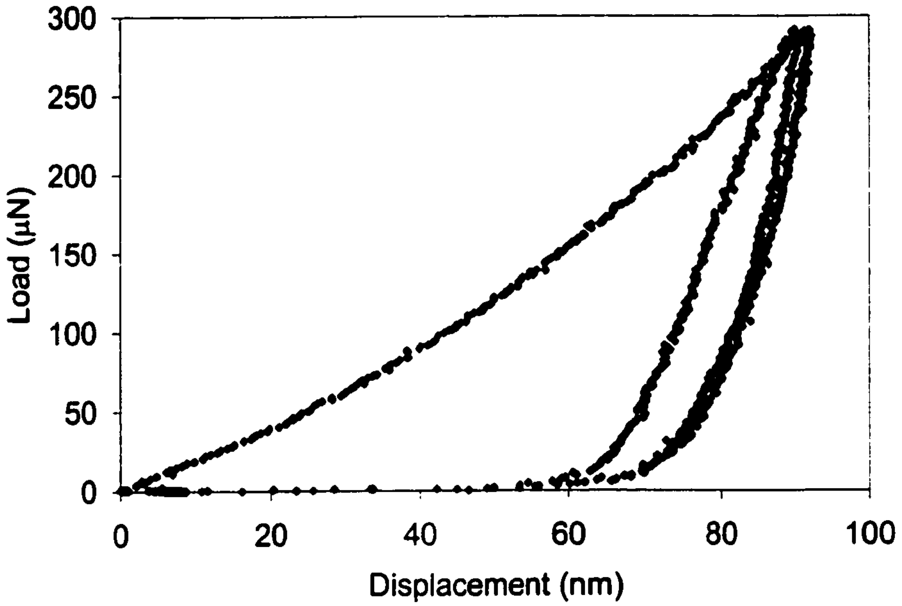

Fig. 5.2(d): The load/displacement curves of silicon <100> under a repeated indentations for two cycles with maximum forces of 300 μN. Hysteresis is generated in the second cycle. However, there is no signs of re-yielding in the curves.

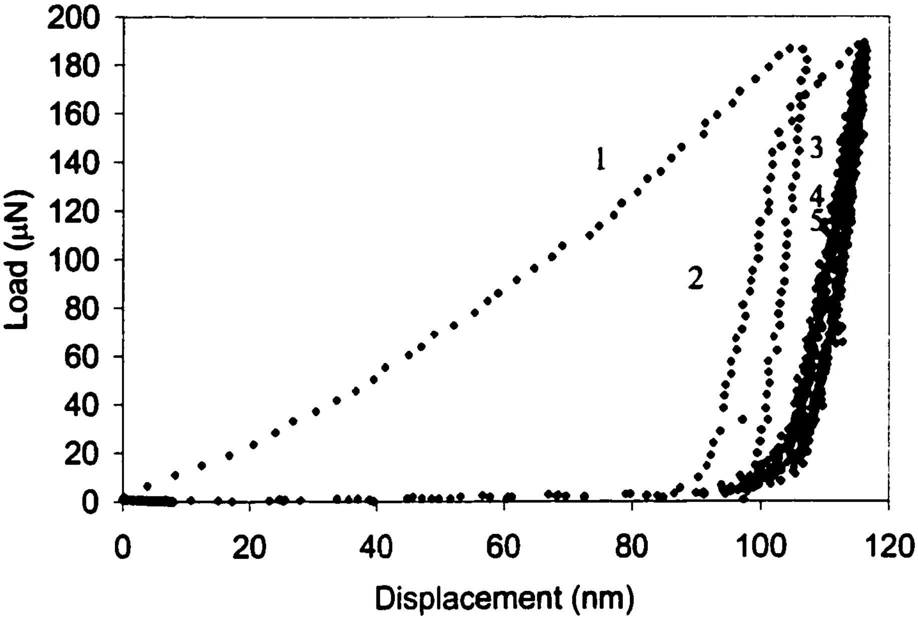

Fig. 5.3: The load/displacement of NiP with five cycles of repeated indentations. The hysteresis generated in the second cycle is subjected to shakedown after the third cycle.

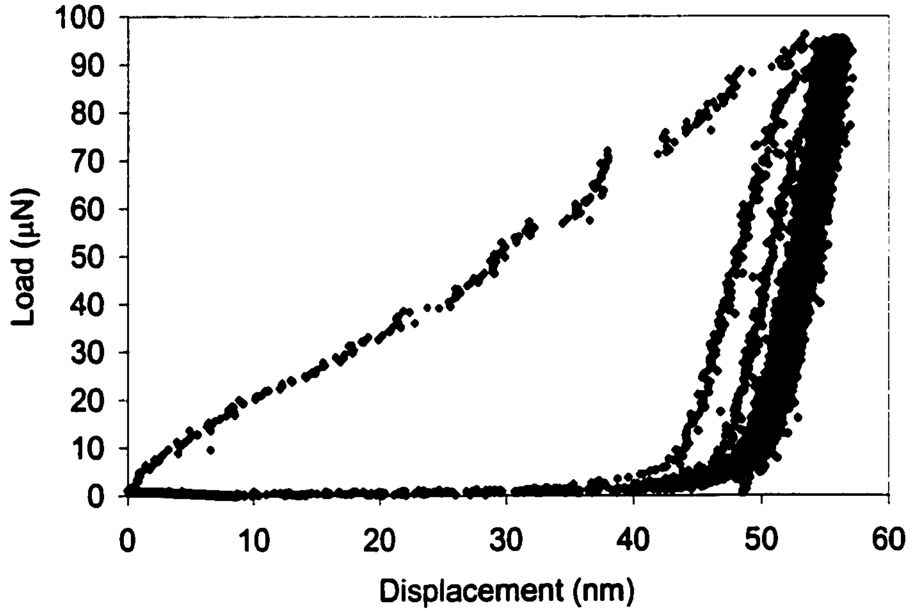

Fig. 5.4: The load/displacement of steel with five cycles of repeated indentations. The hysteresis generated in the second and third cycles are subjected to shakedown after the fourth cycle.

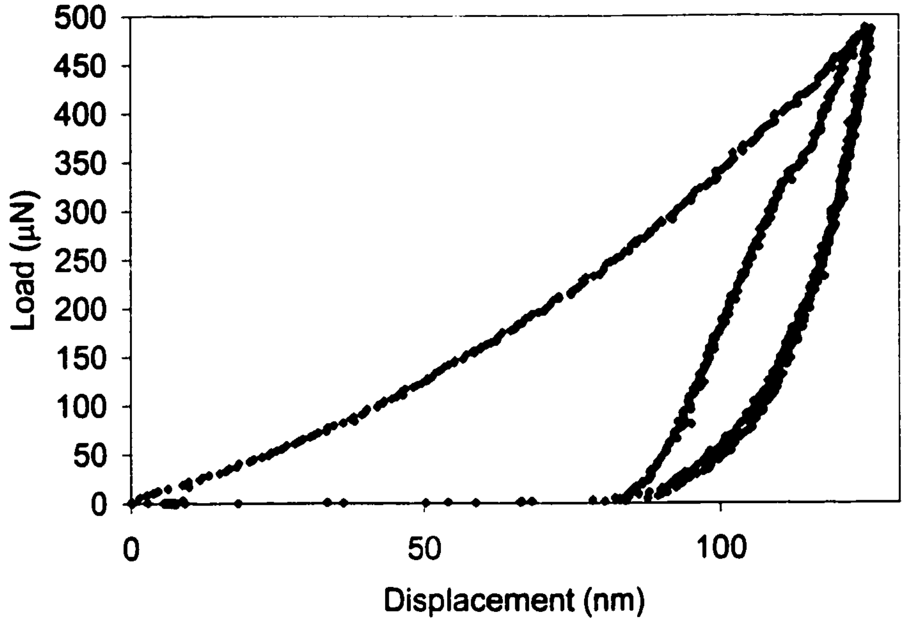

Fig. 5.5(a): the load/displacement curve of silicon <100> under two cycles of repeated indentations with maximum force of 500 μN.

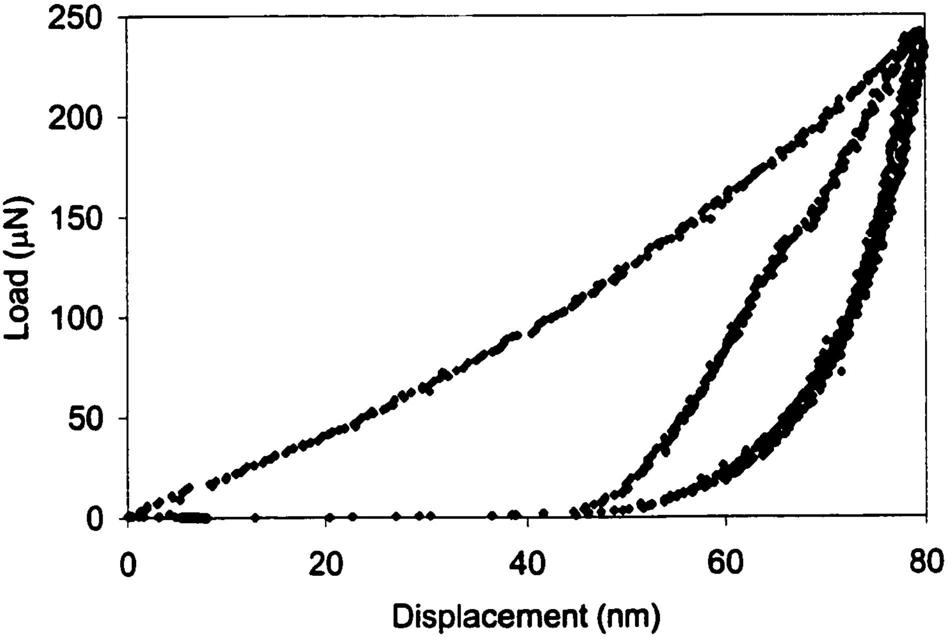

Fig. 5.5(b): the load/displacement curve of silicon <100> under two cycles of repeated indentations with maximum force of 250 μN.

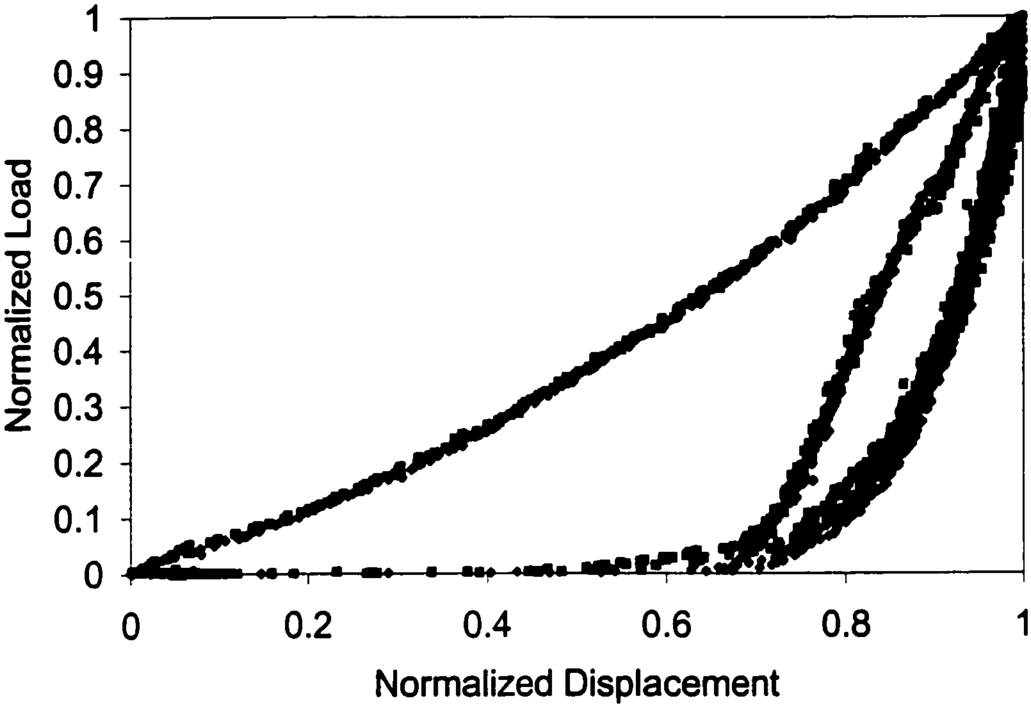

Fig. 5.5(c): The normalized load/displacement curves of Fig. 6(a) and Fig. 6(b). This figure shows that the curves of silicon are self-similar.

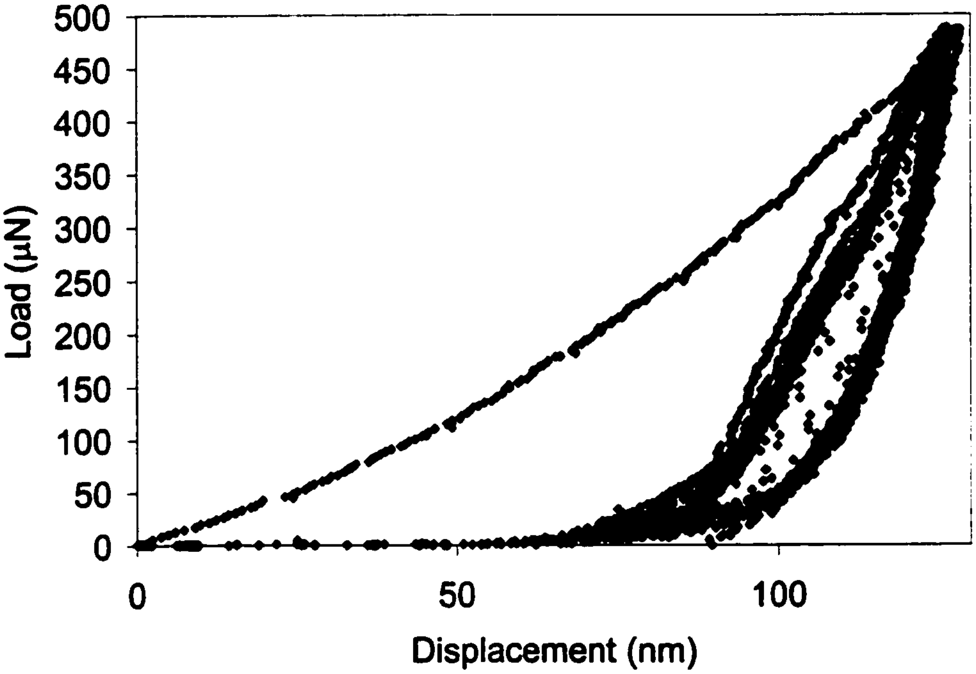

Fig. 5.6: The load/displacement curve of silicon under ten cycles of repeated indentations at the same location.

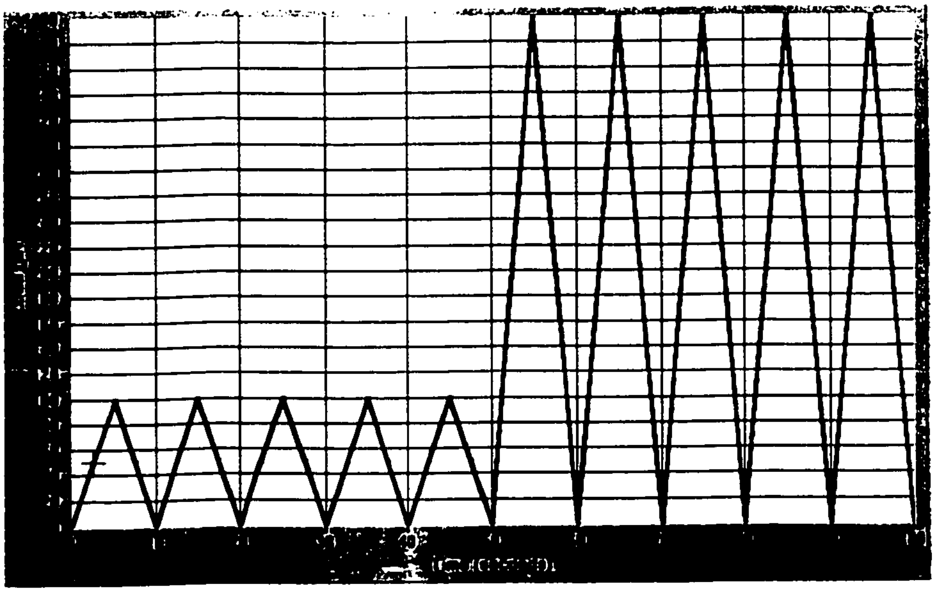

Fig. 5.7: A two-stage loading function

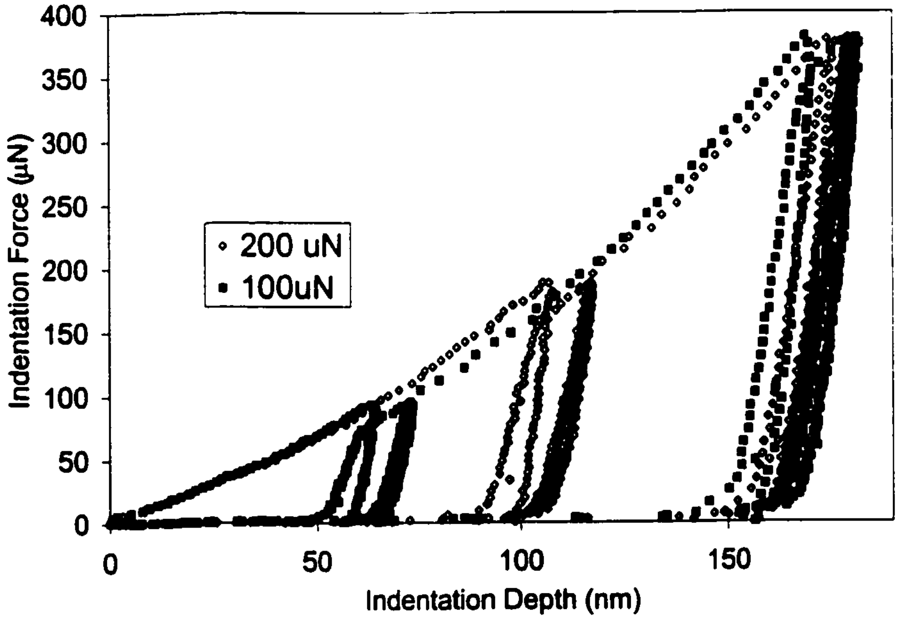

Fig. 5.8: Two-stage loadings on NiP with first loadings of 100 μN and 200 μN. The second loadings remain the same.

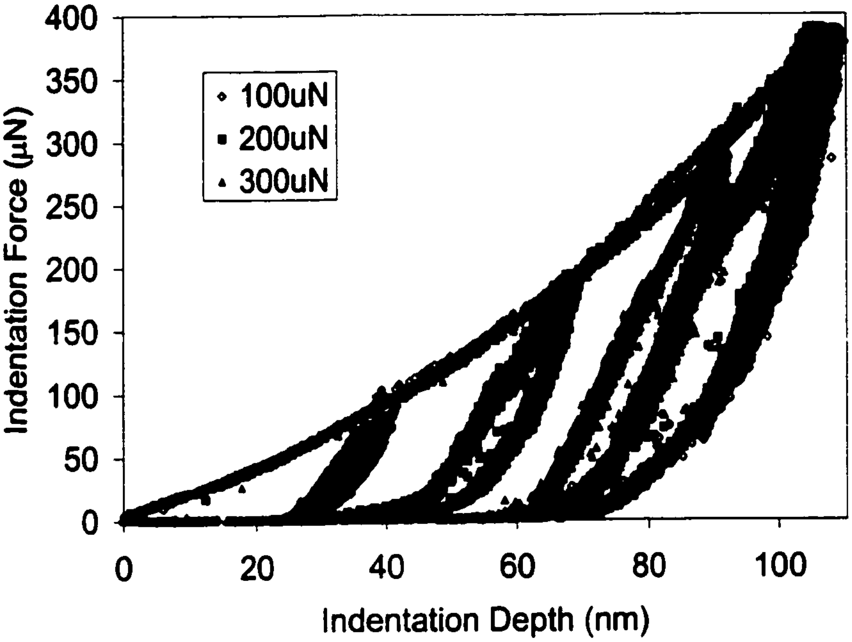

Fig. 5.9: Three two-stage loadings on silicon with first loadings of 100 μN, 200 μN, and 300 μN. The second loadings remain the same.

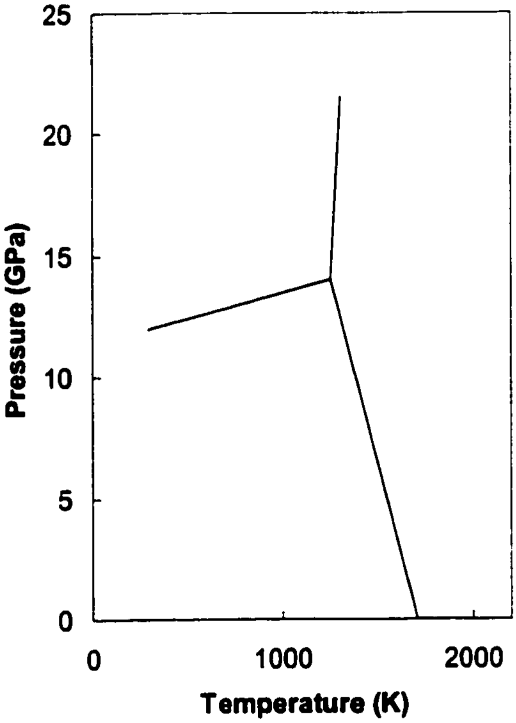

Fig. 5.10: Phase diagram of silicon. The phase transformation pressure at room temperature (300 K) is about 12 GPa. Graph reproduced from Phase Diagrams of the Elements[9]

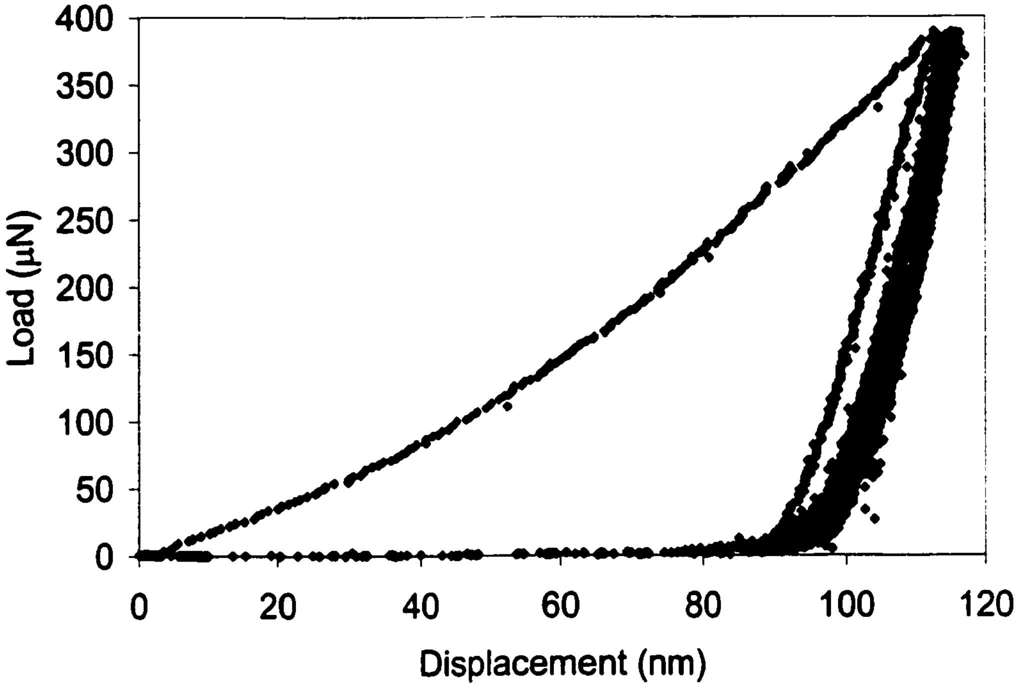

Fig. 5.11: The load/displacement curve of amorphous Si under five cycles of repeated indentations. The hysteresis has been subjected to shakedown shakedowned. Amorphous silicon sample provided by IBM.

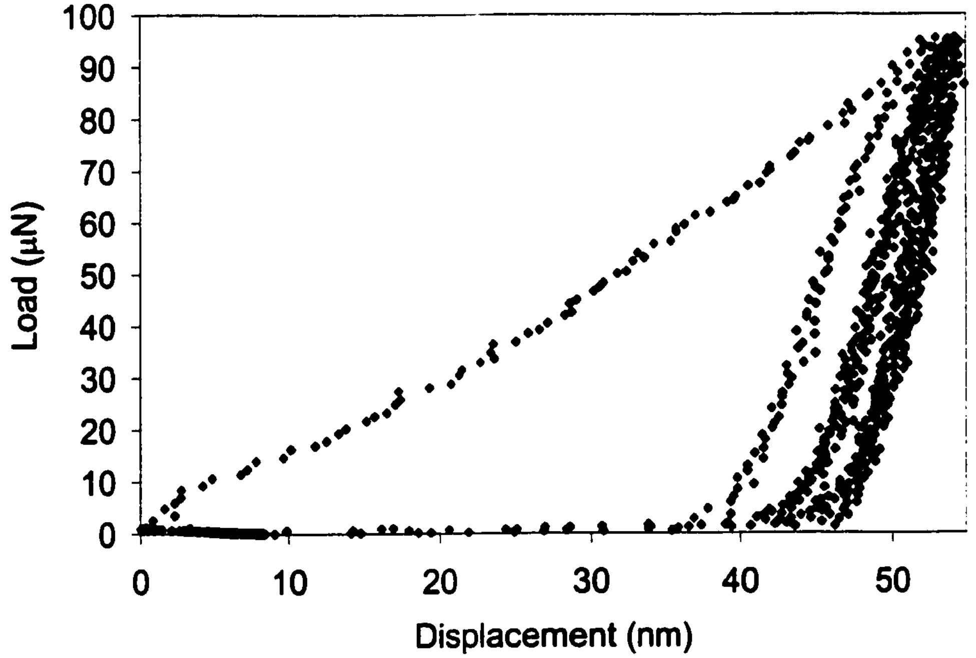

Fig. 5.12: A typical load/unload curve and the final hysteresis loop of the permalloy/silicon system after five loading cycles with tip 18 (50 nm in radius)

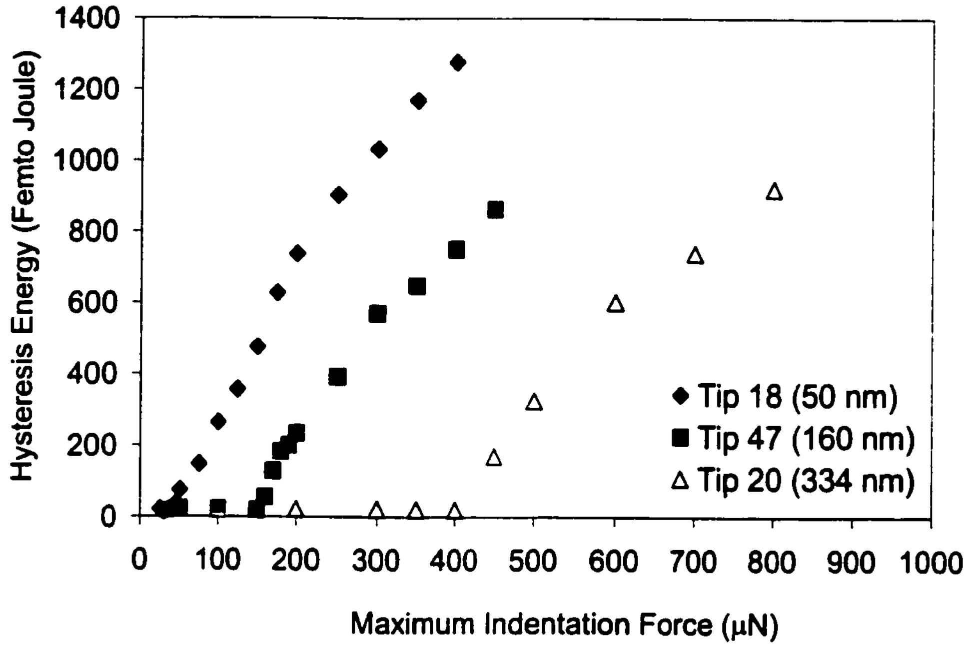

Fig. 5.13: Hysteresis energy versus maximum indentation forces for three tips with variuos tip radii. The hysteresis energies were calculated by integrating the final hysteresis loops over the enclosed areas. The critical maximum indentation forces for the three tips are 40 μN, 150 μN, and 400 μN, respectively.

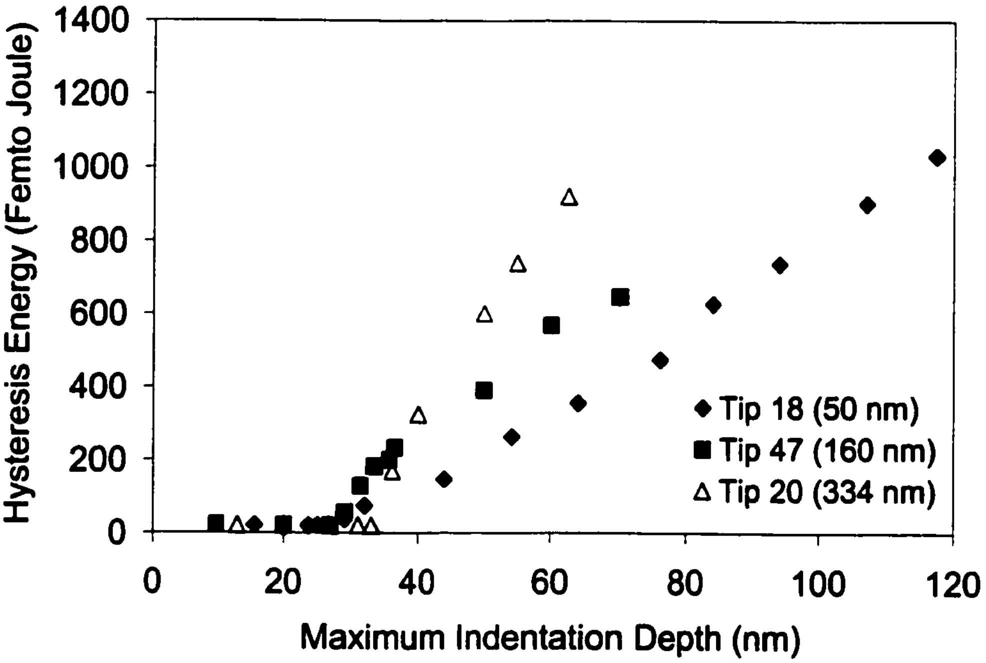

Fig. 5.14: The hysteresis energy versus maximum indentation depths for the three tips. The critical maximum depths for the three tips are 25 nm, 27 nm, and 33 nm, respectively.

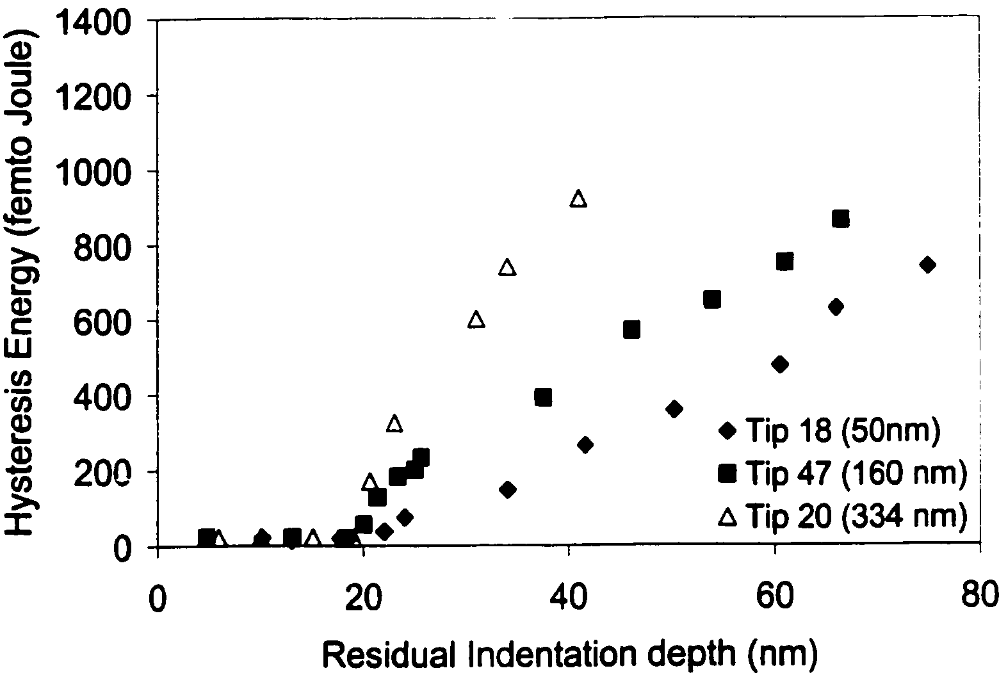

Fig. 5.15: The hysteresis energies versus the residual depths for all three tips. In contract to the maximum indentation forces and maximum depths, the critical residual depths are 19 nm for all of the tips.

Chapter 6

A STUDY OF GEOMETRY AND ROUGHNESS EFFECTS ON NANOINDENTATION HARDNESS TESTS

6.1 INTRODUCTION

Nanoindentation techniques together with the theoretical analyses in Chapter 3 and Chapter 4 are used to evaluate the mechanical properties of thin film materials. The theoretical analyses in both chapters assume that the surface of the specimen is mathematically smooth and flat. However, real surfaces always have surface curvature and roughness. Calculations based on these models give accurate results when the specimen surface is atomically smooth (e.g. a silicon wafer), or the indentations are much larger or smaller than the size of the surface roughness, in which case the indenter contacts many asperities while pushing into the surface. The contact areas at maximum depths are much larger than the diameters of single asperities. In this case, surface roughness only creates a minor variation of the measurements. In fact, Tabor (1951) noted that the surface asperities could be taken into consideration by adding a constant term to the displacement of the indenter. When the indentation depths are much smaller than the heights of the roughness, the indenter may only contact with one asperity. If the asperity is much larger than the indentation in both height and diameter, the flat and smooth surface assumptions may still be valid. Questions arise if the indentation size is comparable to that of the surface roughness. In preparation for the expected future areal density on magnetic disks, thin film overcoats with thicknesses of 2 to 5 nm are already under developement. The typical size of the roughness of these films is around 0.6 nm in R_a (which will be defined later). To avoid the substrate effect, residual indentation depths have to be smaller than 0.4 to 1 nm. Therefore, indentation sizes similar to that of the surface roughness seem to be inevitable.

The study of contacts between rough surfaces can be traced back to Greenwood and Williamson (1966). They considered the contact of a flat two-dimensional plane with a nominally flat rough surface. They assumed spherical asperities and a Gaussian distribution of asperity heights. They were able to obtain the real total contact area and total contact force by applying the Hertz contact theory to every asperity. Greenwood and Tripp (1967) adopted a similar concept to study the contacts between curved rough surfaces. Their methods are good for large indenters contacting relatively small asperities. More insight is needed in studying single asperity contacts. Bobji et al (1996) studied a single asperity contact with an offset from the centerline of the indenter by a simple geometry analysis. They obtained the following relation,

$$\frac{H_{measured}}{H_{true}} = \left(\frac{R}{R_0}\right)\cos^2\theta. \tag{6.1}$$

The measured surface hardness is related to the true hardness through the geometry factors, which will be defined later. However, their derivation is lacking in terms of mechanics. In this chapter, the above relation is re-derived using the mechanics of Hertz contact theory and it is shown that the quantity in the parenthesis should have a power of 2/3, instead of one. Experimental verification is also provided.

Next, the single asperity contact model is used to study the variation in hardness measurements on rough surfaces. The goal is to relate the variation of hardness measurements to the standard deviation of the roughness properties, such as the quantity in the parenthesis in Eq. (6.1). The concepts of apparent roughness and apparent radius of curvature of the specimen to the indenter are proposed. Experimental results show that the hardness variation increases as the indentation sizes decreases and thus, approaches the surface roughness dimension. At extremely shallow indentations, the ratio of standard deviation of the hardness measurements over the mean hardness on one surface equals the apparent standard deviation of $\left(\frac{R}{R_0}\right)^{\frac{2}{3}}$ for that surface. In addition, it is shown that a blunter indenter experiences less "roughness effect".

6.2 THEORETICAL DEVELOPMENT

6.2.1 Indentations on bumps which are solids of revolution

Here we first call some results presented in Chapter 4. When two solids are brought into contact, they initially touch at a single point or along a line. As the contact force increases, they deform near their points of first contact. With help from the Hertz contact theory, we were able to show that the separation s between the surfaces of two solids of revolution making contact at their apex points is:

$$s = \frac{r^2}{2R}. \tag{6.2}$$

$$\text{where, } \frac{1}{R} = \frac{1}{R_1} + \frac{1}{R_2} \tag{6.3}$$

R is the relative radius of the system at the point of the contact; R_1 and R_2 are the radii of curvature of body 1 and body 2 at the points of contact, respectively; $r = \sqrt{x^2 + y^2}$ is the radial coordinate. Figure 6.1 shows the geometry of two solids of revolution in contact under the application of a normal load P. Body 1 is taken as the indenter and body 2 is the specimen. u_{z1} and u_{z2} are the displacements of points S_1 on the indenter and S_2 on the specimen due to the contact pressure. h_1 and h_2 are the displacements of distant points in the two bodies T_1 and T_2. a is the radius of the contact circle. After deformation, if the points S_1 and S_2 coincide with each other within the contact surface, then

$$u_{z1} + u_{z2} + s = h_1 + h_2 = h, \tag{6.4}$$

where h is the relative displacement of two distant points T_1 and T_2. Equation (6.4) must be satisfied for all points within the contact circle, i.e. for $0 \le r \le a$, where a is the contact radius, (the radius of the contact circle). Substituting Eq. (6.2) into Eq. (6.4), we obtain

$$u_{z1} + u_{z2} = h - \frac{r^2}{2R}. \tag{6.5}$$

The pressure distribution obtained by Hertz, which results in displacements satisfying Eq. (6.5), is given by

$$p = p_0\left[1-\left(\frac{r}{a}\right)^2\right]^{1/2}, \; r \le a, \tag{6.6}$$

where p_0 is the maximum pressure. The displacement for both solids can be written as,

$$u_{zi} = \frac{1-\nu_i^2}{E_i}\frac{\pi p_0}{4a}\left(2a^2 - r^2\right), \; r \le a. \tag{6.7}$$

where $i = 1, 2$. Therefore, Eq. (6.7) can be written as,

$$h = \frac{\pi p_0}{4aE_r}\left(2a^2 - r^2\right) + \frac{r^2}{2R}, \tag{6.8}$$

where $\frac{1}{E_r} = \frac{1-\nu_1^2}{E_1} + \frac{1-\nu_2^2}{E_2}$, E_r the reduced modulus of the system, and h and a are variables independent of r. Since the left hand side is not a function of r, the right hand side cannot be a function of r. Therefore, the coefficient of r^2 must vanish, and we have

$$\frac{\pi p_o}{4aE_r} = \frac{1}{2R}, \tag{6.9}$$

or,

$$a = \frac{\pi p_0 R}{2E_r}. \tag{6.10}$$

Substituting Eq. (6.10) back into Eq. (6.8), we obtain

$$h = \frac{\pi a p_0}{2E_r} = \frac{a^2}{R}. \tag{6.11}$$

The total load can also be calculated by integrating the pressure over the contact area, i.e., $P = \int p(r) 2\pi r dr = 2/3 p_0 \pi a^2$. Substituting for p_0 by inserting $\frac{3}{2}\frac{P}{\pi a^2}$ into Eq. (6.10) and Eq. (6.11), we have,

$$a = \left(\frac{3PR}{4E_r}\right)^{1/3}, \tag{6.12}$$

$$h = \frac{a^2}{R} = \left(\frac{9P^2}{16RE_r^2}\right)^{1/3}. \tag{6.13}$$

The second equality in Eq. (6.13) can be re-written as,

$$P = \frac{4}{3}E_r\sqrt{Rh^3}. \tag{6.14}$$

Taking the first derivative of P with respect to h, we obtain

$$\frac{dP}{dh} = 2E_r\sqrt{Rh} = 2aE_r = 2\sqrt{\frac{A}{\pi}}E_r, \tag{6.15}$$

in which the first equality of Eq. (6.13) and $A = \pi a^2$ have been invoked.

The restrictions of this derivation are that the contact radius must be much smaller than the tip radius, as well as smaller than the lateral and axial dimensions of the two bodies. That is to say $a << R$, and $a << l$, where l represents the lateral and axial dimensions of the bodies. These restrictions simply mean that the tip radius R can be taken as a constant if the contact radius a is relatively small. Therefore, the indenter can be viewed as a spherical body in the contact area if the contact area is small enough.

6.2.2 Indentations on a bump of solid of revolution with offsets

The theoretical development presented in the previous section is valid for solids of revolution contacting at their apex points. In this section, contacts of slightly offset solids of revolution are studied. At the same time, a comparison between the measured and true hardnesses in the presence of surface curvature is also discussed.

Figure 6.2 shows a schematic diagram for contacts between two solids of revolution with an offset angle θ, which is assumed to be very small so that both of the radii of curvature for the two solids in the contact region are constant. This means that the deformations on both solids are localized in their spherical regions. The load applied by the indenter is P and the vertical displacement is h. However, the normal load and normal displacement relative to the specimen are P_n and h_n, respectively. Assuming no friction between the two solids, the method presented in the previous section can model the contact between them with P_n ($= P\cos\theta$) and h_n ($=h\cos\theta$) substituting P and h in Eqs. (6.12) to (6.15), respectively. Sliding between the solids while the indenter is moving into the surface may violate the condition modeled in the previous section. However, the restriction of very small θ prevents the sliding effect from becoming a major issue. According to the first equality of Eq. (6.13), the contact area is directly proportional to the contact depth. Thus, the normal contact area can be written as

$$A_n = \pi h_n R = (\pi h R)\cos\theta = A\cos\theta \tag{6.16}$$

where A is the contact area without offset and R is the relative radius of curvature of the system.

From Eq. (6.3), the value of R achieves its maximum when R_2 approaches infinity (i.e. a flat specimen surface). We denote the maximum value of R as R_0, which equals the indenter tip radius R_I. The values obtained from Eqs. (6.13), (6.14), and (6.15) with R_0 are denoted with a subscript 0, i.e. a_0, h_0 and S_0, and are written below

$$a_0 = \left(\frac{3R_0P}{8E_r}\right)^{1/3}, \tag{6.17}$$

$$h_0 = \left(\frac{9P}{8R_0E_r}\right)^{1/3}, \tag{6.18}$$

$$S_0 = \frac{dP}{dh_0} = 2a_0E_r. \tag{6.19}$$

In addition, the contact area for indentation on a flat surface can be written as

$$A_0 = \pi a_0^2. \tag{6.20}$$

The ratio of the contact area with specimen surface curvature A to the contact area for a flat surface is obtained with Eqs. (6.12), (6.17), (6.20), and the relation, $A = \pi a^2$,

$$\frac{A}{A_0} = \left(\frac{R}{R_0}\right)^{\frac{2}{3}}. \tag{6.21}$$

Since the Hysitron Picoindenter only measures the vertical load, P, and vertical displacement, h, the machine does not take into account the surface curvatures and possible offsets. The contact area calculated using the measured P and h and the method provided in Chapter 3 and Chapter 4 is the equivalent contact area for a flat surface, rather than the real contact area. Therefore, the calculated hardness based this area is not the true hardness of the specimen. By using Eqs. (6.16), (6.21), and the definition of hardness, we can derive the measured hardness as follows,

$$H_{measured} = \frac{P}{A_0} = \frac{P_n cos\theta}{A}\left(\frac{R}{R_0}\right)^{\frac{2}{3}} = \frac{P_n}{A_n}\left(\frac{R}{R_0}\right)^{\frac{2}{3}} cos^2\theta$$

where P_n / A_n is the true hardness of the specimen. Thus, we have,

$$\frac{H_{measured}}{H_{true}} = \left(\frac{R}{R_0}\right)^{\frac{2}{3}} \cos^2\theta \qquad (6.22)$$

Eq. (6.22) is very similar to Eq. (6.1), which was obtained by Bobji *et al* (1996) except that they derived a power of one for the quantity in the parenthesis. The experimental verification for Eq. (6.22) will be provided in the next section. If the surface of the specimen is flat, Eq. (6.22) gives $H_{measured} = H_{true}$, since $R = R_0$ and $\theta = 0$. Thus, the true hardness can be obtained on a flat surface (this is also called the flat hardness). If the indentation tests are done on a convex part of the surface, such as a bump or an asperity ($R < R_0$), the measured hardness is always smaller than the true hardness. It is not difficult to visualize this result with the help of Figure 6.3.The load and displacement recorded by the Hysitron Picoindenter is the vertical load P and the vertical displacement h. With the assumption of a flat surface, the analysis roughly distributes the resistance from the material over the entire region under the horizontal line, including the excess region. However, the true resistance comes only from the actual bump. Therefore, an analysis based on a flat surface underestimates the resistance, and thus, the hardness of the specimen. It is worth noting that, if the bump radius is much larger than the indenter tip radius ($R \approx R_0$), the measured hardness based on the flat surface assumption is a good approximation of the true hardness.

The offset between the indenter and the specimen lowers the measured hardness by the amount of $\cos^2\theta$. Since the model requires θ to be small, the offset influence $\cos^2\theta$ is also small. For example, $\cos^2\theta$ lowers the measured hardness by about 10% if θ equals 20 degrees.

6.3 EXPERIMENTS

In order to verify Eq. (6.22), nanoindentation tests were first carried out on the top of "sombrero" type laser bumps 5 to 10 μm in diameter and 20 to 30 nm in height. The laser bumps are of the type often used in the parking zones on hard disks to avoid stiction between the sliders and disks. Assuming the bump tips are spherical, their radii of curvature are estimated between 100 and 600 μm. These radii are 3 to 4 orders larger than the tip radii, which range from 50 nm to 200 nm. The term in the parenthesis in Eq. (6.22) therefore has the value close to one for all the bumps. So there is essentially no difference between $H_{measured}$ and H_{true}. To have an effect from the surface curvature, bump radii close to the tip radii are required.

6.3.1 Nanoindentations on asperities

Since it is difficult to find machined surfaces with bump radii of curvature of 50 to 200 nm, nanoindentation tests were performed on the asperities of regular hard disk surfaces. Nearly spherical asperities were chosen as the targets. The indenter was carefully moved to the top of the asperities so that θ in Eq. (6.22) is zero. Before each test, the area around the targeted asperity was scanned with the Hysitron Picoindenter. The radius of curvature for the asperity was then calculated by assuming spherical asperities. The ratio of (R/R_0) was then calculated for each asperity with this radius and for the known tip radius. Indentation forces must be small enough to avoid plastic deformation and interaction with the non-spherical bases of the asperities. In other words, the indentation forces were chosen to elastically deform the very top portion of the asperities. Based on this requirement, the indentation forces ranged from 20 to 50 μN depending on the specimen hardnesses and the indenter tip radii.

Figure 6.4 shows the ratio of the measured hardness to the true hardness vs. R/R_0. The functions, $\frac{H_{measured}}{H_{true}} = \left(\frac{R}{R_0}\right)^{\frac{2}{3}}$ and $\frac{H_{measured}}{H_{true}} = \left(\frac{R}{R_0}\right)$, are also plotted. The smallest asperity radius found was 250 nm whereas most radii were about 500 nm. Since the indenter tip radius was 186 nm, all of the data points in Fig. 6.4 fall in the upper portion of the curve. A power of 2/3 fits the data shown very well. When R/R_0 equals 0.57, the measured hardness is about 70 % of the true specimen hardness. The difference between a function with a power of 2/3 and a linear function is about 15% at R/R_0 of 0.6, or 0 when R/R_0 equals 1. Asperities with radii smaller than 250 nm are rare on disk surfaces. It is even more difficult to indent these asperities without plastic deformation or interaction with their non-spherical bases. Thus, the lower portion of the curve in Fig. 6.4 is left empty.

6.3.2 Random indentations

In the previous section, the model was verified with indentations on single asperities. Questions arise as to how well this model predicts measurement variations on rough surfaces. Therefore, to study the measurement variations, we performed random indentations on rough surfaces. The indenter was moved laterally 1 μm for a sequence of indentations with the scan size staying at zero. In other words, each indentation was made without the knowledge of the local surface topography around the indentation location. Thus, indentations were made on asperities as well as in the concave areas on the surface. The hardness value for each indentation was then calculated with the obtained load/displacement curves. The mean values, $\overline{H}$, and standard deviations, S_H, for all the tests were then calculated. The standard deviation of a set of data x is defined as,

$$S_x^2 = \frac{1}{n}\sum_{i=1}^{n}\left(x_i - \overline{x}\right)^2 \tag{6.23}$$

where n is the number of data points obtained. Two samples were tested using two indenters of different tip radii. The samples were 100 nm hydrogenated carbon (CH_x) and nitrogenated (CN_x) films. The standard deviation of the surface roughness and R_a of sample A were 0.822 nm and 0.63 nm, respectively. The standard deviation of the surface roughness and R_a of sample B were 0.697 nm and 0.548 nm, respectively. R_a is defined as

$$R_a = \frac{1}{A}\iint_A \left|z(x)\right| dx. \tag{6.24}$$

where $z(x)$ is the roughness height function relative to the mean height of the surface. Both indenters were cube-corner diamonds with a tip radius of 186 nm for Tip 1 and 56 nm for Tip 2. Figure 6.5 shows the hardness values for 50 random indentations on sample A indented by Tip 2. The mean hardness and standard deviation are 16.126 GPa and 3.527 GPa, respectively. The mean hardness is taken as the flat or true hardness in Eq. (6.22), which implies that the ratio $\frac{H_{measured}}{H_{flat}}$ equals to $\left(\frac{R}{R_0}\right)^{\frac{2}{3}}$ when θ is zero. We assume that θ is small enough that $\cos^2\theta$ in Eq. (6.22) can be ignored. Next we wish to study how well the standard deviation of the variation of $\frac{H_{measured}}{H_{flat}}$ agrees with the standard deviation of the variation of $\left(\frac{R}{R_0}\right)^{\frac{2}{3}}$. Since the mean hardness $\overline{H}$ (or H_{flat}) is a constant, the standard deviation of $\frac{H_{measured}}{H_{flat}}$ can be expressed as

$$S_{\frac{H_m}{\overline{H}}} = \frac{S_{H_m}}{\overline{H}} \tag{6.25}$$

Therefore, we just need to compare the ratio of the standard deviation of hardness variation S_{H_m} to the mean hardness $\overline{H}$ with a standard deviation of $\left(\frac{R}{R_0}\right)^{\frac{2}{3}}$. The ratio in Eq. (6.25) is called the roughness effect on nanoindentation hardness measurements. Table 6.1 lists the measured hardness values, the mean hardness values, and their ratios for both samples indented by both indenters. Three random indentations with various indentation forces were performed on each sample. The maximum depths ranged from 4 nm to 16 nm. Since the maximum differences in asperity heights of both samples are within 5 nm, it is expected that the contact model loses its accuracy for indentations of maximum depths larger than or comparable to 5 nm.

Next, we turn our focus to finding the standard deviation of $\left(\frac{R}{R_0}\right)^{\frac{2}{3}}$ for both surfaces. Because not all of the asperities and the concave areas on the surface are spherical or close to spherical, special care is needed to implement the contact model. Greenwood (1967) and Ling (1973) indicated that it is sufficient to characterize a random surface with a profilometric representation along a straight line. Therefore, a line with the same roughness standard deviation as the entire surface is chosen to represent each of the two disk surfaces assuming that the surfaces are random. Figure 6.6 shows a typical scanned line of sample A. Note that the vertical dimension has been exaggerated. The asperities on this line are then approximated by solids of revolution with spherical top portions. If z_{i+1}, z_i, and z_{i-1} are three consecutive heights on the scanned line, according to Johnson (1987), the curvature is defined by,

$$\kappa_i = \frac{z_{i+1} - 2z_i + z_{i-1}}{h^2}, \tag{6.26}$$

where h is the length of the increment intervals in nanometers, and κ_i is the curvature of the ith data point. For an image 1 μm by 1 μm scanned with 256 lines, h equals 3.90625 nm. The radius of curvature is obtained by taking the reciprocal of κ_i, i.e. $r_i = 1/\kappa_i$. If we assume that the asperities are solids of revolution, the radii of curvature of one asperity in both principal directions will be r_i. A positive r_i represents an asperity; while a negative one indicates a cavity on the surface. All asperities with positive radii are likely to be hit by the indenter during random indentations. However, the indenter is not able to reach the cavities whose radii are smaller than the indenter tip radius. For simplicity, we disregard these cavities, which means that we view these areas as flat. The statistical properties of the surface such as the standard deviation of roughness will be slightly changed due to this simplification. The modified radii of curvature are called the apparent radii of curvature for the indenters. Since different indenters have different tip radii, the apparent radii of curvature of the surface will be different for the indenters. It is expected that the standard deviation of the apparent radii of curvature of the same surface is larger for sharper indenters. Recall that the effective radius of curvature R_i of the indenter/specimen system is defined as,

$$\frac{1}{R_i} = \frac{1}{r_i} + \frac{1}{R_0}. \tag{6.27}$$

Table 6.2 lists the standard deviation of the apparent radii of curvature as well as other statistical properties for both sample surfaces for both indenters. It is not a surprise that Sample A has smaller mean radii of curvature and standard deviation of radii of curvature than Sample B, since Sample A is rougher. The standard deviation of $\left(\frac{R_i}{R_0}\right)^{\frac{2}{3}}$ for Sample A is larger than that of Sample B for the same reason. Cross-comparison of the surface properties for different indenters suggests that surface roughness has a stronger influence for a sharper indenter. This finding also agrees with our intuition.

The standard deviations of $\left(\frac{R_i}{R_0}\right)^{\frac{2}{3}}$ are compared with the hardness measurements obtained earlier. Figures 6.7 and 6.8 show the ratios of the standard deviation to mean hardnesses for Sample A and Sample B, respectively. Each data point in the figures represent the result from 50 random indentation tests. The standard deviation of $\left(\frac{R_i}{R_0}\right)^{\frac{2}{3}}$ for each combination is listed in the legend. From both figures, it is seen that the standard deviation to mean ratio increases as the maximum depth decreases. This implies that the deformation mechanism for smaller indentation depths is closer to the assumptions used in the contact model, because the indentation sizes are close to the roughness for small indentations. The ratios achieve the value of the standard deviations of $\left(\frac{R_i}{R_0}\right)^{\frac{2}{3}}$ for Sample A indented by Tip 1 and Tip2 at maximum depths of 6 nm and 4 nm, respectively. And the ratios acquire the value of the standard deviation of $\left(\frac{R_i}{R_0}\right)^{\frac{2}{3}}$ for Sample B at 7 nm and 4 nm for Tip 1 and Tip 2, respectively. The slope of the "Tip 2" curve in Fig. 6.7 is significantly larger than that of the "Tip 1" curve. This indicates that the roughness effect decays faster for a sharper indenter, although it is stronger for such an indenter at very small depths. Although there is also a slope in Fig. 6.8, it is not as significant. Cross-comparing the curves generated by the same indenter on different samples, we find that the roughness effect is stronger and decays faster on the rougher surface. The latter may due to the hardness difference between the two samples. It is concluded that the contact model together with the assumptions and simplifications predicts the variation of indentation hardness measurements well for indentations whose sizes are comparable to the roughness. The roughness effect can be calculated using the procedure presented here before any indentation is made. Note that there is no plastic deformation for the shallowest indentations for the four cases, i.e. the residual depths are zero. For thin film materials, we need to keep the residual depths less than 20% of the film thickness to avoid the substrate effect on the indentation hardness measurements. The contact model for the roughness effect should still be valid for films thinner than, say 4 nm, since residual depths are already zero for the cases in this study.

6.4 SUMMARY AND CONCLUSIONS

A model for the indentation of surfaces with curvature, such as bumps and asperities, is proposed. The power of 2/3 of the ratio R/R_0 is verified experimentally on surface asperities with radii of curvature ranging from 250 nm to 2 μm. The model is then adopted to study the roughness effect on indentation hardness measurements. The concept of the apparent surface properties for a specific indentation is proposed. For indenters with different tip radii, this would result in slightly different surface properties. The ratio of the standard deviation to the mean hardness is compared with the apparent standard deviation of $\left(\frac{R_i}{R_0}\right)^{\frac{2}{3}}$, where R_i is the relative radius of curvature and R_0 is the indenter tip radius. The results show that at very small indentations the ratios of the standard deviations to the mean hardnesses equal the standard deviation of $\left(\frac{R_i}{R_0}\right)^{\frac{2}{3}}$ for all of the sample and indenter combinations. This means that the roughness effect on the indentation hardness measurements can be predicted with only the knowledge of the surface properties and tip radii using the model proposed here.

Table 6.1: Mean hardness, standard deviation, and their ratios for random indentation hardness measurements.

Indenter	Hardness Properties	Sample A	Sample B
Tip 1 (186 nm)	Mean (GPa)	16.216	6.213
	Standard Deviation (GPa)	2.661	1.275
	SD/Mean ratio	**0.164**	**0.205**
	Mean (GPa)	17.027	5.948
	Standard Deviation (GPa)	8.718	2.790
	SD/Mean ratio	**0.512**	**0.469**
	Mean (GPa)	16.521	6.545
	Standard Deviation (GPa)	15.348	4.084
	SD/Mean ratio	**0.929**	**0.624**
Tip 2 (56 nm)	Mean (GPa)	16.126	6.180
	Standard Deviation (GPa)	3.527	0.826
	SD/Mean	**0.219**	**0.134**
	Mean (GPa)	16.385	6.951
	Standard Deviation (GPa)	9.962	4.380
	SD/Mean ratio	**0.608**	**0.63**
	Mean (GPa)	14.956	6.025
	Standard Deviation (GPa)	17.484	4.687
	SD/Mean ratio	**1.169**	**0.778**

Table 6.2: The apparent properties of the surfaces of both samples

Indenter	Apparent surface properties	Sample A	Sample B
Tip 1 (R_0=186 nm)	Mean of radii of curvature (nm)	-32.03	-83.02
	S.D. of radii of curvature (nm)	366.65	2268.93
	S.D. of $(R_i / R_0)^{2/3}$	**0.932**	**0.640**
Tip 2 (R_0=56 nm)	Mean of radii of curvature	-58.45	-98.35
	S.D. of radii of curvature	398.64	2298.80
	S.D. of $(R_i / R_0)^{2/3}$	**1.171**	**0.789**

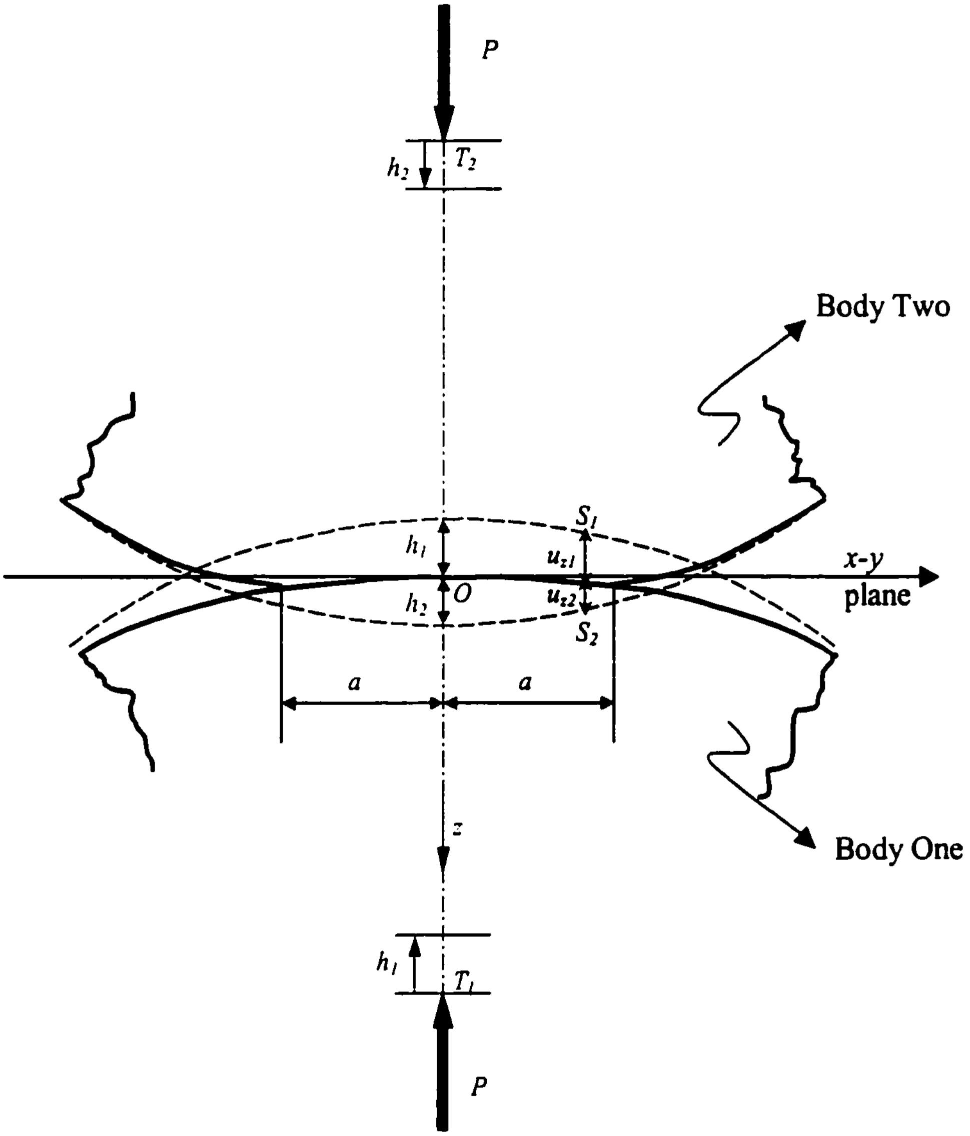

Fig. 6.1: Contact of two solids of revolution on the areas around their apex points.

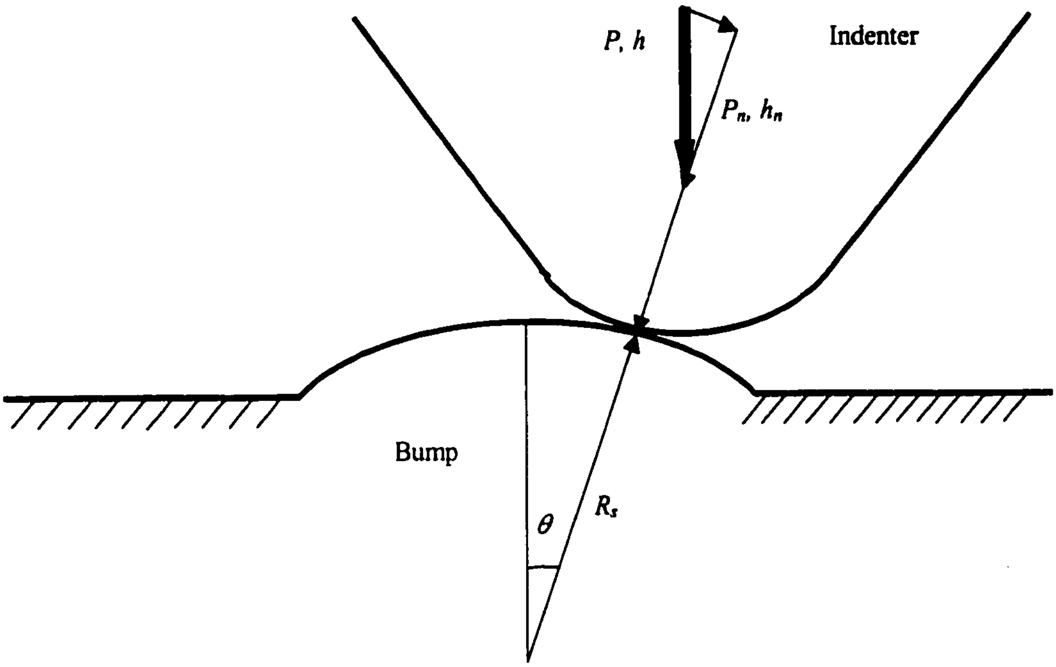

Fig. 6.2: Indentation on a spherical bump with offsets

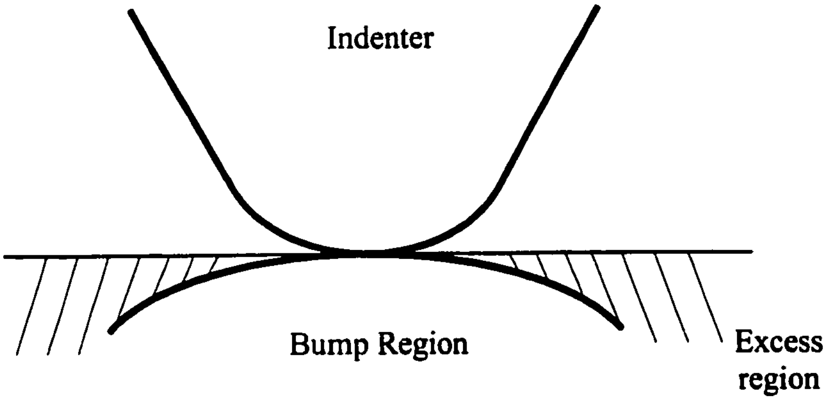

Fig. 6.3: Illustration of the idea showing that the measured hardness is lower than the true hardness.

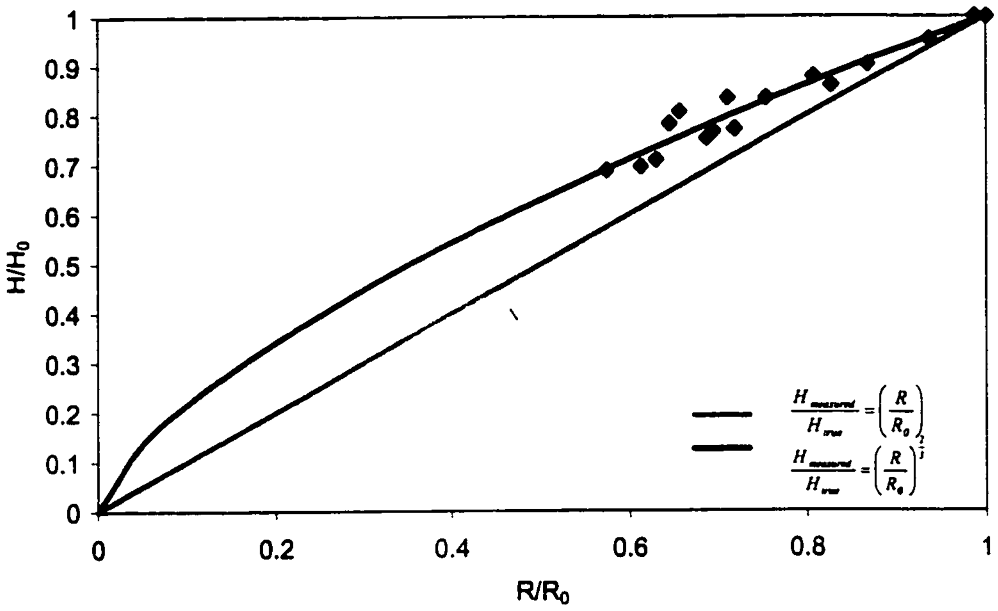

Fig. 6.4: Indentations on spherical asperities. The data shown agree with the contact model derived from Hertz contact theory.

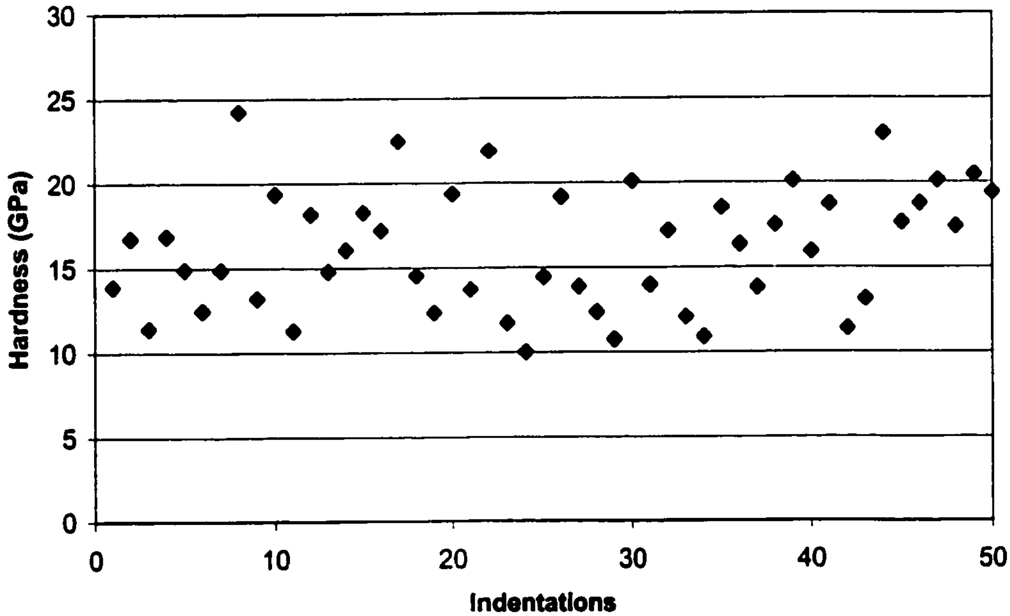

Fig. 6.5: Random indentations on sample A using an indenter with a tip radius of 56 nm.

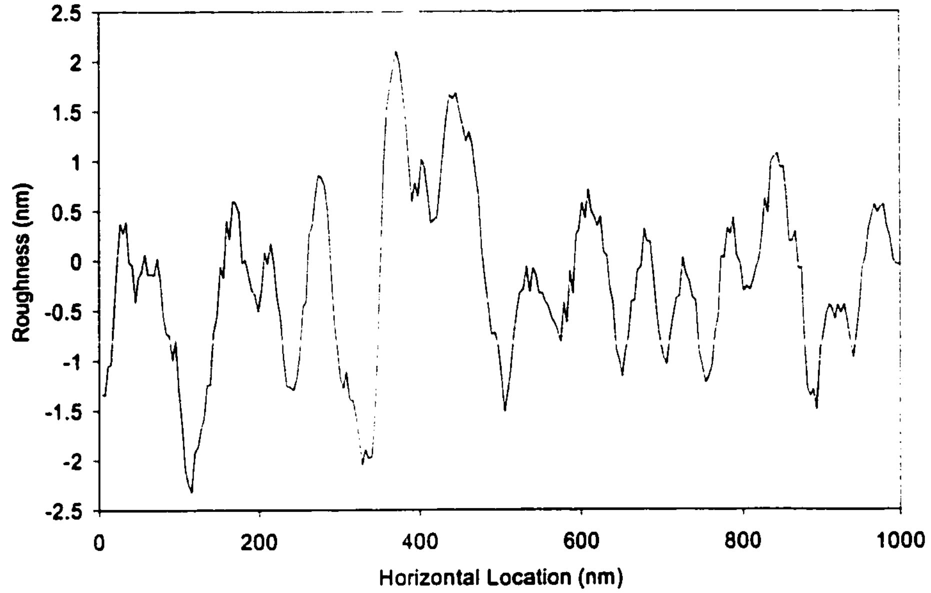

Fig. 6.6: A typical line from the scanned image of sample A surface. Note that the vertical dimension has been exaggerated.

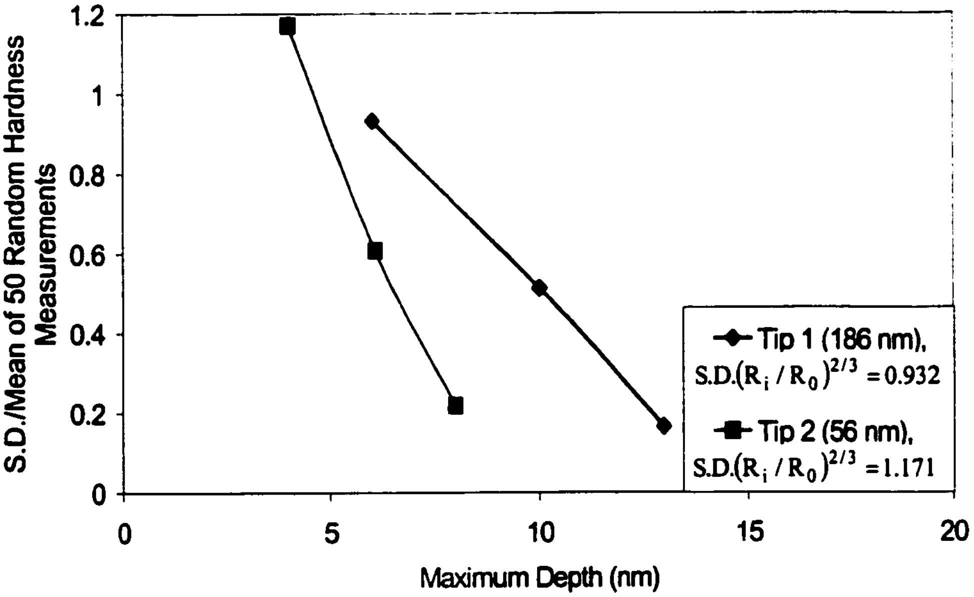

Fig. 6.7: The ratios of standard deviations to mean hardnesses of Sample A indented by Tip 1 and Tip 2. Each data point represents the result of 50 random indentations. The apparent standard deviations of $(R_i / R_0)^{2/3}$ for both tips are listed in the legend.

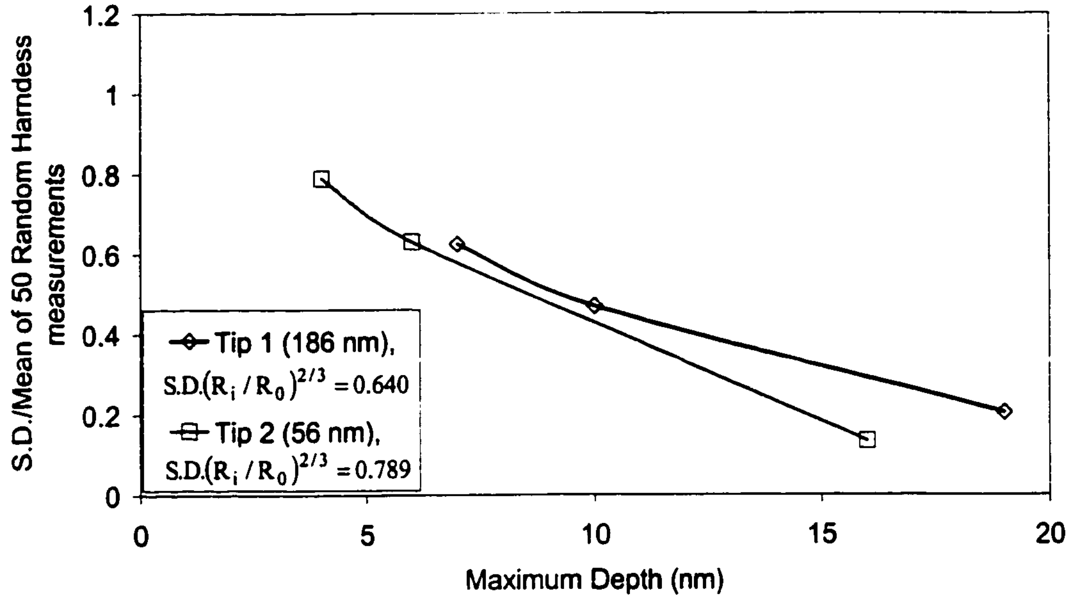

Fig. 6.8: The ratios of standard deviations to mean hardnesses of Sample B indented by Tip 1 and Tip 2. Each data point represents the result of 50 random indentations. The apparent standard deviations of $(R_i/R_0)^{2/3}$ for both tips are listed in the legend.

Chapter 7

CHARACTERIZATION OF CATHODIC ARC AMORPHOUS CARBON FILMS

7.1 INTRODUCTION

The demand for higher storage density of magnetic storage devices has led to extremely small spacing between the disk and slider, and thus continues to push the protective layers on these two components to ever-smaller thicknesses. An ideal overcoat should possess high hardness, low friction properties, and excellent wear and corrosion resistance. Sputtered amorphous carbon films incorporating hydrogen (CH_x), nitrogen (CN_x), or nitrogen and hydrogen (CN_xH_y) have been developed and are used for most drives today. However, their superior properties deteriorate as their thicknesses become too small. For future hard disk drives with target areal densities exceeding 10 Gb/in^2, the magnetic spacing needs to be substantially reduced. Much thinner films (5 nm or less) are needed to achieve this goal. Researchers are working to improve the properties of current films in this regime and also exploring alternative materials.

Anders et al. (1994), Ager III et al. (1995), and Pharr et al. (1996) have developed and studied cathodic-arc deposited amorphous hard carbon films to achieve this goal. Cathodic-arc amorphous films deposited at ion energies of 100 eV possess hardness close to that of diamond due to the high fraction of tetrahedral (sp^3) bonding in the film, which is typically found in crystalline diamond. Therefore, these films are also called cathodic-arc diamond-like (or CA-DLC) films. The hardness of these films is usually measured by nanoindentation techniques. Since their hardness approaches that of diamond, some deformation of diamond indenters is expected to occur and the rigid indenter assumption can no longer be applied. Friedmann et al. (1997) have developed a finite element model to find the contact areas between the indenters and the films and thus, the true hardnesses and elastic modulii of the films. Several researchers have reported that the hardnesses and elastic modulii of these films are thickness dependent. Pharr et al. attributed the thicknesses dependence to the substrate effects, but they did not provide detailed discussion. It is also possible that the thickness dependence is a property of the films. More work needs to be done on this issue.

The purpose of this study is to investigate the thickness dependence of the mechanical properties of the cathodic-arc DLC films. Nanoindentation tests were carried out on films with two tips of different tip radii using the Hysitron tester to study the tip radius effects on the measurements. To study the substrate effects on the measurements, tests were also conducted on films having silicon substrates with and without 100 nm permalloy sublayers. It was concluded that the tip radius effect and the substrate effect are not the causes of the observed thickness dependence phenomenon. Possible causes associated with the film structures are discussed.

7.2 FILM PREPARATION

In our study, cathodic-arc DLC films were deposited on low resistivity, one inch diameter silicon wafers with and without 100 nm permalloy layers. The permalloy layer consisted of 80% nickel (Ni) and 20% iron (Fe). Silicon wafers were chosen as the reference substrate with hardness values of 12 GPa while the permalloy substrates were used because of their relatively lower hardness of 6-8 GPa. A total of eleven films were deposited in a range of film thicknesses from 6.6 to 66 nm – eight films on Si and three films on the permalloy. A catalog of the samples is given in Table 7.1. All CA-DLC depositions on silicon substrates used a 90° bent filter for macroparticle reduction, and a magnetic duct was employed for uniform expansion of the plasma at the filter exit. The following parameters were used in these depositions: (1) an arc pulse with a current of 300A for 5 ms durations and a frequency of 1 Hz, and (2) a pulsed substrate bias with a 33% duty cycle (2 μs on/ 6 μs off). The same parameters were used for depositions on the permalloy substrates but the filter was an S-duct filter (two 90° bent filters connected in series) with two magnetic ducts at the filter exit. These changes in the filter should not affect the material properties of the films; the S-duct filter reduces the number of macroparticles impinging on the substrate and the additional magnetic duct provides a larger, uniform deposition area. However, these changes do result in a decrease in the transmission of plasma from the cathode to the substrate (< 2% total output), which accounts for the increase in deposition time to fabricate a CA-DLC film of the same thickness on silicon and permalloy substrates.

7.3 NANO-INDENTATION TESTS

7.3.1 Nanoindentations on films deposited on silicon with a 150 nm radius tip (tip 47)

Nanoindentation tests were carried out to determine the hardnesses and modulii of the films. The films deposited on silicon substrates were first studied with tip 47, which has a tip radius of 150 nm. Residual depths of indentations were between 0 and 40 nm. Maximum normal loads were allowed to vary from sample to sample as long as the residual depths fell in the range mentioned above. Figures 7.1 and 7.2 show the hardnesses and modulii, respectively, as functions of the residual depth for the four thinner films measured by tip 47. Figures 7.3 and 7.4 show the hardnesses and modulii, respectively, of the rest of the films. The modulii plotted in Figs. 7.2 and 7.4 are the true elastic modulii, instead of the reduced modulii of the indenter/material assembly. The four thinnest films have hardnesses on the order of 15-20 GPa. However, the hardnesses of the four thickest films are about 30 – 40 GPa or higher. The 66 nm film is as hard as 50 GPa at shallow indentations. In addition, the modulii of the four thinner films are about 160 GPa or less. But, the modulus of the 66 nm film can be as high as 240 GPa. Although thickness or deposition time is their only difference, the CA-DLC films do not have the same hardnesses and modulii for the residual depth range shown. Note that films thicker than 44 nm show drops in hardness and modulii at the shallowest indentations. Such drops were not seen for the thinner films. For larger indentations, the measured hardnesses are predominantly those of the substrates, since in this case the tip penetrated the film into the substrate. Therefore, the difference in hardness of the films at the larger indentations can be interpreted as a substrate effect. The substrate effect can usually be neglected at small enough indentations. However, as seen in Figs. 7.1 to 7.4, films with different thicknesses do not have the same hardnesses and modulii even at very small indentations. This raises the concern of whether the measured hardnesses are the true hardnesses of the films, or if there are potential inherent measurement errors with the testing techniques. Lu and Bogy (1995) indicated that the true hardness can only be obtained by nanoindentation techniques with mathematically sharp indenters. According to Lu and Bogy, the hardness of the film can be measured accurately as the ratio of tip radius to film thickness approaches zero. If the ratio equals 1.25, the measured hardness drops to 88% of the true hardness of the material in the plastic depth scenario, or 80% in the residual depth scenario. If the ratio equals 2.5, the measured hardness drops to 66% of the true material hardness in the plastic depth scenario and 0 in the residual depth scenario. Further increase of the tip-radius to film-thickness ratio results in continuous drops of the measured hardnesses. For the films tested here with tip 47, the radius to thickness ratio ranges from 2.27 to 22.72. Therefore, the radius to thickness ratios are much higher than the values required to get reliable hardness values of the films using their method. However, in calculating hardness, the areas adopted in Lu and Bogy's analyses are the plastic areas based on the plastic depths and the residual areas from the final shapes of the indentation mark, both of which are different from the contact areas used in this study. Moreover, their analysis was based on rigid indenters, and they did not incorporate the experimentally possible indenter deformation. Therefore, it is of interest to see if the tip radius plays a role in the measured hardness when using the contact area definition.

7.3.2 Nanoindentations on films deposited on silicon with a tip of 50 nm radius (tip 9)

Tip 9, with a tip radius of about 50 nm, was used to study the tip radius effect on the hardnesses of the samples. The tip radius to thickness ratio is reduced by a factor of three for this tip as compared to tip 47, ranging from 0.75 to 7.57. According to Lu and Bogy, more accurate film hardness values can be obtained with smaller radius to thickness ratios. Furthermore, since the tip radius is only 50 nm and some of the films are as hard as 50 GPa, possible deformation of the tip is to be expected. Figures 7.5 and 7.6 show the hardnesses and modulii respectively of the four thinner films measured by tip 9. The measurements by tip 47 are also shown for comparison. Clearly, for the samples in these two figures, there is no significant difference between the measurements made by tip 47 and tip 9. The films still show high hardnesses at smaller indentations and low hardnesses at larger indentations, because of the substrate effects at large indentations. Samples of different thicknesses still have different hardnesses for the entire range shown. Figures 7.7 and 7.8 show the hardnesses and modulii respectively for the other four films. No significant differences in the measured hardness and modulus values can be observed for the 23.5nm (DLC 634) film using tip 47 and tip 9. However, for thicker films, there are observable differences between the measurements made by tip 47 and tip 9. The relative difference in modulus between the two measurements is smaller than the difference in the hardness measurements. There are two possible causes for the differences. One is the tip radius effect, as indicated by Lu and Bogy, and the other is the deformation of the sharper tip while indenting on the thickest three films. To investigate the possible deformation of tip 9, the procedure presented in Chapter 4 was adopted to calculate the true contact areas at maximum loading for each indentation.

Figures 7.9 and 7.10 show the corrected hardnesses and modulii values measured by tip 9 and those measured by tip 47 for the four thinner films originally shown in Figs. 7.5 and 7.6. There is no change in hardness due to the correction. This indicates that tip 9 did not deform while indenting these four samples. The hardness values measured by tip 9 are essentially the same as those measured by tip 47. Figures 7.11 and 7.12 show the corrected hardness and modulus values respectively for the four thicker samples. The measurements made using tip 47 are also shown in these two figures for comparison. After compensating for the indenter deformation, the hardness values obtained by tip 9 do not show significant differences from those measured by tip 47. Again, films of different thicknesses do not have the same hardness for the entire depth range tested. Therefore, indenter deformation is the cause for the difference in hardness measured by two different tips, and so, tip radius does not have an effect on the measured hardness.

7.3.3 Nanoindentations on films deposited on permalloy using a tip of 50 nm radius (tip 9)

Pharr et al. (1996) measured the hardnesses of some similar cathodic-arc DLC films that are much thicker than the films tested here. They also reported different hardnesses for films of different thicknesses. They point out, "the fact that there are no clear plateaus in small-depth hardness indicates that the measured values for the cathodic-arc films are not substrate independent". They suspected that the measured film hardnesses were much lower than the real film hardnesses due to the substrate effects and suggest that the real hardnesses of the cathodic-arc DLC films could be as high as that for diamond. To allay this suspicion, three cathodic-arc DLC films, with thicknesses of 6.6, 18, and 66 nm, were deposited on permalloy (NiFe) underlayers, which has good conductivity, low surface roughness and, most importantly, a low hardness of 6-8 GPa. If the substrate plays an important role in the measured hardness of the films, the measured values for NiFe substrates would be lower than those for the same films on silicon, since silicon is almost two times harder than NiFe.

Figures 7.13 and 7.14 show the hardnesses and modulii of the three films deposited on permalloy and measured by tip 9. The values shown have been corrected for indenter deformation. The hardnesses of the three corresponding films on silicon are also shown for comparison. It is clear from these figures that there is no significant difference in hardness values at shallow indentations between the films on silicon and NiFe. At larger indentations, however, the measured hardnesses of the films on NiFe are lower than those on silicon. Furthermore, the modulii of the films on NiFe are much higher than the film modulii on Silicon at larger indentation. The rate of decrease of hardnesses and modulii due to the increase of residual depth are lower for the films on silicon than for those on NiFe. This is expected because the substrate plays an important role for large indentations. Therefore, there are measurable differences in hardness due to different substrates and the differences could only be seen for large indentations. This means that the measured hardnesses at shallow indentations are substrate-independent. Therefore, the substrate effect is also not the cause of the thickness dependence in hardnesses of the cathodic-arc DLC films. The measured hardnesses and modulii are, thus, test instrument independent and the thickness dependence phenomenon at small indentation is a material property of the cathodic-arc DLC films.

7.4 Discussion

As reported by McKenzie et al. (1991), "a study of the surface plasmon excitation shows that the surface material (of a tetrahedral amorphous carbon film) is almost entirely sp^2 carbon as predicted." They did not estimate the thickness of the surface layer. Gilkes et al. (1993) indicated that the maximum thickness of the sp^2-bonded surface layer is 0.9 nm. Davis, et al. also observed a 1.3±0.3 nm sp^2-bonded surface layer in their study of the cross-section structure of an amorphous carbon film. Pharr et al. (1996) mentioned that "a cathodic-arc DLC film has a surface layer of about 20 nm, which is structurally different and softer than the bulk." They also indicated that the surface layer is predominately sp^2-bonded, unlike the sp^3-bonded bulk, which is structurally similar to a diamond. If the "twenty percent[1]" rule applies to the conditions here, the thickness of the surface layer is estimated at 16 to 20 nm by the nanoindentation techniques. Since the published values of the thickness of the surface layer vary from about 1 nm to 20 nm, no confirmation of the thickness can be drawn at this moment. However, the existence of an sp^2-bonded surface layer above the sp^3-bonded bulk is confirmed.

The existence of this layer explains the thickness dependence phenomenon of mechanical properties of the cathodic-arc DLC films. For films thinner than a certain value, for example 20 nm, the entire films are mostly sp^2 bonded. For thicker films there is more sp^3 bonding. Therefore, a 6.6 nm film would have a higher sp^2/sp^3 bonding ratio than an 18 nm

---

[1] The true film hardness can be measured by the nanoindentation techniques if the indentation residual depth is below 20% of the film thickness. This rule has been discussed in Chapter 5.

film does. This explains why there are differences in the mechanical properties of films thinner than 20 nm and also why no observable drops occur in the mechanical properties of these films at shallow indentations. A film thicker than 20 nm has a top sp^2 layer along with a lower layer that is mostly sp^3 bonded. For films much thicker than 20 nm, their top layers are relatively thin, compared to the hard sp^3 bonded bulk layer. Therefore, thicker films show higher hardnesses and elastic modulii at deeper indentations and there are drops in these values at shallow indentations.

7.5 SUMMARY AND CONCLUSIONS

Cathodic-arc DLC films were deposited on silicon and permalloy and tested by nanoindentation techniques to determine their hardnesses and elastic modulii. Two diamond indenters of different tip radii were used to study the tip radius effect on these films. After compensation for deformation of the sharper tip, the measurements made by both tips were consistent. Both hardnesses and elastic modulii are thickness dependent for these films. Comparing the test results for the films deposited on silicon and permalloy, we find the measurements at shallow indentations are nearly the same and the substrate effects could only be observed for large indentations. This suggests that the measured hardnesses and elastic modulii at shallow indentations are true properties of the films. There are no inherent errors due to the nanoindentation testing techniques. The thickness dependence phenomenon is one of the material properties of these films.

A possible explanation for this phenomenon can be drawn from the existence of top layers associated with the CA-DLC films. The films are predominately sp^2 bonded up to certain thicknesses. Beyond that there is an sp^2 bonded softer top layer on the sp^3 bonded bulk. If the films are thinner than the top layer thickness, the films are soft and no drops in mechanical properties can be seen at shallow indentations. If the films are thicker than the sp^2 top layer thickness, the films are harder and drops at shallow indentations can be observed. These drops are the indicators for the existence of the softer top layers. The thicknesses of the top layers are estimated at 16 to 20 nm. There are no published thicknesses available other than the rough estimation by Pharr et al.

Although the cathodic-arc DLC films have extremely high hardnesses and elastic modulii at the bulk region, they always have top layers that are much softer than the bulk. Such soft layers can be observed with the nanoindentation techniques for films thicker than 23.5 nm. Therefore, the mechanical properties of the CA-DLC films are inherently thickness-dependent.

Table 7.1: Cathodic-arc carbon sample descriptions.

Sample number	Substrate	Film thickness (nm)	Number of arc pulses at −1 kV substrate bias	Number of arc pulses at −100V substrate bias
DLC668	Silicon	6.6	5	45
DLC665		10.4	10	90
DLC667		17.7	30	270
DLC666		18.2	20	180
DLC634		23.5	100	900
DLC635		44	100	1400
DLC632		49	100	2400
DLC633		66	100	2400
DLC858	Permalloy	6.6	100	1394
DLC856		18	100	3552
DLC855		66	100	5378

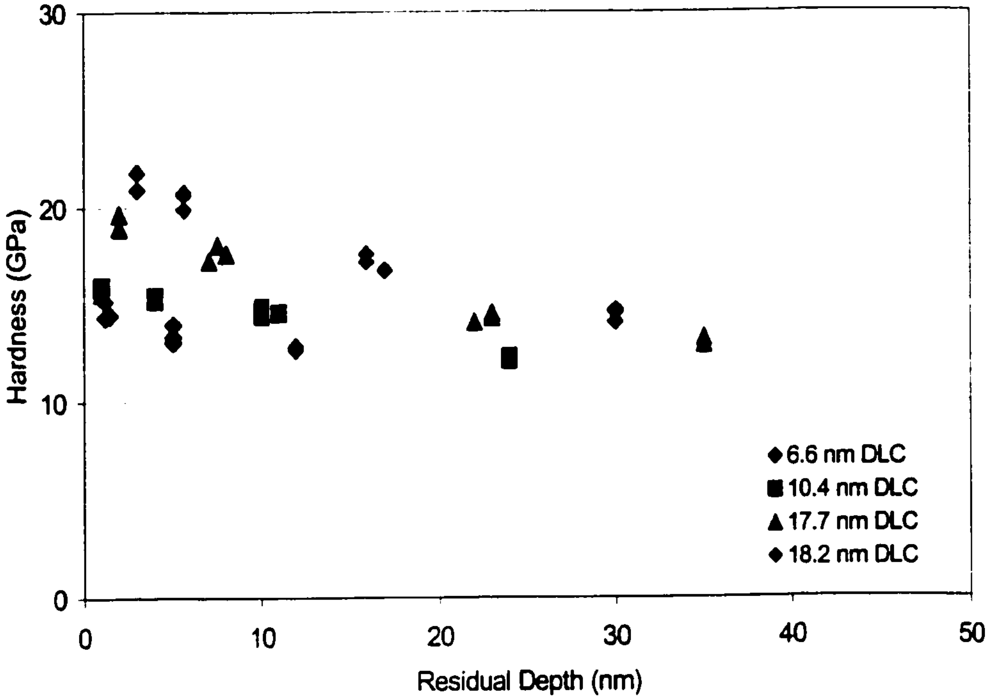

Fig. 7.1: Hardnesses of the four thinner cathodic arc DLC films.

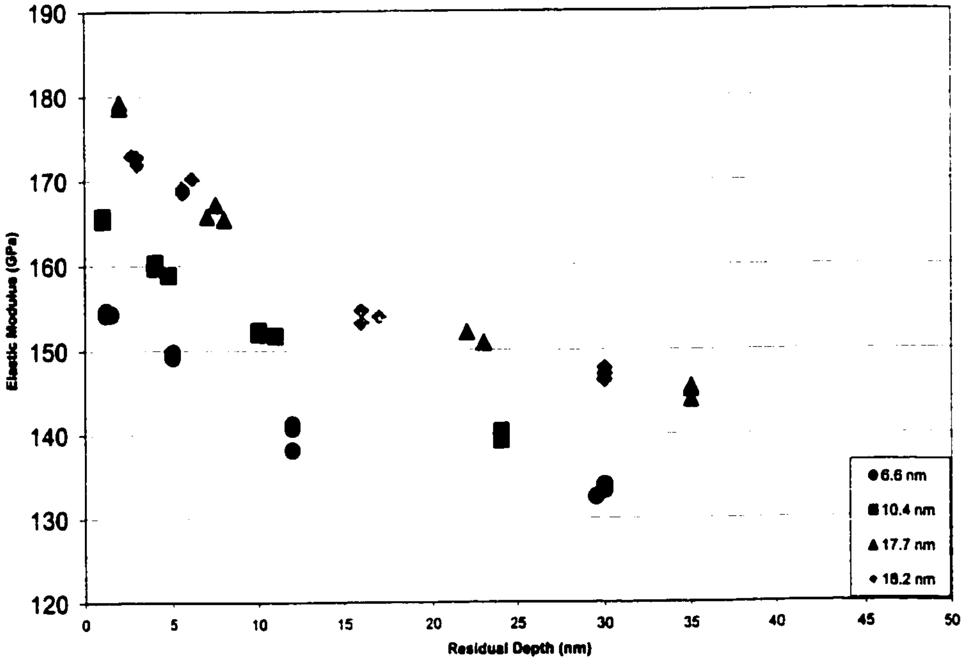

Fig. 7.2: Modulus of the thinner four cathodic arc DLC films.

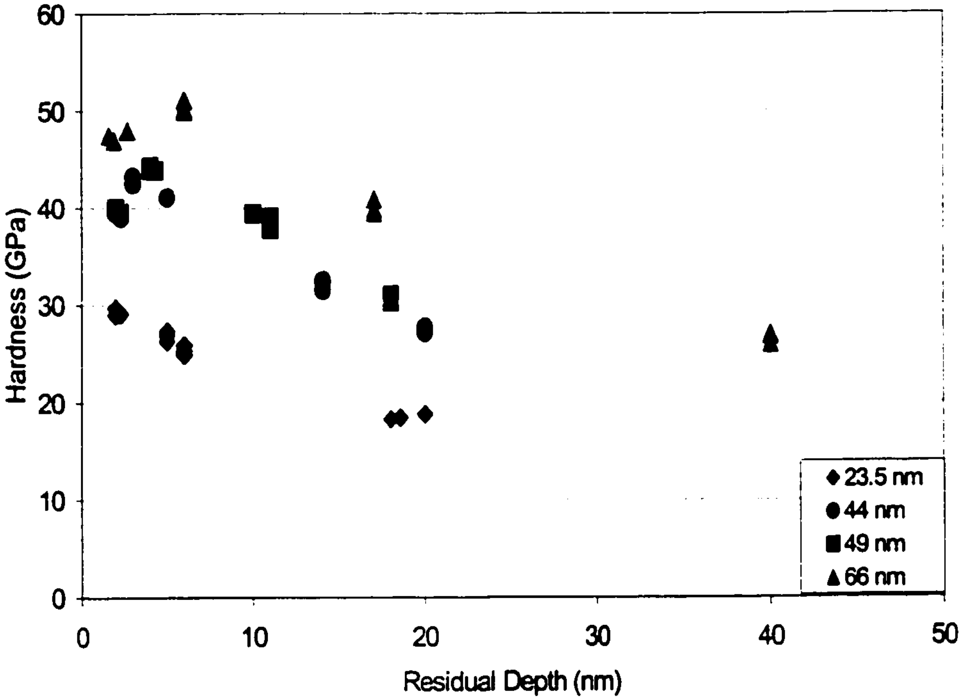

Fig. 7.3: Hardnesses of the thicker four cathodic-arc DLC films.

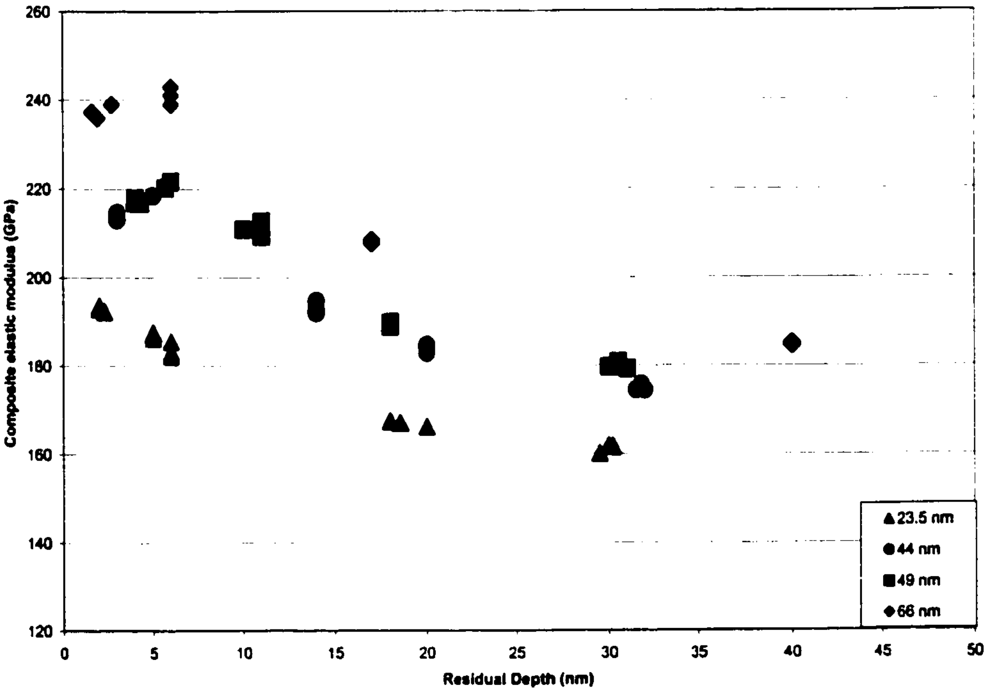

Fig. 7.4: Modulii of the thicker four cathodic-arc DLC films measured by tip 47, which has a tip radius of about 170 nm.

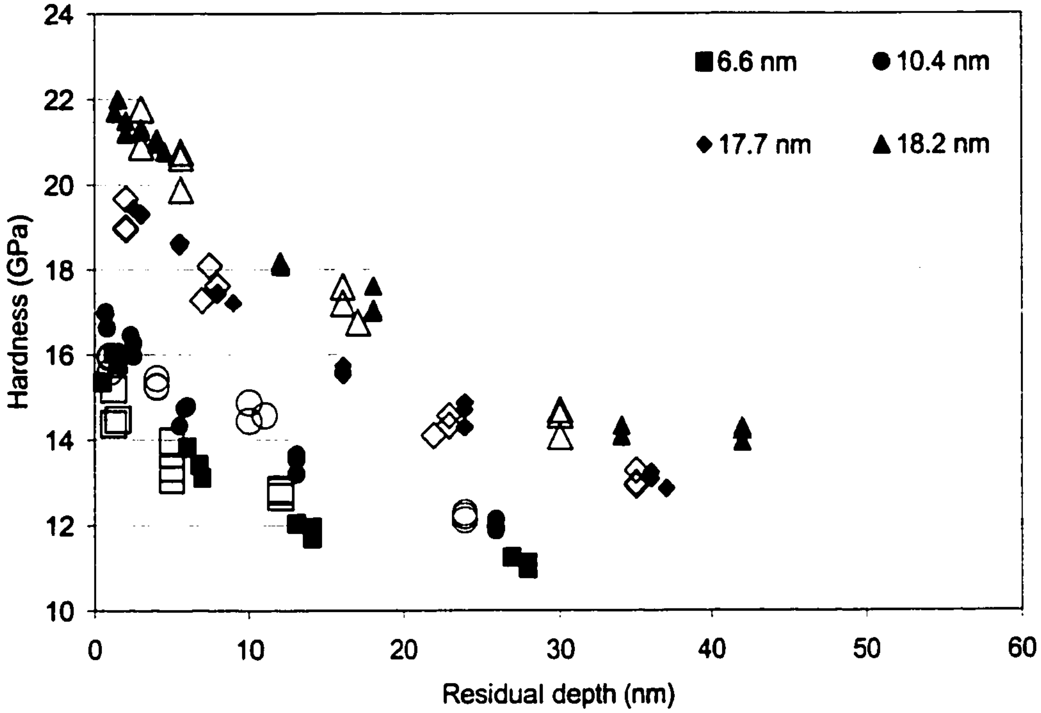

Fig. 7.5: Hardnesses of the thinner four films measured by tip 9 (Solid symbols) compared to those measured by tip 47 (Empty symbols).

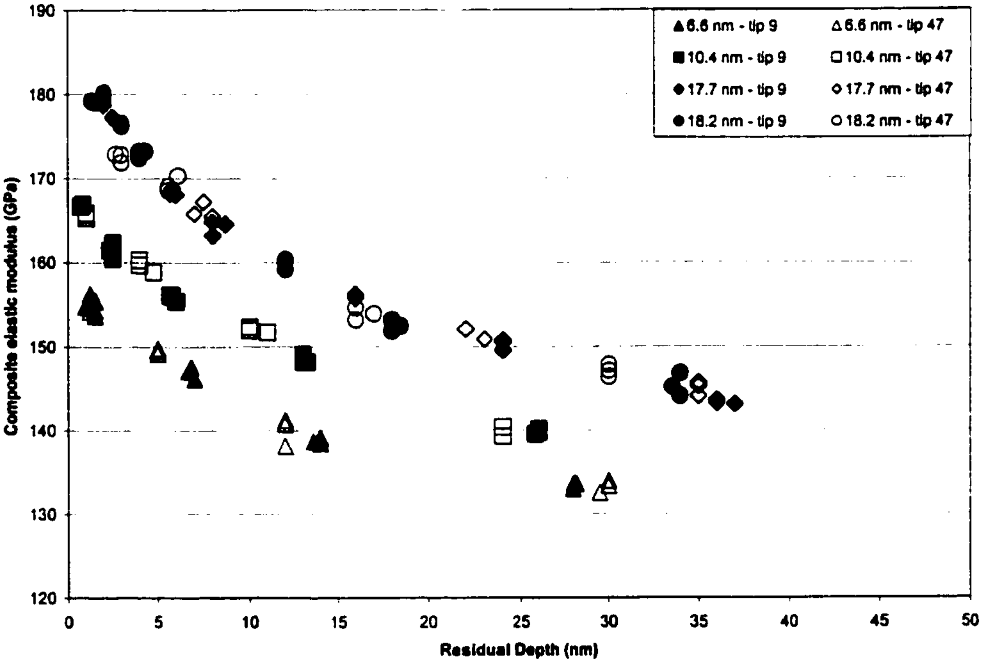

Fig. 7.6: Modulii of the thinner four films measured by tip 9 (Solid symbols) compared to those measured by tip 47 (Empty symbols).

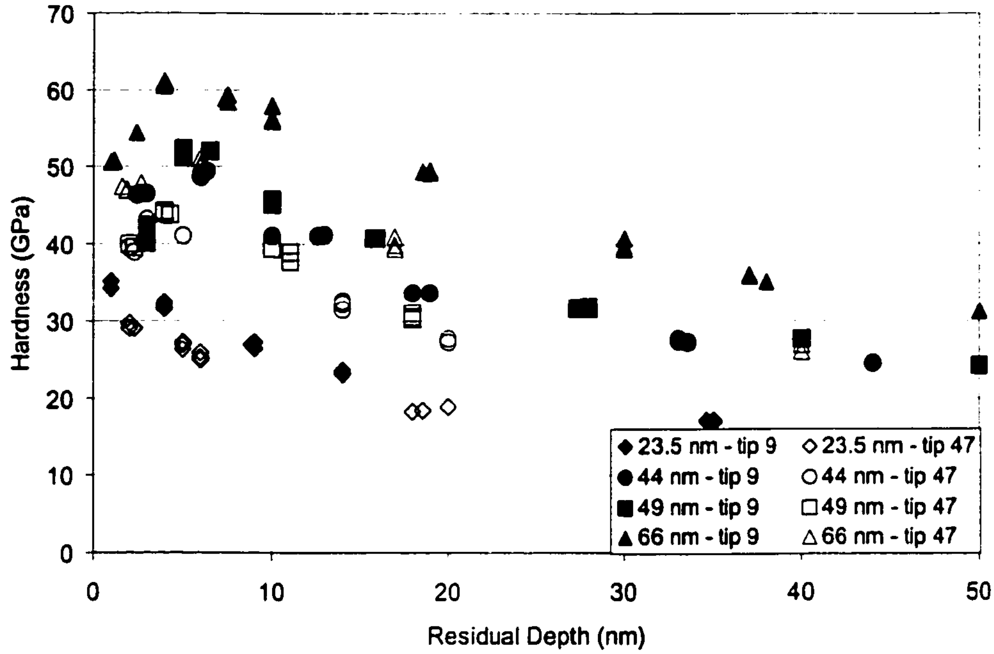

Fig. 7.7: Hardnesses of the thicker four films measured by tip 9 (Solid symbols) compared to those measured by tip 47 (Empty symbols). Indenter deformation is not considered yet.

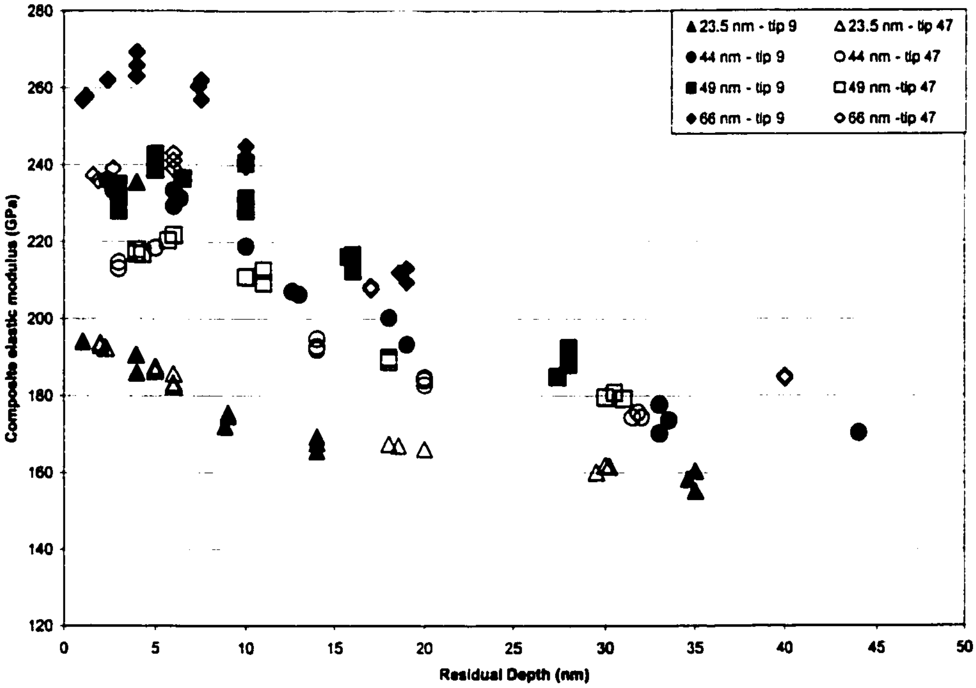

Fig. 7.8: Modulii of the thicker four films measured by tip 9 (Solid symbols) compared to those measured by tip 47 (Empty symbols).

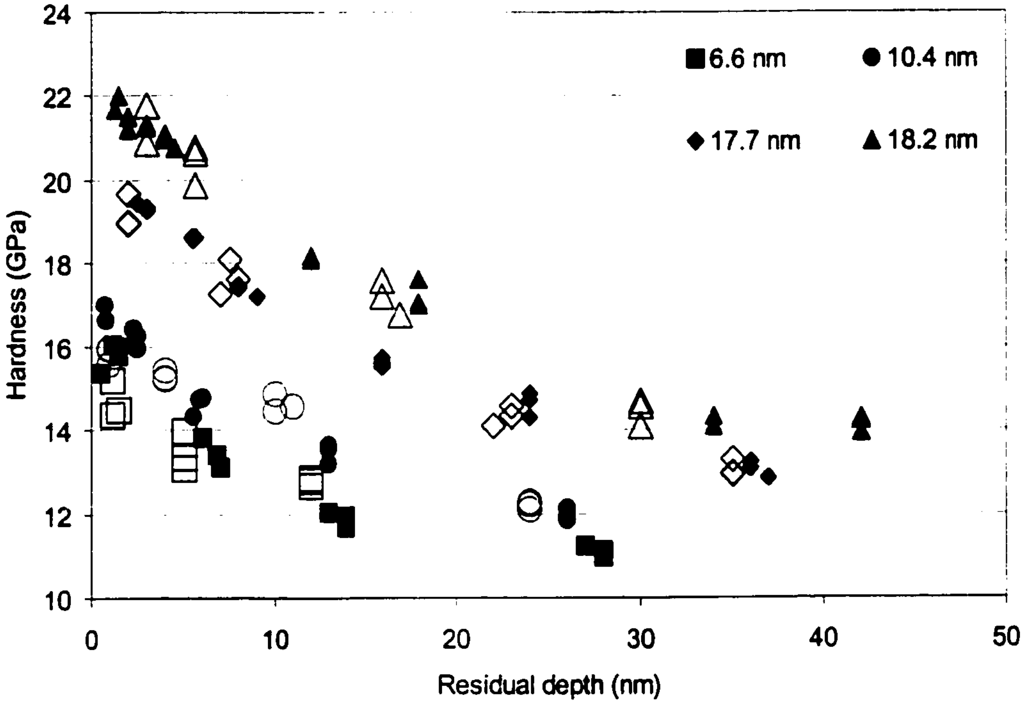

Fig. 7.9: Hardnesses of the thinner four films measured by tip 9 and corrected for the indenter deformation. No difference observed for data before and after correction.

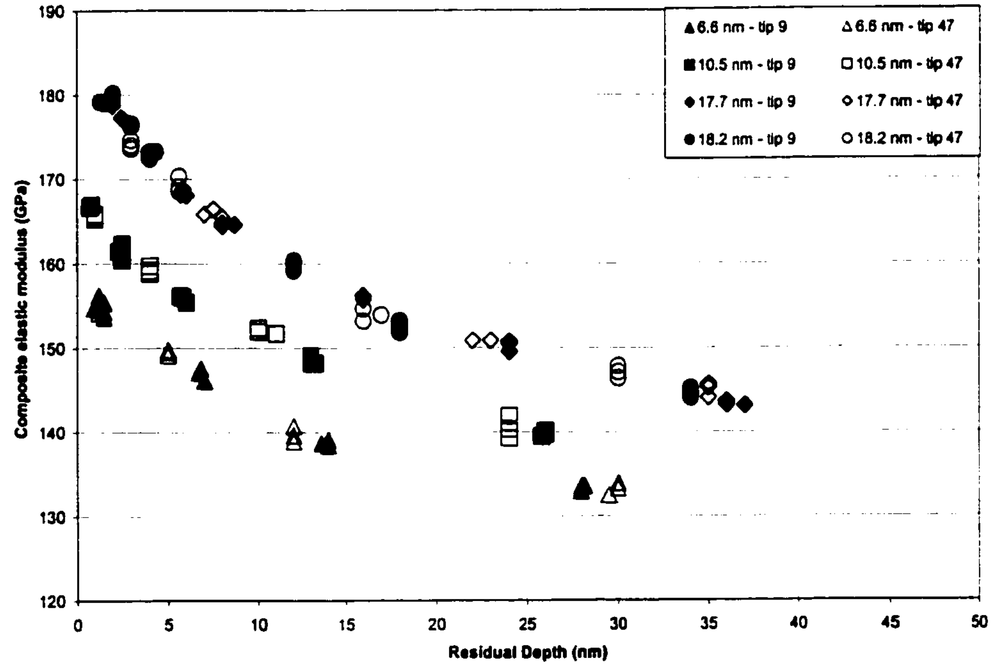

Fig. 7.10: Moduli of the thinner four films measured by tip 9 and corrected for the indenter deformation. No difference observed for data before and after correction.

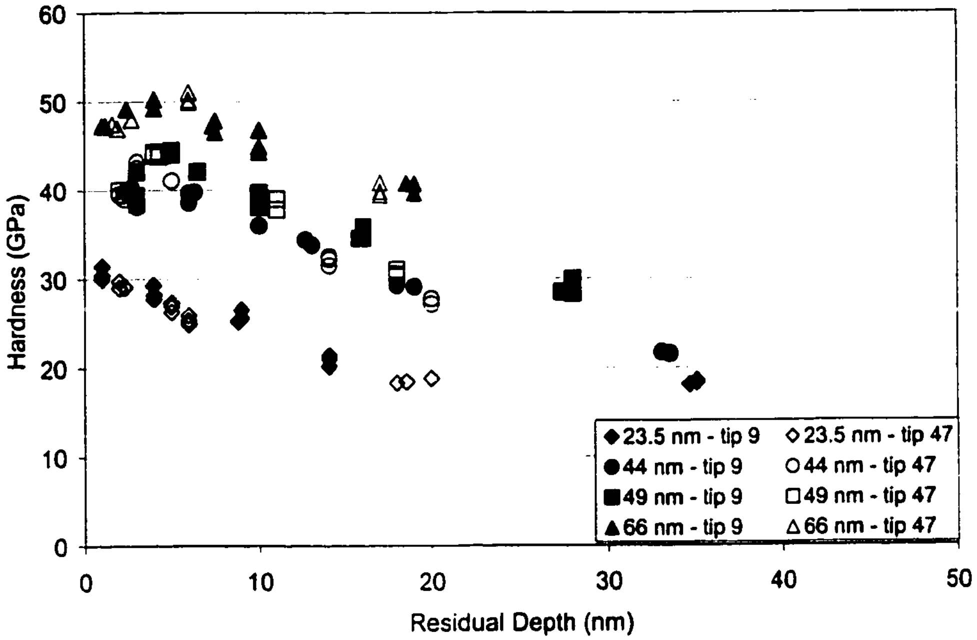

Fig. 7.11: Hardnesses of the thicker four films measured by tip 9 and corrected for indenter deformation. After correction, no significant difference can be observed between the measurements by tip 9 and tip 47.

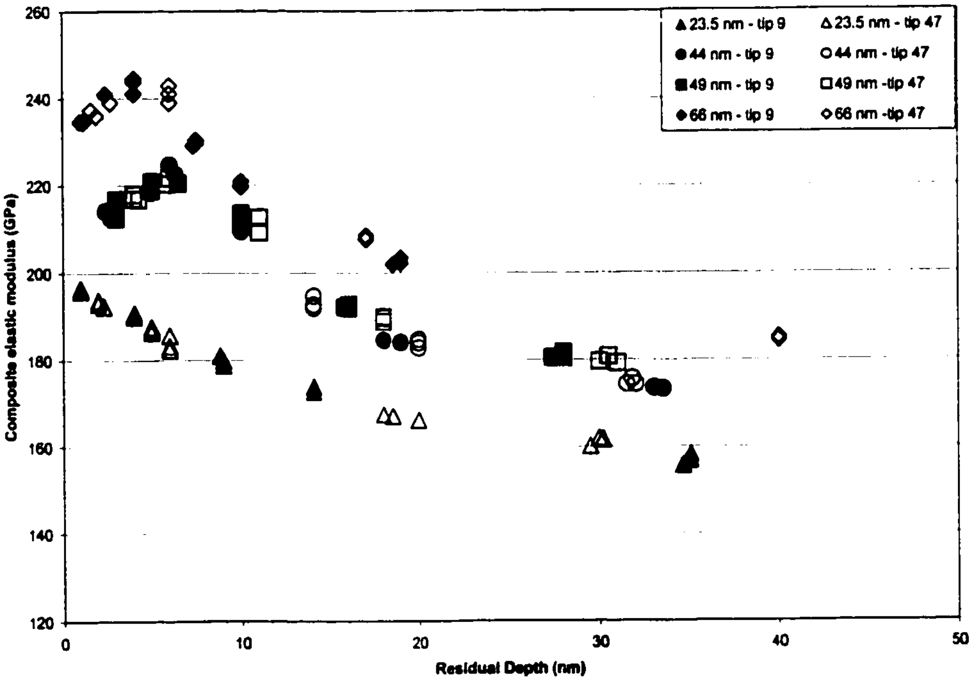

Fig. 7.12: Modulii of the thicker four films measured by tip 9 and corrected for indenter deformation. After correction, no significant difference can be observed between the measurements by tip 9 and tip 47.

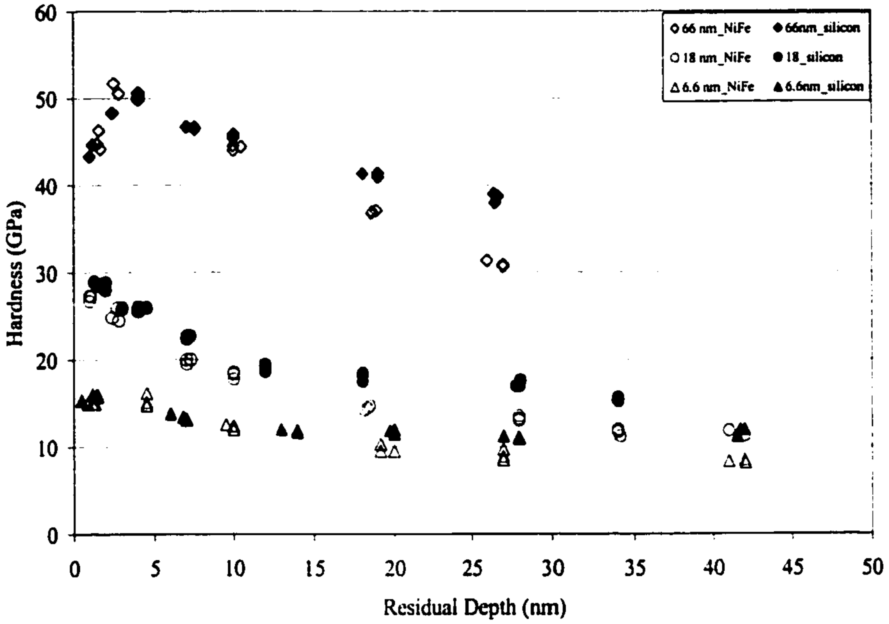

Fig. 7.13: Hardnesses of the films deposited on NiFe compared with those of the films on Silicon. The data shown have already been corrected for indenter deformation and was measured by tip 9.

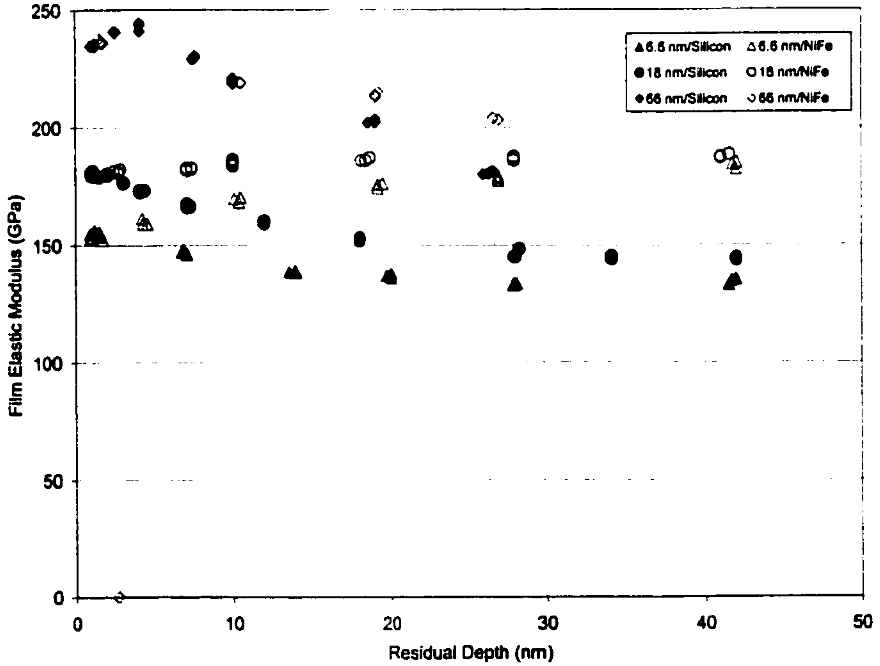

Fig. 7.14: Modulii of the films deposited on NiFe compared with those of the films on Silicon. The data shown have already been corrected for indenter deformation and was measured by tip 9.

Chapter 8

SUMMARY AND CONCLUSIONS

The strong demand for larger capacity data storage systems has pushed the hard disk drive industry to increase in areal density by 60% every year. Recently, with the advances in every aspect of computer hardware and software, the role of computers has escalated from data-processing machines to family entertainment centers. The type of files needed to be stored has changed from the traditional numbers and texts to multimedia files containing audio and video clips. For example, the recently introduced digital video recording machines using hard disk drives are likely to replace videocassette recorders in a few years. The shift of data types has further increased the demand for storage by orders of magnitude. To meet this challenge, the magnetic spacing between the read-write head and the disk in a hard disk drive must be significantly reduced below its current value of around 20 nm. In fact, this must be done by reducing the sizes of the two physical components of the magnetic spacing: the flying height and the protective overcoat thickness. As the flying height becomes lower and lower, accidental or even permanent contacts between the slider and disk seem inevitable. Thus, the protective overcoats have to be thin enough to reduce the magnetic spacing, and strong enough to protect the data from harder and more frequent impacts. It is truly a challenge to characterize the mechanical properties of these films. Nanoindentation techniques are used in this dissertation to study these thin film overcoats.

The equipment used in this dissertation includes the Point Contact Microscope and the Hysitron Picoindenter. Both are of SPM type, with resolution in nanometers. Their working mechanisms, advantages and disadvantages are described and discussed in the second chapter. The PCM measures the residual indentation areas using post-indentation scans near the indentation marks and obtains hardnesses that are defined as the maximum loads divided by the residual indentation areas. There are inherent errors associated with the post-indentation scans by the PCM. It requires substantial effort to reduce these errors and it is impossible to remove them completely. The Hysitron Picoindenter records the load/displacement curves during the indentation process. By analyzing the unloading curves using the theories provided in Chapters 3 and 4, the reduced elastic modulus of the specimen and the hardness defined as the maximum load divided by the maximum contact area can be obtained. The two definitions of hardness are compared, showing no significant difference for most materials. Therefore, the Hysitron Picoindenter is chosen as the instrument on which to perform all the measurements in this dissertation.

The theoretical analysis of the load/displacement curves generated by the Hysitron Picoindenter is based on Sneddon's solution for the elastic field in a homogenous half space indented by a flat punch. The specimen is assumed to be the half space with a flat surface. The solution is then expanded to include nanoindentation tests using indenters which are solids of revolution, or triangle- and square-based pyramidal indenters by modifying the boundary conditions, resulting in negligible errors. Sneddon's solution provides an equation with two unknowns, A and E_r in Eq. (3.5), therefore it is not a determinate system of equations. To close the system, a tip shape function is needed to establish an additional equation for the contact area *A*. To construct the tip shape function, a tip calibration procedure must be done on standard samples such as fused quartz. Therefore, the hardness and reduced elastic modulus of the specimen can be obtained by applying Sneddon's solution together with the tip shape function at the maximum penetration point on the unloading curve. In this method we make two assumptions that might not always be true: 1) constant tip shapes (according to the tip shape function setup), and 2) flat specimen surfaces. The former is examined and generalized in Chapter 4 and the latter is studied in Chapter 6. It is also worth noting that the hardness and reduced elastic modulus values are the composite ones if the indentations are done on thin film materials deposited on substrates. The indentation substrate effect is a major concern in the measurement of film properties for film/substrate systems, especially for films with thicknesses of 20 nm or less. Insight into the substrate effects for the elastic modulus measurements are provided by using Gao's solution for elastic fields in film and substrate systems. For a perfect cube-corner tip, it is suggested that the contact depth be kept below 11% of the film thickness to avoid any influence from substrates. This percentage is even smaller for a tip with a finite radius. The substrate effect for hardness measurements is not retrievable using Gao's solution, and is discussed with the indentation hysteresis techniques in Chapter 5.

As mentioned earlier, two assumptions made using the analysis based on Sneddon's solution may not always be valid. The first assumption is that the tip shape remains constant during any indentation tests. This assumption is implicit to the idea of the tip shape function. Since the tip shape function is found by a series of indentations with various forces on fused quartz, and is then used for indentations on all other materials, it is implicitly assumed unchanged for all materials. Because the indenter is made of diamond in the Hysitron Picoindenter, this assumption is valid for indentations on materials with hardnesses of 50 GPa or less,. However, if indentations are done on harder materials, the indenter geometry will change during the indentation processes. The indenter tends to deform in a way that increases the contact area, and thus, to lower the overall stress level in the indenter. Therefore, the method based on Sneddon's solution will overestimate the hardness and the reduced elastic modulus of the specimen. To solve this problem, a contact model based on the Hertz contact theory for contacts between elastic solids is proposed. Sneddon's solution can be re-derived with this model (Eq. (4.24)). An additional relation between the contact area, indentation depth, and tip radius can be obtained (Eq. (4.22)). The system of equations derived from this model is fully determinate. No extra assumption is necessary to close the system. Thus, the model is able to account for the indenter elastic deformation if indentations are made on materials as hard as the indenter. According to experimental data, it is sufficient to consider only the elastic deformation when a diamond indenter is used. The tip radius at the origin can also be calculated if the contact areas are known. No special equipment or time-consuming processes are needed. As expected, this model yields lower hardness and modulus values for very hard materials than those calculated by the method based on Sneddon's solution. However, when indenting on soft materials, it shows almost the same hardness and modulus values as the method based on Sneddon's solution. This is because indenter deformation is negligible while indenting on soft materials. The hardness and modulus values calculated by this method agree with the finite-element-simulated results by Follstaedt *et al.* Finally, this model is easy to integrate into commercial software, such as the Hysitron Triboscope 3.5 for analyzing load-unload/displacement curves. The correct hardness and reduced modulus values can be calculated in seconds, rather than hours or days, as is required using the finite-element simulation.

The indentation substrate effect has been mentioned earlier. However, only the effect for elastic modulus measurement has been quantified. An interesting concept based on indentation hysteresis has been proposed to study the substrate effect for hardness measurements. Indentation hystereses are generated by repeated indentations at the same location on the surfaces of several materials. Yielding in tension during the unloading process and re-yielding in compression during the subsequent loading process are observed in metals such as NiP and steel. Thus, an indentation hysteresis of the first type is generated. This hysteresis exhibits shakedown after a few cycles of repeated loading and unloading. This means that the yieldings on both the loading and unloading curves disappear after a few cycles. The loading/unloading processes after shakedown are purely elastic and thus reversible. Indentation hysteresis of the second kind is generated on semiconductors such as silicon and is due to phase transformation. Silicon undergoes a pressure-induced transformation from its semiconductor state to a denser metal state, which reverses when the load is withdrawn. The transformation is reversible and is not suppressible after multiple loading cycles. Therefore, the hysteresis exists for all cycles of repeated indentations and is not subject to shakedown. Indentation hysteresis is now one of the material properties. The substrate effect is then studied on a film with a hysteresis subject to shakedown deposited on a substrate with a hysteresis not subject to shakedown. The sample tested is a 100 nm permalloy film on a silicon substrate. Three indenters with different radii are used to study the influence of tip radius on substrate effects. The study shows that, for indentation residual depths smaller than 20% of the film thickness, substrate effects can be ignored. This statement is true for all the tips tested regardless of tip radius.

The second assumption made in the method using Sneddon's solution is that the surfaces of the specimen are mathematically flat. This is not true for indentations on surfaces with curvatures such as laser bumps or surfaces with a large roughness. Especially when our focus is on ultra thin films with thicknesses of 2 to 5 nm, very small indentation depths are needed to avoid the substrate effect. The indentation sizes are therefore comparable to that of the surface roughness. Measurement variation due to surface roughness is a major concern for this situation. A model has been proposed for the contact between the indenter and surfaces with curvature, such as bumps and asperities. The power of 2/3 of the R/R_0 is verified experimentally on surfaces asperities with radii of curvature ranging from 250 nm to 2 μm. The model is then adopted to study the roughness effect on the indentation hardness measurements. The concept of the apparent surface properties for a specific indentation has also been proposed. This concept gives slightly different surface properties for the same surface using indenters with different tip radii. The ratio of the standard deviation to the mean hardness was compared with the apparent standard deviation of $\left(\frac{R_i}{R_0}\right)^{\frac{2}{3}}$, where R_i is the relative radius of curvature for *i*th surface profilometric measurement and R_0 is the indenter tip radius. The results show that the roughness effect deceases as the indentation size increases, and at very small indentations the ratios of the standard deviations to the mean hardnesses equal the standard deviation of $\left(\frac{R_i}{R_0}\right)^{\frac{2}{3}}$ for all of the sample and indenter combinations. This means that, with the model proposed in Chapter 6, the roughness effect on the indentation hardness measurements can be predicted using only the knowledge of the surface properties and tip radii.

It has been reported that the recently developed cathodic-arc amorphous carbon films (also called CAC films) have superior mechanical properties due to their high concentration of sp^3 bondings and may be the solution for the 2 nm protective overcoats. Therefore, the last topic of this dissertation is to study the mechanical properties of the CAC films using the models and methods proposed in the previous chapters. CAC films with various thicknesses are deposited on silicon and permalloy. Two diamond indenters of different tip radii of 50 nm and 160 nm are used to study the tip radius effect on these films. After compensation for elastic deformation of the sharper tip, the measurements made by both tips are consistent. However, both hardnesses and elastic modulii of the CAC films are thickness dependent. In other words, thick films have higher hardnesses and elastic modulii. Substrate effects on the measurements are suspected. However, we find that the measurements at shallow indentations are nearly the same for films with the same thicknesses deposited on different substrates. The substrate effects could only be observed for large indentations. This suggests that the measured hardnesses and elastic modulii at shallow indentations are the true properties of the films. There are no inherent errors due to the nanoindentation testing techniques. The thickness dependence phenomenon is one of the material properties of these films. An explanation for this phenomenon could be drawn from the existence of top layers associated with the CAC films. The films are predominately sp^3 bonded up to certain thicknesses. Beyond that there is an sp^2 bonded softer top layer on the sp^3-bonded bulk. If the films are thinner than the top layer thickness, the films are soft and no drops in mechanical properties could be seen at shallow indentations. If the films are thicker than the *sp*^{2} top layer thickness, the films are harder and drops in hardness and elastic modulus at shallow indentations could be observed. These drops are indicators for the existence of the softer top layers. The thicknesses of the top layers were estimated at 16 to 20 nm using the rule of thumb obtained in Chapter 5. There are no published thicknesses available for these films other than the rough estimation of about 20 nm by Pharr *et al.* It is concluded that, although the CAC films have extremely high hardnesses and elastic modulii in the bulk region, they always have top layers that are much softer than the bulk. Such soft layers can be observed with the nanoindentation techniques for films thicker than 23.5 nm. Therefore, the mechanical properties of the CAC films are inherently thickness-dependent.

On the whole, this dissertation focuses on developing and extending the capability of nanoindentation techniques of finding the hardnesses and elastic modulii of thin film overcoats with the Hysitron Picoindenter. The models proposed in this dissertation have been proven to be useful for studies toward this goal.

REFERENCE

Ager III, J. W., Anders, S., Anders, A., and Brown, I. G., 1995, "Effect of intrinsic growth stress on the Raman spectra of vacuum-src-deposited amorphous carbon films", *Applies Physics Letters*, Vol. 66, No. 25, pp. 3344-3346.

Anders, S., Anders, A., Brown, I. G., Wei, B., Komvopoulos, K., Ager III, J. W., Yu, K. M., 1994, "Effect of vacuum arc deposition parameters on the properties of amorphous carbon thin films", *Surface & Coatings Technology*, Vol. 68/69, pp. 388-393

Bhattacharya, A. K. and Nix, W. D., 1988, "Analysis of elastic and plastic deformation associated with indentation testing of thin films on substrates", *International Journal of Solids and Structures*, Vol. 24, No. 12, pp. 1287-98

Binnig, G., Quate, C. F., and Gerber, Ch., 1986, "Atomic Force Microscope", *Physical Review Letters*, Vol. 56, No. 9, pp. 930-933.

Bobji, M. S., Fahim, M., Biswas, S. K., 1996, "Hardness estimated from the indentation of a spherical body. Some implications for nanoindentation test restuls", *Tribology Letters*, Vol. 2, pp. 381-391

Bobji, M. S. and Biswas, S. K., 1998, "Estimation of hardness by nanoindentation of rough surfaces", *Journal of Materials Research*, Vol. 13, No. 11, pp. 3227-3233.

Bobji, M. S. and Biswas, S. K., 1999, "Deconvolution of hardness from data obtained from nanoindentation of rough surfaces", *Journal of Materials Research*, Vol. 14, No. 6, pp. 2259-2268.

Bobji, M. S., Fahim, M., and Biswas, S. K., 1996, "Hardness estimated from the indentation of a spherical body. Some implications for nanoindentation test results", *Tribology Letters*, Vol. 2, pp. 381-391.

Clarke, D. R., Kroll, M. C., Kirchner, P. D., Cook, R. F., and Hockey, B. J., 1988, "Amorphization and conductivity of silicon and germanium induced by indentation", *Physical Review Letters*, Vol. 60, No. 21, pp. 2156-2159

Davis, C. A., Knowles, K. M., and Amaratunga, G. A., 1995, "Cross-sectional structure of tetrahedral amorphous carbon thin films", *Surface and Coatings Technology*, Vol. 76-77, pp. 316-321.

Doerner, M. F., and Nix, W. D., 1986, "A method for interpretating data from depth-sensing indentation instruments", *Journal of Materials Research*, Vol. 1, pp. 601-609

Follstaedt, D. M., Knapp, J. A., Myers, S. M., Dugger, M., Friedmann, T. A., Sullivan, J. P., Monteiro, O. R., Ager III, J. W., Brown, I. G., and Christenson, T., 1997, "Energetic particle synthesis of metastable layers for superior mechanical properties", 1997 Fall meeting of Material Research Society.

Friedmann, T. A., Sullivan, J. P., Knapp, J. A., Tallant, D. R., Follstaedt, D. M., Medlin, D. L., and Mirkarimi, P. B., 1997, "Thick stress-free amorphous-tetrahedral caron films with hardness near that of diamond", *Applied Physics Letters*, Vol.71, No.26, pp. 3820-3826.

Gao, H., Chiu, C. H., and Lee, J., 1992, "Elastic contact versus indentation modeling of multi-layered materials", *International Journal of Solids and Structures* Vol. 29, No. 20, pp. 2471-2492

Gerk, A. P. and Tabor D., 1978, "Indentation hardness and semiconductor-metal transition of germanium and silicon", *Nature*, Vol. 271, pp. 772-773

Gilkes, K. W., Gaskell, P. H., and Yuan, J., 1993, "Atomic Structure of tetrahedral amorphous carbon", *Journal of Non-Crystalline Solids*, Vol. 166, pp. 164-166.

Greenwood, J. A. and Williamson, J. B. P., 1966, "Contact of nominally flat surfaces", *Proceedings Royal Society*, Vol. A295, pp. 300

Greenwood, J. A. and Tripp, J. H., 1967, "The elastic contact of rough surfaces", *Transactions of ASME, Series E, Journal of Applied Mechanics*, Vol. 34, pp. 153

Hsiao, R. and Bogy, D. B., 1996, "Nano-indentation and nano-scratch tests", Technical Report 96-020, Computer Mechanics Laboratory, Department of Mechanical Engineering, University of California, Berkeley.

Hu, J. Z., Merkle, L. D., Menoni, C. S., and Spain, I. L., 1986, "Crystal data for high-pressure phases of silicon", *Physical Review B*, Vol. 34, No. 7, pp. 4679-4684

Hysitron Triboscope Users Manual

Jiang, Z., Lu, C.-J., Bogy, D. B., Bhatia, C. S., and Miyamoto, T., 1995, "Nanotribological characterization of hydrogenated carbon films by scanning probe microscopy", *Thin Solid Films*, Vol. 258, pp. 75-81

Johnson, K. L., 1985, Contact Mechanics, Cambridge University Press, Cambridge, United Kingdom

Kaneko, R., Nonaka, K., and Yasuda, K., 1988, "Scanning tunneling microscope and atomic force microscopy for microtribology", *Journal of Vacuum Science Technology* Vol. 6, No. 2, pp. 291-292

King, R. B., 1987, "Elastic analysis of some punch problems for a layered medium", *International Journal of Solids and Structures*, Vol. 23, No. 12, pp. 1657-1664

Knapp, J. A., Follstaedt, D. M., Barbour, J. C., Myers, S. M., 1997 "Finite element modeling of nanoindentation for determining the mechanical properties of implanted layers and thin films", *Nuclear Instruments and Methods in Physics Research*, Sec. B, Vol. 127, pp. 935-939

Kral, E. R., Komvopoulos, K., and Bogy, D. B., 1993, "Elastic-plastic finite element analysis of repeated indentation of a half-space by a rigid sphere", *J. Applied Mechanics*, Vol. 60, pp 829-841

Laursen, T. A. and Simo, J. C., 1992, "A study of the mechanics of microindentation using finite elements", ", *Journal of Materials Research*, Vol. 7, pp. 618-26

Ling, F. F., 1973, "Surface Mechanics", John Wiley & Sons, Inc., New York, pp.173-179

Lo, R. Y., Bogy, D. B., 1997, "On the measurement of nanohardness and elastic modulus of ultra-thin overcoats: effect of W-doping and annealing on the properties of DLC", Technical Report No. 97-017, Computer Mechanics Laboratory, Department of Mechanical Engineering, University of California, Berkeley

Lo, R. Y. and Bogy, D. B., 1999, "Compensating for elastic deformation of the indenter in hardness tests of very hard materials", *J. of Materials Research*, Vol. 14, No. 6, pp. 2276-2282

Lu, C.-J., Bogy, D. B., and Kaneko, R., 1994, "Nanoindentation hardness tests using a point contact microscope", *Journal of Tribology*, Vol. 116, pp. 175-180

Lu, C.-J. and Bogy, D. B., 1995, "The effect of tip radius on nano-indentation hardness tests", *International Journal of Solids and Structures*, Vol. 32, No. 12, pp. 1759-1770

Lu, C.-J. and Bogy, D. B., 1995, "Sub-microindentation hardness tests on thin film magnetic disks", *Advances in Information Storage Systems* Vol. 6, pp. 163-175

McKenzie, D. R., Muller, D., and Pailthorpe, B. A., 1991, "Compressive-stress-induced formation of thin-film tetrahedral amorphous carbon", *Physical Review Letters*, Vol. 67, No. 6, pp. 773-776

Monteiro, O. R.; Delplancke-Ogletree, M. P.; Lo, R. Y.; Winand, R.; Brown, I., 1997, "Synthesis and characterization of thin films of WC_x, produced by mixing W and C plasma streams", *Surface and Coatings Technology*, Vol. 94-5, No. 1-3, pp. 220-225

Pharr, G. M., Oliver, W. C., and Clarke, D. R., 1989, "Hysteresis and discontinuity in the indentation load-displacement behavior of Silicon", *Scripts Metallurgica*, Vol. 23, pp. 1949-1952

Pharr, G. M., Oliver, W. C., and Brotzen, F. R., 1992, "On the generality of the relationship among contact stiffness, contact area, and elastic modulus during indentation", *Journal of Material Research*, Vol. 7, No. 3, pp. 613-617

Pharr, G. M., Callahan, D. L., Mcadams, S. D., Tsui, T. Y., Anders S., Anders, A., Ager III, J. W., Brown, I. G., Bhatia, C. S., Silva, S. R. P., Robertson, J., 1996, "Hardness, Elastic Modulus, And Structure Of Very Hard carbon Films Produced By Cathodic-Arc Deposition With Substrate Pulse Biasing", *Applied Physics Letters*, Vol. 68, No. 6, pp. 779-781

Ramsey, P. M., 1991, "Modeling the contact response of coated systems", *Surface and Coatings technology*, Vol. 49, pp. 504-509

Sneddon, I. N., 1965, "The relation between load and penetration in the axisymmetric Boussinesq problem for a punch of arbitrary profile", *International Journal of Engineering Science*, No. 3, pp. 47-57

Stilwell, N. A. and Tabor, D., 1961, "Elastic recovery of conical indentations", *Proceedings Physics Society London*, Vol. 78, pp. 169-179

Tabor, D., 1948, "A simple theory if static and dynamic hardness", *Procedings Royal Society*, Vol. A 192, pp.247-274

Tabor, D., 1951, The Hardness of Metals, Clarendon Press, Oxford

Tai, Y. C. and Muller, R. S., 1989, "IC-processed electrostatic synchronous micromotors", *Sensors and Actuators*, Vol. 20, pp. 49-55

Veerasamy, V. S., Amaratunga, G. A. J., Milne, W. I., Robertson, J., and Fallon, P. J., 1993, "Influence of Carbon Ion Energy on Properties of Highly Tetrahedral Diamond-Like Carbon," *Journal of Non-Crystalline Solids*, Vol. 164-166, pp. 1111-1114

Wu, Y. Q., Shi, G. Y., and Xu, Y. B., 1999, "Cross-section observation on the indentation of [001] silicon", *J. of Materials Research*, Vol. 14, No. 6, pp. 2399-2401

Yang, X., Grosjean, C., Tai, Y. C., and Ho, C. M., 1997, "A MEMS Thermopneumatic Silicone Membrane Valve," *Proceedings, 1997 IEEE Micro Electro Mechanical Systems Workshop (MEMS '97)*, Nagoya, Japan, pp. 114-118

Young, D. A., 1991, Phase Diagrams of the elements, University of California Press, Berkeley and Los Angeles, California, pp. 105

Yun, X., Hsiao, R., Bogy, D. B., Bhatia, C. S., 1996, "Hardness and tribochemical evaluation of ultra-thin CHx and CNx overcoats", Technical Report 96-015, Computer Mechanics Laboratory, Department of Mechanical Engineering, University of California, Berkeley